

Determination of the Kinematics of the Q_{weak} Experiment and Investigation of
an Atomic Hydrogen Møller Polarimeter

Valerie Marie Gray
Baileys Harbor, Wisconsin

Master of Science, College of William & Mary, 2013
Bachelor of Science, St. Norbert College, 2011

A Dissertation presented to the Graduate Faculty
of The College of William & Mary in Candidacy for the
Degree of Doctor of Philosophy

Department of Physics

College of William & Mary
January 2018

© 2018
Valerie Marie Gray
All Rights Reserved
Attribution-NonCommercial
(CC BY-NC)

APPROVAL PAGE

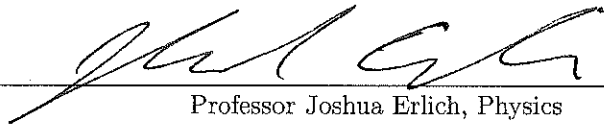
This Dissertation is submitted in partial fulfillment of
the requirements for the degree of

Doctor of Philosophy

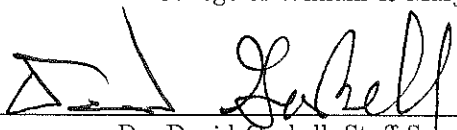

Valerie Marie Gray

Approved by the Committee, November 2017


Committee Chair
Chancellor Professor of Physics David Armstrong, Physics
College of William & Mary


Professor Joshua Erlich, Physics
College of William & Mary


Professor Todd Averett, Physics
College of William & Mary


Dr. David Gaskell, Staff Scientist
Thomas Jefferson National Accelerator Facility

ABSTRACT

The Q_{weak} experiment has tested the Standard Model through making a precise measurement of the weak charge of the proton (Q_{W}^{p}). This was done through measuring the parity-violating asymmetry for polarized electrons scattering off of unpolarized protons. The parity-violating asymmetry measured is directly proportional to the four-momentum transfer (Q^2) from the electron to the proton. The extraction of Q_{W}^{p} from the measured asymmetry requires a precise Q^2 determination. The Q_{weak} experiment had a $Q^2 = 24.8 \pm 0.1 \text{ m}(\text{GeV}^2)$ which achieved the goal of an uncertainty of $\leq 0.5\%$. From the measured asymmetry and Q^2 , Q_{W}^{p} was determined to be 0.0719 ± 0.0045 , which is in good agreement with the Standard Model prediction. This puts a 7.5 TeV lower limit on possible “new physics”. This dissertation describes the analysis of Q^2 for the Q_{weak} experiment.

Future parity-violating electron scattering experiments similar to the Q_{weak} experiment will measure asymmetries to high precision in order to test the Standard Model. These measurements will require the beam polarization to be measured to sub-0.5% precision. Presently the electron beam polarization is measured through Møller scattering off of a ferromagnetic foil or through using Compton scattering, both of which can have issues reaching this precision. A novel Atomic Hydrogen Møller Polarimeter has been proposed as a non-invasive way to measure the polarization of an electron beam via Møller scattering off of polarized monatomic hydrogen gas. This dissertation describes the development and initial analysis of a Monte Carlo simulation of an Atomic Hydrogen Møller Polarimeter.

TABLE OF CONTENTS

Acknowledgements	iv
Dedication	vi
List of Tables	vii
List of Figures	viii
List of Equations	x
1 Introduction	1
2 Theory of Weak Charges	3
2.1 Theory of the Standard Model	3
2.2 Parity Violation	5
2.3 Electroweak Theory	6
2.3.1 Spontaneous Symmetry Breaking	7
2.3.2 Neutral Current	10
2.3.3 Nucleon Weak Charge	12
2.4 Why Study Physics Beyond the Standard Model	14
2.5 Theory of Q_{weak}	15
3 Q_{weak} Experiment Apparatus	17
3.1 Jefferson Lab Overview	17
3.2 Q_{weak} Experiment Requirements	18
3.2.1 Integration Mode vs. Tracking Mode	19
3.3 Q_{weak} Experiment Apparatus	20
3.3.1 Target	21
3.3.2 The QTor Magnetic Spectrometer	22
3.3.3 Collimators	22
3.3.4 Main Detectors	23
3.3.5 Tracking Chambers	24
3.3.5.1 Horizontal Drift Chambers	25
3.3.5.2 Vertical Drift Chambers	26
3.3.5.3 Trigger Scintillators	26
3.3.6 Beam Position Monitors	26
3.3.7 Beam Current Monitors	27
3.3.8 Luminosity Monitors	27
4 Tracking Mode: Data and Simulation Analysis	28
4.1 Q_{weak} Experiment Simulation	29
4.2 Measured Q^2 vs. Interaction Q^2	30
4.3 Kinematics Validations Using Tracking Data	31
4.3.1 Target Properties	32
4.3.1.1 Target Location	32
4.3.1.2 Target Boiling	33
4.3.2 Beam Properties	34
4.3.2.1 Raster Size	35
4.3.2.2 Beam Position	36
4.3.2.3 Beam Angle	42
4.3.2.4 Beam Energy	44

4.3.3	QTor Magnet Properties	46
4.3.3.1	Magnetic Field Strength Scan	47
4.3.3.2	Magnetic Field Sector Rotation Study	49
4.3.4	Main Detector and Primary Collimator	51
4.3.4.1	Position of Main Detectors	51
4.3.4.2	Primary Collimator Location	53
4.3.4.3	Primary Collimator Imperfections	54
4.3.5	Radiative Corrections	56
4.3.6	Q^2 Uncertainty Synopsis	56
4.4	Q^2 Determination	58
4.4.1	Simulation to Data Correction for Run 2	59
4.4.2	Extraction of Q^2 for Run 1	60
4.5	Final Q^2	60
4.6	Asymmetry Correction from Tracking	61
4.6.1	Lightweighting Correction	61
4.6.2	Acceptance Correction	62
5	Final Result from the Q_{weak} Experiment	64
5.1	Uncertainties on A_{ep}	64
5.2	Final Q^{P}_{W}	67
5.3	Possible Improvements to Q^2	68
6	Electron Beam Polarimetry	71
6.1	Theory of Møller Scattering	71
6.2	Theory of Compton Scattering	73
6.3	Existing Polarimeter Technology	75
6.3.1	Møller Polarimeters	76
6.3.2	Compton Polarimeters	78
6.4	Advantages of a Hydro-Møller	79
6.5	Future Needs for Precision Polarimetry	79
6.5.1	The P2 Experiment	79
6.5.2	The MOLLER Experiment	81
7	Concept and Design of the Hydro-Møller	82
7.1	Hydro-Møller Concept	82
7.2	Electron Polarization States of Atomic Hydrogen	83
7.3	Requirements on the Hydrogen Gas Target	85
7.3.1	Dissociation of Diatomic Hydrogen	86
8	The Hydro-Møller Simulation: HMolPol	88
8.1	HMolPol Simulation	88
8.1.1	Primary Generator	88
8.1.2	Atomic Hydrogen Target	89
8.1.3	Detectors	90
8.1.4	Input/Output	91
8.1.5	Hall A Magnetic Optics	92
8.2	HMolPol Analysis	93
8.2.1	Beam Energy Scan	94
8.2.1.1	θ_{CM} Distribution	100
8.2.2	Hall A Magnetic Optics	100

8.2.2.1	θ_{CM} Distribution	101
8.2.2.2	Radius vs. θ_{CM}	104
8.2.2.3	ϕ Angle Rotation	106
8.3	Next Stages in HMolPol Development	107
9	Conclusion	110
A	Q^2 Derivation	111
A.1	Q^2 Derivation	111
A.2	Q^2 Derivation: Relativistic Limit	113
A.3	Q^2 Elastic Scattering in the Relativistic Limit	114
B	Eigenstates and Energies of Atomic Hydrogen	117
C	Analyzing Power for Møller Scattering	120
C.1	Lab Frame Analyzing Power Derivation	120
C.2	Energy Independence of the Analyzing Power	123
D	Hydro-Møller: Expected Event Rates	126
D.1	Expected Event Rates	126
D.2	Experimental Time Required per Measurement	128
	References	132

ACKNOWLEDGEMENTS

“Sometimes I lie awake at night and I ask, ‘Is life a multiple choice test or is it a true or false test?’... Then a voice comes to me out of the dark and says, ‘We hate to tell you this but life is a thousand word essay.’ ” — *Charlie Brown*
Clearly good ol’ Charlie Brown didn’t know about graduate school because my dissertation is way more than a thousand words; but like him, there have been many people who have supported me.

I would like to thank my adviser, David Armstrong, for all the help and guidance during my time at William & Mary. I am extremely grateful for all the time he has given to answering my questions and helping me through everything here. Thanks also to the members of my committee Dave Gaskell, Joshua Erlich, and Todd Avertt for help on various components of my work.

I would also want to acknowledge my undergraduate teacher, adviser, and mentor, Michael Olson, without whom I would have never realized physics was interesting and pursued experimental nuclear physics. His advice and guidance at St. Norbert College and after has been invaluable and instrumental. I was given many opportunities for teaching, mentoring, and doing research and indispensable lab skills that I otherwise wouldn’t have gotten. Also thanks for all the time dedicated to helping, working on research, and developing new labs for classes. I can’t thank him enough for his amazing capacity for fostering confidence, giving perspective when needed, and the advice and support he has shared with me over the years and the ones to come.

To the people whom I owe my existence, my parents David and Jola Gray. Thanks for all the unwavering support over the years, both from stands and off. I also would like to acknowledge my brother, Christopher Gray, and my life long friends Amanda Zahn, and Kirsten Jaquet. Thank you for the support, messages, jokes, and being able to drop a line whenever either of us needs it. Regardless of where we have been or are going in our lives we always are able to talk and you smile and listen when the topic turns to science.

I would also like to thank Kansas State University’s High Energy Physics group, specifically Tim Bolton and Glenn Horton-Smith, University of Notre Dame’s Nuclear Astrophysics department, and Joint Institute for Nuclear Astrophysics (JINA) specifically Micheal Wiescher, Ed Stech, and their group for a great REU program experience.

I would also like to say thanks to the people I worked with while being on the executive board of the Forum of Graduate Student Affairs the American Physical Society, the fellow students: Laura Boon, Brock Russell, Krista Freeman, Josh Einstein-Curtis, Richard Ruiz, and others. I am very grateful for the help and advice of Amy Flatten, Michele Irwin, Crystal Bailey, Steven Lambert, and others.

I’d also like to thank the Q_{weak} tracking group, Mark Pitt, Anna Lee, and Jie Pan. I am grateful for the help from the Q_{weak} collaboration, especially my

fellow graduate students and the William & Mary parity group. I would like to thank all the undergrads who I worked with here at William & Mary: Hannah Smith, Connor Simpson, Wyndham Batchelor, Richie Thaxton, Matt Ferry Chris Haufe, Melissa Guidry, Quinn Hailes, David Specht, Jeff Buffkin, and Jonathan Rigby. I couldn't have done this without my friends and fellow graduate students at William & Mary. This is not exhaustive or in any order, Victoria Owen, Juan Carlos Cornejo, Kurtis Bartlett, Anashe Bandari, Tangereen Claringbold, Martin Rodriguez-Vega, Ellie Radue, Raymundo Ramos, James Dowd, Brittany Dowd, Anne Norrick, Perry Nerem, and Denise McKaig. Financial support from the National Science Foundation, under grants PHY-1405857 and PHY-1206053 , and from the Virginia Space Grant Consortium, is gratefully acknowledged.

This dissertation is dedicated to my parental unit.

LIST OF TABLES

2.1	Fermion Properties and Coupling Constants	12
4.1	Beam Position Scan	41
4.2	Beam Angle Scan	42
4.3	Uncertainties on the Q^2 measurement	57
4.4	Differences Between Run 1 and Run 2 in the Q_{weak} Experiment .	59
5.1	Final Quadrature Systematic Uncertainties in the Q_{weak} Experiment	65
5.2	Final Asymmetries in the Q_{weak} Experiment	67
6.1	Comparisons of Different Polarimeters	80
7.1	Eigenstates and Energies of Hydrogen	84
8.1	Properties of the Target	90
8.2	Location of Hall A Magnets	92
8.3	Unpolarized Cross Section, Analyzing Power, and Rate for Various Beam Energies	95
8.4	Status of Magnetic Fields for Optic Simulations	101

LIST OF FIGURES

2.1	Standard Model Diagram	4
2.2	Higgs Potential	6
2.3	Neutral Current Exchange Diagrams	10
3.1	Layout of Continuous Electron Beam Accelerator Facility	18
3.2	Integration Mode vs. Tracking Mode	20
3.3	Layout of the Q_{weak} Experiment	21
3.4	Picture of the Q_{weak} Experiment Apparatus	22
3.5	Projection of Scattered Electron Tracks on the Main Detectors	23
3.6	Main Detector Numbers for the Q_{weak} Experiment	24
3.7	Cherenkov Radiation	24
3.8	Path of the Electrons Through the Tracking System	25
4.1	Q^2 vs. Target Location	32
4.2	Simulated Q^2 vs. Target Length	34
4.3	The Q_{weak} Experiment and JLab Accelerator Coordinate Systems	35
4.4	Q^2 vs. Raster Size	36
4.5	\hat{x} Beam Position Scan in Main Detectors 1 and 5	37
4.6	\hat{x} Beam Position Scan in Main Detectors 3 and 7	38
4.7	\hat{y} Beam Position Scan in Main Detectors 3 and 7	39
4.8	\hat{y} Beam Position Scan in Main Detectors 1 and 5	40
4.9	\hat{x} Beam Angle Scan for Main Detectors 1 and 5	43
4.10	\hat{x} Beam Angle Scan for Main Detectors 3 and 7	44
4.11	\hat{y} Beam Angle Scan for Main Detector 1 and 5	44
4.12	\hat{y} Beam Angle Scan for Main Detectors 3 and 7	45
4.13	Q_{weak} Beam Energy	46
4.14	Q^2 vs. QTor Current from the GEANT4 Simulation	47
4.15	Q^2 vs. QTor Current from the Data	48
4.16	Q^2 vs. QTor Current from Data and GEANT4 Simulation	48
4.17	Rotations of QTor's Magnetic Field	49
4.18	Q^2 Variations due to QTor Magnetic Field Rotations	50
4.19	Q^2 for Ideal and Actual Main Detector Locations	52
4.20	Primary Collimator Shifts	53
4.21	Effects of the Primary Collimator Shifts	54
4.22	Projection to the Primary Collimator	55
4.23	Radiative Correction Cartoon	56
4.24	Q^2 Distribution from GEANT4 Simulation	58
4.25	PMT Light Yield vs. Position on Main Detector Bar	62
4.26	Light Yield Across the Main Detectors	63
5.1	Reduced Asymmetry vs. Q^2	68
6.1	Lowest-order Feynman Diagrams for Møller Scattering	72
6.2	Møller Scattering Analyzing Power vs. θ_{CM}	73
6.3	Lowest-order Feynman Diagrams for Compton Scattering	73
6.4	JLab's Hall A Møller Polarimeter Layout	77
6.5	Schematic of JLab's Hall C Compton Polarimeter	78

7.1	Schematic of the Hydro-Møller	83
7.2	Splitting of Energy Levels of Hydrogen	84
7.3	Schematic of the Apparatus Used by S. B. Crampton <i>et al.</i>	86
7.4	Schematic of the Apparatus for an Polarized Hydrogen Beam . . .	87
8.1	Relative Magnetic Field Strength and Gas Density of the Hydro-Møller Target	90
8.2	Target in HMolPol	91
8.3	Hall A Magnetic Optics in HMolPol	93
8.4	Cross Section and Analyzing Power vs. θ_{CM} for Møller Scattering	94
8.5	θ_{CM} Distribution on DummyDet for Beam Energies Similar to MAMI	96
8.6	Radius of the Hits vs. θ_{CM} on DummyDet for Beam Energies Similar to MAMI	97
8.7	θ_{CM} Distribution on DummyDet for Beam Energies Similar to JLab	98
8.8	Radius of the Hits vs. θ_{CM} on DummyDet for Beam Energies Similar to JLab	99
8.9	Hall A Møller Polarimeter's Quadropoles Settings	101
8.10	θ_{CM} Distribution on DummyDet for Different Magnetic Field Configurations	102
8.11	Radius vs. θ_{CM} Distribution on DummyDet for Different Magnetic Field Configurations	105
8.12	Difference in the ϕ_{Lab} for each Primary Electrons vs. θ_{CM} Distribution	108
A.1	Electron Scattering off a Proton	111
C.1	Scattering Electrons in the Lab Frame	122
C.2	Analyzing Power vs. θ_{Lab}	124

LIST OF EQUATIONS

2.1	Dirac Lagrangian	4
2.2	Covariant Derivative	4
2.3	A_μ Gauge Transformation	4
2.4	Helicity	5
2.5	Weak Charge Singlet and Doublet States for the Electron	5
2.6	Standard Model Lagrangian	6
2.7	Higgs part of the SM Lagrangian	6
2.8	Higgs Potential	6
2.9	Electroweak Covariant Derivative	6
2.10	Higgs Complex Scalar Doublet	7
2.11	Higgs Minimum Potential	7
2.12	Covariant Derivative for the Vacuum State	8
2.12	W_μ^\pm Gauge Term	8
2.13	Z_μ Gauge Term	8
2.14	A_μ Gauge Term	8
2.16	Simplified Covariant Derivative for the Vacuum State	8
2.17	Mass of W^\pm, Z^0, γ	8
2.18	Definition of the Weinberg Angle	9
2.19	Weinberg Angle in Terms of Masses of the W and Z	9
2.19	Definition of Z_μ Gauge Term Using Weinberg Angle	9
2.20	Definition of A_μ Gauge Term Using Weinberg Angle	9
2.22	Perturbation of the Higgs Minimum Potential	9
2.23	Z^0 's Neutral Current	10
2.24	Photon's Neutral Current	10
2.25	Isospin Neutral Current	10
2.26	Gell-Mann Nishijima Relation	11
2.27	Hypercharge Neutral Current	11
2.28	Z^0 's Neutral Current in Terms of Q and the Weak Isospin	11
2.28	Fermion's Weak Vector Charge	11
2.29	Fermion's Weak Axial Charge	11
2.32	Z^0 's Neutral Current in Terms of g_V^f and g_A^f	12
2.33	Proton's Electromagnetic Charge	12
2.34	Proton's Weak Charge	13
2.35	Effective Z^0 Neutral Current Lagrangian	13
2.36	Neutral Current Lagrangian	13
2.36	u Quark Weak Vector and Axial Couplings	14
2.37	d Quark Weak Vector and Axial Couplings	14
2.39	Proton's Weak Charge in Terms of the Quark Weak Vector and Axial Couplings	14
2.40	Measured Asymmetry	15
2.41	Parity-violating Asymmetry	15
4.1	Q^2 of Elastically Scattered Electron Independent of E'	30
4.2	Visible Q^2 for the Q_{weak} Experiment	31

4.3	Visible Q^2 from the GEANT4 Simulation	31
4.4	Geometric Contribution to Q^2 due to the Primary Collimator.	53
4.7	Lightweighting Correction Factor	61
4.8	Acceptance Correction Factor	63
6.1	Theoretical Asymmetry	71
6.2	Møller Scattering Cross Section for Longitudinally Polarized Electrons	72
6.3	Møller Scattering Unpolarized Cross Section	72
6.4	Møller Scattering Asymmetry for Longitudinally Polarized Electrons	72
6.5	Compton Scattering Differential Cross Section, when Integrating over the Azimuthal Angle	74
6.6	Unpolarized Cross Section for Compton Scattering	74
6.7	Longitudinally Spin-dependent Cross Section for Compton Scattering	74
6.9	Maximum Scattering Energy of the Photon in Compton Scattering .	74
6.10	Analyzing power for Compton Scattering	75
6.11	Analyzing Power at the Compton Edge	75
6.12	Relationship Between Analyzing Power and Measured Asymmetry for Møller Scattering	76
6.13	Beam Polarization in terms of the Target Polarization, Analyzing Power and Measured Asymmetry for Møller Scattering	76
6.14	Relationship Between Analyzing Power and Measured Asymmetry for Compton Scattering	76
6.15	Beam Polarization in terms of the Target Polarization, Analyzing Power and Measured Asymmetry for Compton Scattering	76
7.1	Hamiltonian for the Hydrogen Atom	83
7.2	Mixing Angle for the Hydrogen Atom	84
8.1	Unpolarized Rate Normalized to the Beam Current	95
8.2	Rate for Longitudinally Polarized Møller Scattering	95
A.1	Elastic Electron and Proton Scattering Initial State	112
A.3	Non-relativistic Q^2	112
A.5	Proton Recoil Factor	113
A.6	Relativistic Q^2 Definition	113
A.7	Square of the Electron Momentum	113
A.8	Initial Electron Momentum	113
A.9	Final Electron Momentum	113
A.11	Q^2 of Elastically Scattered Electrons	114
A.12	Energy Transferred to the Proton from the Electron	114
A.13	Proton's Initial and Final Four-momentum	114
A.14	Bjorken x	114
A.17	Bjorken x for Elastic Scattering	115
A.19	Q^2 of Elastically Scattered Electron Independent of θ_{Lab}	115
A.20	E and E' as a Function of Q^2	115
A.22	Q^2 of Elastically Scattered Electron Independent of E	116
A.23	Four Equivalent Forms of Q^2 for Elastically Scattered Electrons in the Relativistic Limit	116
B.1	Hamiltonian for Hydrogen with Raising and Lowering Operators . .	117
B.2	Eigenvalues for Hydrogen	118

B.3	Matrix Representation for Hydrogen	118
B.4	Energies of the Hydrogen Eigenstates	118
B.5	Hydrogen's Four Eigenstates and Energies	119
C.1	Four-momentum for the Initial State Electrons in Møller Scattering	120
C.2	Energy in the Center of Mass Frame	121
C.3	Velocity in the Lab Frame	121
C.4	The γ Factor in the Center of Mass Frame	121
C.5	Four-momentum in the Center of Mass Frame	121
C.6	Momentum in the Center of Mass Frame	121
C.7	Final States Four-momenta	122
C.8	The Final state Four-momenta in Lab Frame	122
C.9	Relationship Between the Lab and Center of Mass Scattering Angles	122
C.10	The Lab Scattering Angle for Maximum Analyzing Power	123
C.11	Total Analyzing Power for Møller Scattering where the Beam and Target are Polarized in a Combination of Directions	123
C.12	Relativistic Limit of the Total Analyzing Power for Møller Scattering where the Beam and Target are Polarized in a Combination of Directions	125
C.13	Simplified Relativistic Limit of the Total Analyzing Power for Møller Scattering Where the Beam and Target are Polarized in a Combination of Directions	125
D.1	Rate	126
D.3	Luminosity	126
D.4	Flux of the Beam Normalized to the Beam Current	127
D.5	Number of Scattering Centers in the Target	127
D.6	Luminosity Normalized to the Current, for a Hydro-Møller Target .	127
D.11	Measured Asymmetry in Terms of Electrons Counted in each Helicity States	129
D.12	Error on A_{msr}	129
D.13	Partial Derivatives of A_{msr} with respect to n_+ and n_-	129
D.14	Relative Error on A_{msr} with Respect to n_+ and n_-	129
D.15	n_- and n_{tot} in terms of n_+	130
D.16	dn_+ , dn_- and dn_{tot} in terms of n_+	130
D.17	Error on the A_{msr} in terms of n_{tot}	130
D.18	dA_{msr} in terms of n_{tot}	130
D.19	Relative Uncertainty on A_{msr} in terms of n_{tot}	130

Chapter 1

Introduction

This dissertation is on two projects, which are both related to parity-violating electron scattering. The first chapters deal with the Q_{weak} experiment which was conducted at the medium energy electron accelerator, Thomas Jefferson National Accelerator Facility (Jefferson Lab or simply JLab) for two years ending in 2012. It had the goal of measuring the weak charge of the proton at low momentum transfer by scattering polarized electrons off of protons. For this I will present my work on finding the momentum transfer from the electron to the proton for the experiment.

The second half is on the Atomic Hydrogen Møller Polarimeter or “Hydro-Møller”, a new technique proposed by E. A. Chudakov and V. G. Luppov [1, 2], which would improve the present methods of measuring the polarization of an electron beam through Møller scattering from a target made of monatomic hydrogen (H) gas. This polarimeter would be useful in future electron scattering experiments at JLab and the MAMI accelerator at the Johannes Gutenberg University, Mainz in Germany. The Johannes Gutenberg University, Mainz is building a new Mainz Energy Recovery Superconducting Accelerator (MESA) which will host a future proton weak charge experiment, called the P2 experiment. At JLab, the MOLLER experiment will make a measurement of the electron’s weak charge. In order to meet their precision goals, both experiments require precise measurements of the electron beam polarization, for which a Hydro-Møller would be very beneficial.

Chapter 2 will discuss the Standard Model (SM), specifically introducing the electro-weak interaction. A basic overview of the elements of the Q_{weak} experimental apparatus relevant to my work is included in Chap. 3. Analysis of the momentum transfer is discussed in Chap. 4. How this result impacts the final results of the Q_{weak} experiment is discussed in Chap. 5.

The last three chapters are related to the Hydro-Møller. An overview on Møller and Compton polarimetry and the proposed Hydro-Møller apparatus are in Chaps. 6 and 7 respectively. Finally the Monte Carlo for the Hydro-Møller, HMolPol and the initial analysis done with it is discussed in Chap. 8.

Chapter 2

Theory of Weak Charges

2.1 Theory of the Standard Model

There are four known fundamental forces: gravity, electromagnetism, the strong and weak nuclear forces. The Standard Model (SM) is a quantum field theory based on gauge symmetries, and has been very successful in describing the interactions of fundamental particles through the latter three fundamental forces. It does this through combining the strong nuclear force, $SU(3)_C$, with the electroweak $SU(2)_L \times U(1)_Y$ gauge groups.

The SM includes three main groups of particles: gauge bosons, quarks, and leptons. Bosons are integer spin particles, while quarks and leptons are fermions which have half-integer spin. The gauge bosons are spin 1, and mediate a force: the electromagnetic (photon, γ), the weak (Z and W^\pm bosons), and the strong (gluons, g). There are three different generations of quarks and leptons which are shown from left to right in Fig. 2.1. Three of the six leptons, the electron (e^-), muon (μ^-), and tau (τ), couple to all the force carriers in the SM but gluons. These leptons have corresponding neutrinos, ν_e , ν_μ , and ν_τ which only interact through the weak interaction, as they carry no electric charge or color.

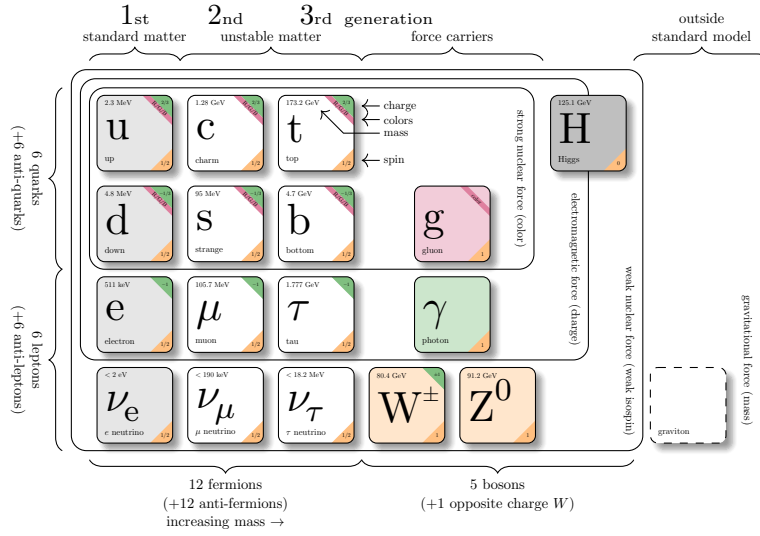


Figure 2.1: Diagram of the fundamental particles described by the SM. Reproduced from [3] with original from [4].

For a fermion, the Dirac Lagrangian is

$$\mathcal{L}_{\text{Dir}} = \bar{\psi}(i\gamma^\mu \partial_\mu - m)\psi, \quad (2.1)$$

where ψ and m are the wave function and mass of the fermion respectively and γ^μ are the gamma matrices for $\mu \in [0, 3]$. This Lagrangian is invariant under the global gauge transformation by a constant phase of ϕ , *i.e.* $\psi \rightarrow e^{i\phi}\psi$. However, for a similar local transformation where ϕ is dependent on the position and time $\phi \rightarrow \phi(t, \vec{x})$, the Lagrangian is no longer invariant. By introducing a gauge field, A_μ , with the coupling g and using the covariant derivative in Eq. 2.2 in place of the derivative, the Lagrangian stays invariant:

$$D_\mu \equiv \partial_\mu - igA_\mu. \quad (2.2)$$

The gauge field must also transform to remove the unwanted terms created through adding it in,

$$A_\mu \rightarrow A_\mu + \frac{1}{g}\partial_\mu \phi(t, \vec{x}). \quad (2.3)$$

For a more in depth look at the information in this chapter see [5–9].

2.2 Parity Violation

Parity is the discrete inversion of spatial coordinates *i.e.* $(x, y, z) \rightarrow (-x, -y, -z)$, and can be thought of as a mirror reflection. For particles the quantum number of the parity operator is the particle's handedness, or a particle's chirality, or in the relativistic limit its helicity. Helicity, h , is the product of the particle's momentum, \vec{p} and its spin, \vec{s} . When these are parallel the particle is right handed or has positive helicity, and when they are anti-parallel the particle is left handed or has negative helicity,

$$h \equiv \vec{s} \cdot \vec{p} = \begin{cases} > 0 & \text{positive helicity} \\ < 0 & \text{negative helicity} \end{cases} . \quad (2.4)$$

Parity violation in the weak interaction was first observed by C.S. Wu *et al.* in 1957 [10], and until then parity was believed to be conserved. Wu and collaborators measured the electron from β -decay¹ in ^{60}Co , where they aligned the spin of the nucleus with a magnetic field. If parity is conserved the same number of electrons would be emitted parallel and anti-parallel to the magnetic field. However Wu observed that most of the electrons were emitted anti-parallel to the spin of the nucleus, a clear violation of the conservation of parity in the weak interaction.

In the SM parity violation is incorporated through the left-handed doublet and right-handed singlet, which for the case of the electron is

$$\begin{aligned} \text{Left-Doublet: } & \begin{pmatrix} e^- \\ \nu_e \end{pmatrix} . \\ \text{Right-Singlet: } & e^- \end{aligned} \quad (2.5)$$

The doublet state has a weak isospin of $1/2$, and the singlet has a weak isospin of 0 .

¹ β -decay equation: $^{60}\text{Co} \rightarrow ^{60}\text{Ni} + e^- + \bar{\nu}_e$

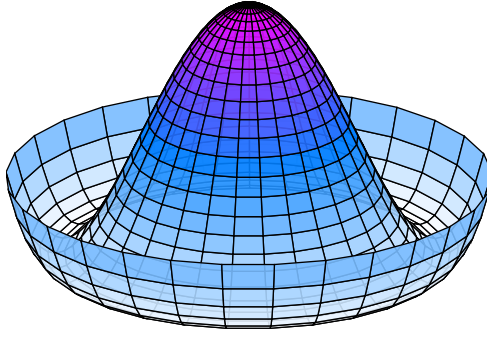


Figure 2.2: The Higgs potential, with arbitrary constants.

2.3 Electroweak Theory

The $SU(2)_L \times U(1)_Y$ is the gauge theory that combines the electromagnetic and weak interactions together, and was proposed by S. L. Glashow [11], A. Salam [12], and S. Weinberg [13] in the late 1960's.

The SM Lagrangian (\mathcal{L}_{SM}) is

$$\mathcal{L}_{\text{SM}} = \mathcal{L}_{\text{gauge}} + \mathcal{L}_{\text{f}} + \mathcal{L}_{\text{Higgs}} + \mathcal{L}_{\text{Yuk}}, \quad (2.6)$$

which is the sum of the gauge, fermion, Higgs, and Yukawa sectors of the SM theory, respectively. The Higgs part of \mathcal{L}_{SM} through symmetry breaking gives rise to the mass of the W^\pm and Z^0 , and will be discussed in Sec 2.3.1; the other parts of \mathcal{L}_{SM} are beyond the scope of this dissertation. The Higgs part of the SM Lagrangian is

$$\mathcal{L}_{\text{Higgs}} = (D_\mu \Psi)^\dagger (D^\mu \Psi) - V(\Psi^\dagger \Psi), \quad (2.7)$$

where $V(\Psi^\dagger \Psi)$ is the potential term. The Higgs potential is illustrated in Fig. 2.2 and has the form

$$V(\Psi^\dagger \Psi) = -\mu^2 \Psi^\dagger \Psi + \lambda (\Psi^\dagger \Psi)^2. \quad (2.8)$$

For this to be gauge invariant, the electroweak gauge group has a covariant derivative given by

$$D_\mu = \partial_\mu + i\frac{g}{2}\sigma^a W_\mu^a + i\frac{g'}{2}B_\mu, \quad (2.9)$$

where W_μ^a and B_μ , respectively, are the $SU(2)_L$ and $U(1)_Y$ bosons, σ^a are the Pauli matrices ($a \in [1, 3]$), and g and g' are the gauge coupling constants.

2.3.1 Spontaneous Symmetry Breaking

Through the Higgs mechanism the electroweak theory goes through spontaneous symmetry breaking which leads to the weak force bosons, W^+ , W^- , Z^0 which have mass, and the electromagnetic massless boson, the photon, γ . The complex scalar Higgs field, Ψ for Eq. 2.7 is a doublet defined as

$$\Psi = \begin{pmatrix} \psi^+ \\ \psi^0 \end{pmatrix} = \begin{pmatrix} \frac{1}{\sqrt{2}}(\psi_1 + i\psi_2) \\ \frac{1}{\sqrt{2}}(\psi_3 + i\psi_4) \end{pmatrix}, \quad (2.10)$$

where $\psi_i = \psi_i^\dagger$ for $i \in [1, 4]$ are the four basis Hermitian fields.

One can choose the minimum potential in terms of the vacuum expectation value, v , to be

$$\Psi = \frac{1}{\sqrt{2}} \begin{pmatrix} 0 \\ v \end{pmatrix} \quad (2.11)$$

and therefore

$$\langle \Psi \rangle^2 = \frac{v^2}{2}.$$

In the case of $\mu^2 < 0$, the minimum potential which is at $v = 0$ is stable and the $SU(2)_L \times U(1)_Y$ symmetry is not broken. However if $\mu^2 > 0$, $v = 0$ is not stable and symmetry breaking can take place, and in order for the vacuum to be stable one must have $\lambda > 0$. Using Eqs. 2.8 and 2.11, $v = \sqrt{\mu^2/\lambda}$.

The gauge terms of the Higgs part of the SM Lagrangian² implicitly includes the information on the weak and electromagnetic bosons. Then the covariant derivative of

²The second two terms of the covariant derivative in Eq. 2.9.

Ψ as defined in Eq. 2.11 becomes

$$\begin{aligned} D_\mu \Psi &= \frac{i}{2\sqrt{2}} \begin{pmatrix} gW_\mu^3 - g'B_\mu & g(W_\mu^1 + W_\mu^2) \\ g(W_\mu^1 - W_\mu^2) & -gW_\mu^3 + g'B_\mu \end{pmatrix} \begin{pmatrix} 0 \\ v \end{pmatrix} \\ &= \frac{iv}{2\sqrt{2}} \begin{pmatrix} g(W_\mu^1 + W_\mu^2) \\ -gW_\mu^3 + g'B_\mu \end{pmatrix}. \end{aligned} \quad (2.12)$$

To find the mass of W^\pm , Z^0 , and γ , the following definitions are commonly made³,

$$W_\mu^\pm = \frac{W_\mu^1 \mp iW_\mu^2}{\sqrt{2}} \quad (2.13)$$

$$Z_\mu = \frac{gW_\mu^3 + g'B_\mu}{\sqrt{g^2 + g'^2}} \quad (2.14)$$

$$A_\mu = \frac{g'W_\mu^3 + gB_\mu}{\sqrt{g^2 + g'^2}} \quad (2.15)$$

The W_μ^\pm corresponds to the weak charge-current interaction (W^\pm), the Z_μ corresponds to the weak neutral current interaction (Z^0), and A_μ corresponds to the electromagnetic interaction (γ). With the definitions in Eqs. 2.13, 2.14 and 2.15, $(D_\mu \Psi)^\dagger (D^\mu \Psi)$ becomes

$$\begin{aligned} (D_\mu \Psi)^\dagger (D^\mu \Psi) &= \frac{v^2 g^2}{4} |W_\mu^\pm|^2 + \frac{v^2 (-gW_\mu^3 + g'B_\mu)^2}{8} \\ &= \left(\frac{gv}{2}\right)^2 W_\mu^+ W^{-\mu} + \frac{1}{2} \left(\frac{v\sqrt{g^2 + g'^2}}{2}\right)^2 Z_\mu Z^\mu. \end{aligned} \quad (2.16)$$

From Eq. 2.16 the masses of the W^\pm , Z^0 , and γ can be picked off from the coefficients of each term respectively,

$$m_{W^\pm} = \frac{gv}{2}, \quad m_{Z^0} = \frac{v\sqrt{g^2 + g'^2}}{2}, \quad m_\gamma = 0. \quad (2.17)$$

The coefficient m_γ comes from there being no $A_\mu A^\mu$ term. The predicted masses of

³As seen in textbooks *e.g.* Peskin & Schroeder [9] and Langacker [6].

the W^\pm and Z^0 agree well with the measured values of $m_W \approx 80 \text{ GeV}$ and $m_Z \approx 91 \text{ GeV}$ [14].

While W^\pm is directly related to W_μ^1 and W_μ^2 as illustrated in Eq. 2.13, this is not the case for W_μ^3 and B_μ and Z^0 and γ . There is a mixing between W_μ^3 and B_μ which leads to the weak mixing angle or Weinberg angle (θ_W), defined by

$$\tan \theta_W = \frac{g'}{g}, \quad \cos \theta_W = \frac{g^2}{\sqrt{g^2 + g'^2}}, \quad \sin \theta_W = \frac{g'}{\sqrt{g^2 + g'^2}}. \quad (2.18)$$

The denominator, $\sqrt{g^2 + g'^2}$ is also often defined as g_Z . It is often more useful to have the Weinberg angle in terms of the mass of W and Z bosons,

$$\sin^2 \theta_W = 1 - \left(\frac{m_W}{m_Z} \right)^2. \quad (2.19)$$

Using the Weinberg angle, Eqs. 2.14 and 2.15 can be rewritten as

$$Z_\mu = \cos \theta_W W_\mu^3 - \sin \theta_W B_\mu \quad (2.20)$$

$$A_\mu = \sin \theta_W W_\mu^3 + \cos \theta_W B_\mu. \quad (2.21)$$

Adding a small perturbation of a neutral Higgs field ($h(x)$) to the vacuum expectation value can give the fermions mass; doing this Eq. 2.11 then becomes

$$\Psi = \frac{1}{\sqrt{2}} \begin{pmatrix} 0 \\ v + h(x) \end{pmatrix}. \quad (2.22)$$

With the addition of $h(x)$ the above formalism stays intact, but now there is a Higgs coupling which is part of an $SU(2)_L$ doublet. Neutrinos which do not have a right handed singlet state, are massless⁴, while the other fermions have a mass proportional to their coupling. Details on the Higgs sector and neutrino masses are outside the

⁴Experiments have observed that neutrinos oscillate between ν_e , ν_μ , and ν_τ , and therefore must have mass. Since neutrinos are not massless, the SM needs to be extended, but this is outside the scope of this dissertation.

scope of this dissertation.

2.3.2 Neutral Current

The neutral current interaction is an exchange of a Z^0 or γ , as illustrated in Fig. 2.3.

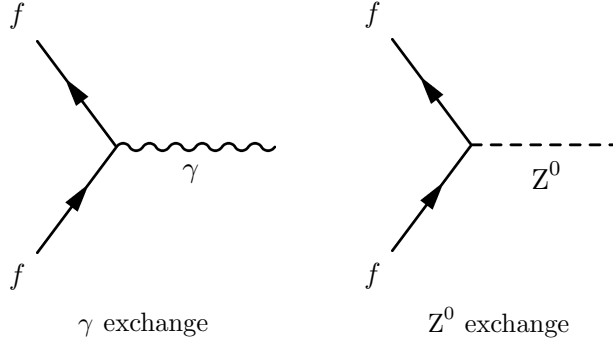


Figure 2.3: Neutral current exchange diagrams for both the electromagnetic and weak exchange.

The neutral current for the Z^0 is

$$\begin{aligned} J_\mu^{Z^0} &= g \cos \theta_W J_\mu^{W^3} - g' \sin \theta_W \frac{J_\mu^Y}{2} \\ &= \frac{e}{\sin \theta \cos \theta} \left[J_\mu^{W^3} - \sin^2 \theta_W J_\mu^\gamma \right] \end{aligned} \quad (2.23)$$

and for the γ is

$$J_\mu^\gamma = \bar{\psi} \gamma_\mu Q \psi, \quad (2.24)$$

which is dependent on the current of the charge operator (Q), the hypercharge (Y) and W_μ^3 . The current for W_μ^3 is

$$\begin{aligned} J_\mu^{W^3} &= \bar{\psi} T^3 \gamma_\mu (1 - \gamma_5) \psi \\ &= \bar{\psi}_L T^3 \gamma_\mu \psi_L. \end{aligned} \quad (2.25)$$

The charge-current weak interaction only interacts with left-handed particles, as can be seen in Eq. 2.25⁵, where the third component of the weak isospin is T^3 . The

⁵This is through the left and right parity operators $P_L = (1 - \gamma^5)/2$ and $P_R = (1 + \gamma^5)/2$.

hypercharge is related to Q and T^3 by

$$Q = T^3 + \frac{Y}{2}. \quad (2.26)$$

Therefore the current for Y is

$$\begin{aligned} J_\mu^Y &= \bar{\psi} Y \gamma_\mu \psi \\ &= \bar{\psi} (2Q - 2T^3) \gamma_\mu \psi. \\ &= 2J_\mu^Q - 2J_\mu^{T^3} \end{aligned} \quad (2.27)$$

Unlike with W_μ^3 , J_μ^Y interacts with both left and right-handed particles. Then $J_\mu^{Z^0}$ (Eq. 2.23) can be rewritten by using Eqs. 2.25, 2.26 and 2.27 as

$$\begin{aligned} J_\mu^{Z^0} &= \frac{e}{\sin \theta_W \cos \theta_W} \left[\bar{\psi}_L \gamma_\mu (T^3 - Q \sin^2 \theta_W) \psi_L \right. \\ &\quad \left. + \bar{\psi}_R \gamma_\mu (-Q \sin^2 \theta_W) \psi_R \right]. \end{aligned} \quad (2.28)$$

Here the coefficient $e/\sin \theta_W \cos \theta_W$ is the coupling constant for the Z^0 ($g_Z = \sqrt{g^2 + g'^2}$)⁶. The neutral current is more often written in terms of the weak vector (V) and axial (A) charges of a fermion, which respectively are

$$g_V^f \equiv g_L^f + g_R^f = T^3 - 2Q \sin^2 \theta_W, \quad (2.29)$$

$$g_A^f \equiv g_L^f - g_R^f = T^3. \quad (2.30)$$

Similar to the simplification in Eq. 2.25, $J_\mu^{Z^0}$ can be written as,

$$\begin{aligned} J_\mu^{Z^0} &= g_Z \bar{\psi} \gamma_\mu \left[(T^3 - Q \sin^2 \theta_W) (1 - \gamma^5) \right. \\ &\quad \left. + (-Q \sin^2 \theta_W) (1 + \gamma^5) \right] \psi \\ &= g_Z \bar{\psi} \gamma_\mu \left[(T^3 - 2Q \sin^2 \theta_W) + \gamma^5 (-T^3) \right] \psi. \end{aligned} \quad (2.31)$$

⁶In some texts g_Z contains an extra factor of $1/2$, and therefore is defined as $e/2 \sin \theta_W \cos \theta_W$.

Therefore with Eq. 2.29 and 2.30,

$$J_\mu^{Z^0} = g_Z \bar{\psi} \gamma_\mu (g_V^f - g_A^f \gamma^5) \psi. \quad (2.32)$$

From Eq. 2.32 it is seen that the weak neutral current interacts differently with right and left-handed fermions, leading to the parity violation in the neutral current process.

Table 2.1 summarizes these values for the fundamental fermions.

Particle	Q	T^3	g_V^f	g_A^f
u, c, t	$+\frac{2}{3}$	$+\frac{1}{2}$	$\frac{1}{2} - \frac{4}{3} \sin^2 \theta_W$	$+\frac{1}{2}$
d, s, b	$-\frac{1}{3}$	$-\frac{1}{2}$	$-\frac{1}{2} + \frac{2}{3} \sin^2 \theta_W$	$-\frac{1}{2}$
ν_e, ν_μ, ν_τ	0	$+\frac{1}{2}$		$+\frac{1}{2}$
e^-, μ^-, τ^-	-1	$-\frac{1}{2}$	$-\frac{1}{2} + 2 \sin^2 \theta_W$	$-\frac{1}{2}$

Table 2.1: The SM values for the electromagnetic charge (Q), third component of the weak isospin (T^3), and the vector and axial coupling for various fermions.

2.3.3 Nucleon Weak Charge

The electromagnetic charge of a composite particle can be determined through the sum of charges of its valence quarks, $Q = \sum Q_i$. For the proton (uud) this is,

$$\begin{aligned} Q_p^{EM} &= Q_u^{EM} + Q_u^{EM} + Q_d^{EM} \\ &= \frac{2}{3} + \frac{2}{3} - \frac{1}{3} \\ &= 1. \end{aligned} \quad (2.33)$$

Likewise the weak charge of a composite particle is defined as the sum of its vector couplings (g_V^f) at tree level. For the proton this is,

$$\begin{aligned}
Q_p^Z &= Q_W^p = Q_u^Z + Q_u^Z + Q_d^Z \\
&= g_V^u + g_V^u + g_V^d \\
&= \left(\frac{1}{2} - \frac{4}{3} \sin^2 \theta_W \right) + \left(\frac{1}{2} - \frac{4}{3} \sin^2 \theta_W \right) \\
&\quad + \left(-\frac{1}{2} + \frac{2}{3} \sin^2 \theta_W \right) \\
&= 1 - 4 \sin^2 \theta_W
\end{aligned} \tag{2.34}$$

Similarly the weak charge of the neutron (at tree level), $Q_n^Z = -1$, and for the electron, $Q_e^Z = 1 - 4 \sin^2 \theta_W$.

When looking at certain energy scales often it is useful to use an effective theory, which allows for interactions and particles that are too heavy to directly produce to be integrated out, reducing an interaction to an effective one; for a fermion scattering experiment this is a four-fermion effective interaction. For energies $\ll m_Z$, most of the weak couplings are due to virtual Z^0 s, which allows for an effective Lagrangian to be defined,

$$\mathcal{L}_{eff}^{Z^0} = \frac{G_F}{\sqrt{2}} J_\mu^{Z^0} J_{Z^0 \mu} \tag{2.35}$$

where the Fermi coupling constant, G_F , is defined by, $G_F/\sqrt{2} = g^2/8m_Z^2$. Using this, along with Eq. 2.32, a neutral current Lagrangian can be defined for a composite particle, details which are outside the scope of this dissertation and can be found in the resources referenced at the beginning of this chapter and [15, 16]. For composite particles like a nucleus the weak charge of the particle can be determined in a similar method. The parity-violating part of the neutral current Lagrangian (\mathcal{L}_{NC}) is then

$$\mathcal{L}_{NC} = -\frac{G_F}{\sqrt{2}} \sum_{i=u,d} \left[C_{1i} \bar{e} \gamma_\mu \gamma^5 e \bar{q}_i \gamma^\mu q_i + C_{2i} \bar{e} \gamma_\mu e \bar{q}_i \gamma^\mu \gamma^5 q_i \right], \tag{2.36}$$

where C_{1i} is the weak quark-vector, electron-axial coupling and C_{2i} weak electron-

vector, quark-axial coupling. At tree level in the SM these are,

$$C_{1u} = -\frac{1}{2} + \frac{4}{3} \sin^2 \theta_W, \quad C_{2u} = -\frac{1}{2} + 2 \sin^2 \theta_W \quad (2.37)$$

$$C_{1d} = \frac{1}{2} - \frac{2}{3} \sin^2 \theta_W, \quad C_{2d} = \frac{1}{2} - 2 \sin^2 \theta_W. \quad (2.38)$$

Using these, Q_W^p can be rewritten as,

$$Q_W^p = -2(2C_{1u} + C_{1d}) \quad (2.39)$$

2.4 Why Study Physics Beyond the Standard Model

Based on various observations, it is known that the SM is incomplete, making it important to both test predicted values of the SM and search for physics beyond the SM. As stated before, the SM does a very good job at describing the electromagnetic, strong, and weak forces, however it does not include gravity. The dark matter and dark energy which make up most of the universe also are not included in the SM [17, 18]. Neutrinos oscillate between their different flavors, therefore they must have mass; however this is not the case in the SM, so again it can't be complete. It is also unknown if neutrinos are Dirac or Majorana particles⁷.

Along with the observations that are missing from the SM, another reason why the SM is considered to be incomplete is the large number of adjustable parameters. Exactly how many of these parameters there are depends on what one considers a parameter, but they can include masses, coupling constants, mixing angles, and number of generations of fermions. Fundamental theories ideally are simple and elegant, so the ultimate theory would have only a few input parameters, ideally one.

Experiments like the Q_{weak} experiment look for physics beyond the SM indirectly, by making measurements of constants precisely predicted by the SM. While the Q_{weak} experiment measured Q_W^p , other experiments measure the weak charge of the electron, Q_W^e (E158 experiment [19] and MOLLER experiment). Other experiments test the

⁷Majorana particles are their own antiparticle, unlike Dirac particles.

SM by directly looking for various predictions of the SM, like the Higgs boson or new fermions and gauge bosons not in the SM. In 2012 at the Large Hadron Collider⁸ (LHC) accelerator at the European Organization for Nuclear Research (CERN) in Geneva, Switzerland both the ATLAS [20] and Compact Muon Solenoid (CMS) experiment [21] independently detected the Higgs boson.

More information on physics beyond the SM can be found in [6–8].

2.5 Theory of Q_{weak}

The Q_{weak} experiment [22] performed a precision measurement of the weak charge of the proton, Q_{W}^{P} . The Standard Model predicts a small value for $Q_{\text{W}}^{\text{P}} \approx 0.07$. Because this value is so small, a precise measurement of Q_{W}^{P} provides an attractive indirect way of looking for physics beyond the Standard Model.

Using the integrated output signal from the main detectors, the measured asymmetry, A_{msr} was calculated from the helicity-dependent difference over the sum of the cross section (σ)

$$A_{msr} = \frac{\sigma_+ - \sigma_-}{\sigma_+ + \sigma_-}, \quad (2.40)$$

This then is used with Eq. 2.41 and the value of Q^2 to calculate Q_{W}^{P} [23].

In order to measure Q_{W}^{P} , we must measure the parity-violating asymmetry from scattering electrons of different helicities from a proton. The parity-violating asymmetry is related to the weak charge of the proton through the following equation⁹:

$$A_{ep} = \frac{-G_F Q^2}{4\pi\alpha\sqrt{2}} \left\{ Q_{\text{W}}^{\text{P}} + B(\theta, Q^2) Q^2 \right\} \quad (2.41)$$

where, α is the fine structure constant, Q^2 is the four-momentum transfer squared, and $B(\theta, Q^2)$ are higher-order corrections due to hadronic effects. Because of the relationship between Q^2 and the asymmetry, it is important that both the asymmetry

⁸These are often referred to as the “energy frontier” rather than the “precision frontier”.

⁹This is sometimes written in terms of the reduced asymmetry, A_{ep}/A_0 . Here $A_0 = -G_F Q^2 / 4\pi\alpha\sqrt{2}$, then $A_{ep}/A_0 = Q_{\text{W}}^{\text{P}} + B(\theta, Q^2) Q^2$.

and Q^2 be measured precisely. The determination of Q^2 for the Q_{weak} experiment is one of the major topics of this dissertation.

Chapter 3

Q_{weak} Experiment Apparatus

3.1 Jefferson Lab Overview

The Q_{weak} experiment was executed in experimental Hall C at the Thomas Jefferson National Accelerator Facility (Jefferson Lab or simply JLab) in Newport News, Virginia. At the time of the Q_{weak} experiment JLab had three experimental halls; A, B, and C. The halls are at the end of the Continuous Electron Beam Accelerator Facility (CEBAF) which has two antiparallel linear accelerators (linacs) that deliver the electron beam to each of the experimental halls. The electrons are accelerated in each linac consisting of 20 superconducting radio-frequency (RF) cryogenically cooled modules (cryomodules). The cryomodules operate at 1497 MHz, with an average accelerating gradient of 8.4 MV m^{-1} [24]. The two linacs are connected via bending magnets that allow the electron beam to travel up to 5 times around, for a maximum beam energy of 6 GeV; upon leaving the accelerator the electron beams are separated and sent to their respective halls. An illustration of the layout of CEBAF is in Fig. 3.1. More information on CEBAF can be found in Refs. [24, 25].

The Q_{weak} experiment utilized Hall C, requiring the two standard Hall C spectrometers be moved out of the way of the custom experimental apparatus used in the Q_{weak} experiment, which is described in Sec. 3.3.

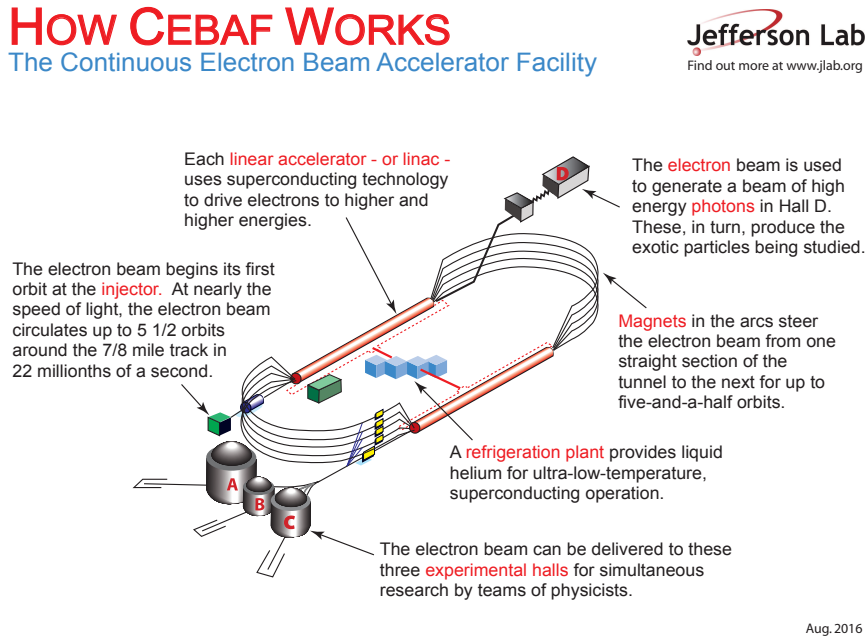


Figure 3.1: Cartoon describing how CEBAF works. Hall D was added after the Q_{weak} experiment ran [26].

3.2 Q_{weak} Experiment Requirements

Since the Q_{weak} experiment is aimed at making a precise measurement of Q_W^{P} , the Q_{weak} Collaboration must consider how to minimize all sources of experimental uncertainty. For all precise measurements a crucial necessity is to have large statistics and the Q_{weak} experiment is no different. In turn, the Q_{weak} experiment required 2 years on the floor with about 15 months of data taking at JLab, a high beam current, a thick target, and an efficient detection system covering a large acceptance.

The Q_{weak} experiment required an electron beam that is highly polarized, and it is important that the polarization be measured precisely. The polarization of the beam was determined through both Møller and Compton polarimetry¹ during the Q_{weak} experiment. The Møller measurement is invasive to an experiment where the Compton measurement is not. They have very different systematic uncertainties therefore these two can be used as a cross-check for each other.

¹Møller and Compton polarimetry are explained in Chap. 6.

As mentioned in Chap. 2, in order to make the measurement of Q_{W}^{P} , the helicity difference over the sum of the cross section is needed. In order to achieve this, the helicity of the beam must be reversed throughout the experiment²; this was done at 960 Hz.

The momentum transfer (Q^2) is also crucial as can be seen in Eq. 2.41, as it multiplies Q_{W}^{P} , and therefore needs to be measured as precisely as possible. The SM prediction of Q_{W}^{P} is at $Q^2 = 0$, but in an electron-scattering experiment this is not practical. A small Q^2 experiment suppresses the second term in Eq. 2.41 (the “ B ” term) therefore the Q_{weak} experiment was designed to have a low Q^2 , which needed to be measured precisely.

For more details on the requirements of the Q_{weak} experiment see [27].

3.2.1 Integration Mode vs. Tracking Mode

The Q_{weak} experiment had two data-taking “modes”: the integration mode, which was the main part of the experiment, and tracking mode which was used to measure Q^2 .

During the main part of the experiment the beam current was as large as $180 \mu\text{A}$ [28]; at this current individual electrons can not be detected without significant deadtime and pileup. The electrons came into the detectors at such a rate that the signals from individual electrons overlapped each other, as illustrated in Fig. 3.2. This means that in order to get the total signal seen by the main detector (MD) bars from the electrons the signal must be integrated over the helicity window.

The overlap in the signal of the electron make it impossible for the tracking chambers to be used during this time, as they need to be able to distinguish between different electrons, and would trip off from being overloaded, as is illustrated in Fig. 3.2. Therefore in order to track individual electrons, the beam current was decreased to currents between 50 pA and 200 nA [28], depending on the particular study. At these currents the tracking chambers are not overloaded, so tracking the path of an individual

²This can be done by flipping the spin of the electron while the momentum stays the same; the other option would be to change the momentum while the spin stays constant. The latter is impractical as it would require changing the direction of the accelerator.

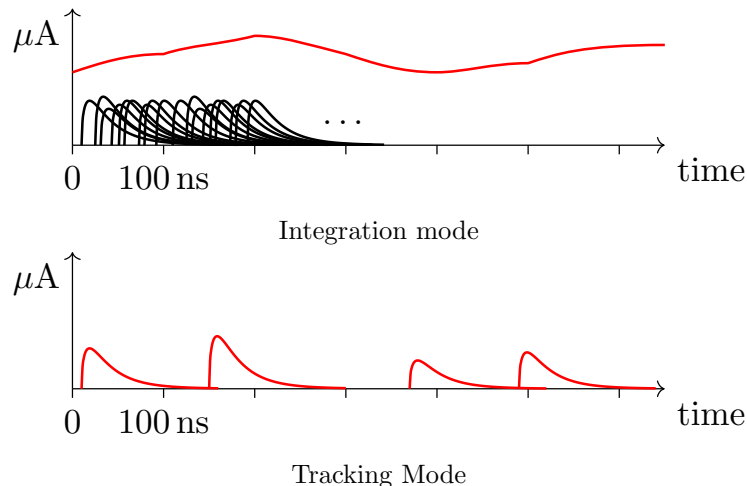


Figure 3.2: Data collection for integration mode (top) compared to tracking mode (bottom) [29]. During integration mode electrons go through the MD so fast information on them individually can't be gathered, therefore requiring integration of the signal (in red on top). In event mode this is not the case, and individual events can be recorded.

electron can be found, as explained in Sec. 3.3.5.

3.3 Q_{weak} Experiment Apparatus

The Q_{weak} experiment ran at JLab for two years, finishing in May 2012. The Q_{weak} experiment (see Fig. 3.3) used a 89% polarized 1.16 GeV electron beam scattering off a liquid hydrogen target (LH_2). Collimators were used to select the elastically scattered electrons with a low Q^2 . They also defined an area of acceptance that corresponds to the solid angle acceptance associated with the main detector bars (MDs). Following three collimators there was the Q_{weak} toroidal magnet (QTor) which was used to select the elastically scattered electrons and direct them to the main detector bars.

During specific points in the experiment the beam current was decreased and drift chambers were placed in the paths of the scattered electrons for the tracking part of the experiment. There were horizontal drift chambers (HDCs) between the set of collimators near the target, and right before the MDs there was a set of vertical drift chambers (VDCs) and a trigger scintillator. These are the elements that will be concentrated on here, as they are most relevant for the Q^2 analysis.

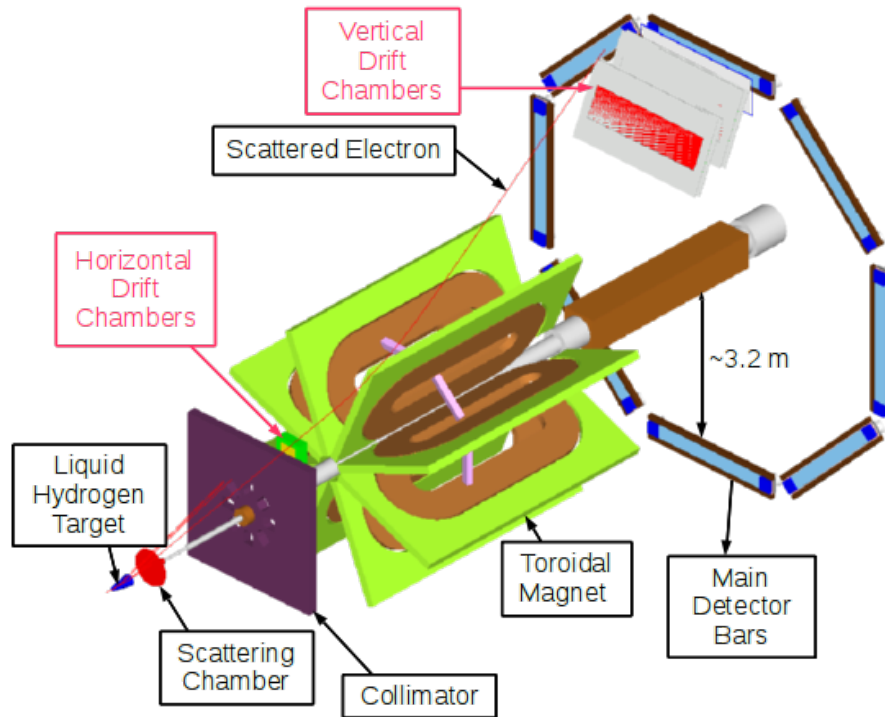


Figure 3.3: Layout of the Q_{weak} experiment, with the tracking system inserted, which is labeled in red. The electron beam (red) comes in from the left, hitting the LH_2 target. The scattered events travel through collimators and the toroidal magnetic field, finally reaching the main detectors. During the tracking measurements the horizontal drift chambers were placed after the initial collimators and the vertical drift chambers were placed right before the main detectors.

Figure 3.3 shows a schematic of the experimental setup during the tracking period of the experiment. A full description of the Q_{weak} experiment's layout and operating principle can be found in [28].

3.3.1 Target

The Q_{weak} experiment used a liquid hydrogen target, which was 34.4 cm long and held ≈ 58 L of liquid, which was cooled to 20 K. The $180 \mu\text{A}$ beam deposited 2.1 kW in the target. The entrance and exit windows to the target were made of Al, and were 0.097 mm and 0.64 mm thick respectively. The beam was rastered uniformly over a $4 \text{ mm} \times 4 \text{ mm}$ area on the target entrance window to help prevent damage to the windows and boiling of the LH_2 [28].

3.3.2 The QTor Magnetic Spectrometer

The Q_{weak} experiment used a normal conducting toroidal magnet (QTor) which was centered around the beam line and sat 6.5 m downstream of the target between the tracking chambers, as seen in Fig 3.4. This was used to select and direct the elastic ep scattered electrons on to the center of the MDs, as seen in Fig. 3.5. Background processes like inelastic scattering were deflected away from the MDs, which reduced the asymmetries measured by the MDs for those interactions [28].



Figure 3.4: Picture of the Q_{weak} experiment during the installation. The target is on the left, followed by two lead collimators, one on each side of the man in the photo. A third collimator sits right in front of the large frame in the center of the photo is the QTor magnetic with its eight coils. After QTor on the right three of the eight quartz main detector bars are visible.

3.3.3 Collimators

The Q_{weak} experiment had three lead antimony (95.5% Pb, 4.5% Sb) collimators, each with eight holes for the electrons to travel through to the MDs. The first and third collimator had the primary purpose of reducing backgrounds. They were located 74 cm

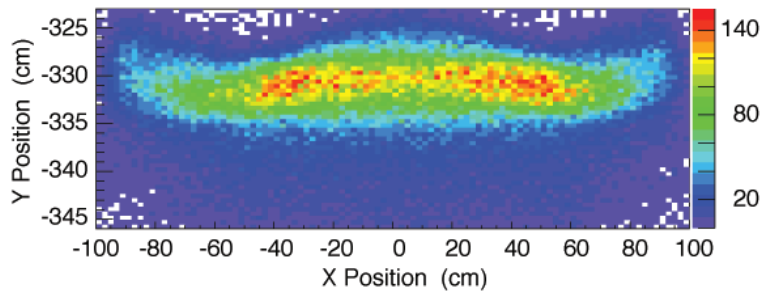


Figure 3.5: Scattered electron tracks, found using the VDCs, projected to a typical MD. The \hat{x} -axis is the horizontal direction and the \hat{y} -axis is the vertical direction and the color scale is the relative flux. The “moustache” shape illustrates the focusing of the electrons on the MDs due to the QTor magnetic field.

and 3.82 m downstream of the target respectively. The second or primary collimator defined the acceptance of the scattered electrons, 49% in ϕ with an acceptance in θ of 5.8° to 10.2° and 6.6° to 11.6° on the upstream and downstream sides of the collimator respectively, therefore, there was a total θ acceptance of 6.6° to 10.2° . All three of these collimators can be seen in Fig. 3.4. For more information see [28].

3.3.4 Main Detectors

The Q_{weak} experiment used 8 main detector (MD) Cherenkov bars laid out in the shape of an octagon to use symmetry to help decrease false asymmetries from a transverse component in the beam polarization and shifts in the beam position and angle that could be helicity correlated. Figure 3.6 shows how the MDs are numbered in the Q_{weak} experiment.

Cherenkov radiation happens when a charged particle travels through a medium at a speed faster than the speed of light in that medium. This creates a light cone which is illustrated in Fig. 3.7³.

Each MD consisted of two $100\text{ cm} \times 18\text{ cm} \times 1.25\text{ cm}$ non-scintillating artificial quartz bars glued together [28]. The lack of scintillation of the artificial quartz bars makes them relatively insensitive to neutral backgrounds [30]. Another way soft neutral backgrounds like low energy photons were suppressed through the use of the 2 cm Pb

³This is analogous to a sonic boom.

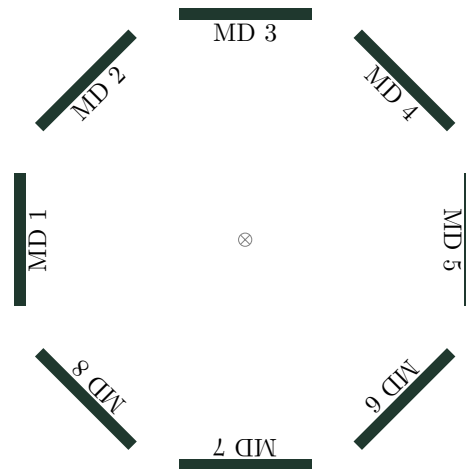


Figure 3.6: The numbering scheme of the MDs in the Q_{weak} experiment viewed from upstream.

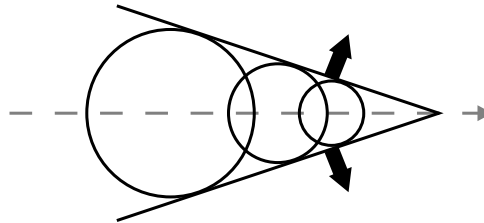


Figure 3.7: Illustration of Cherenkov Radiation: As a particle (in gray) travels through a medium faster than the speed of light in the medium, it creates a light cone behind it.

pre-radiator installed in front of each MD. These also increased the light yield in the MDs by creating a shower of electrons and photons which then travels into the MDs.

Each side of the MDs had a 130 mm photomultiplier tube (PMT) attached to it. These collected the photons created by the electrons in the MDs and read them out as an analog signal; this was then converted into a digital signal by a low-noise Analog-to-Digital Converter (ADC). A full description of the MDs can be found in Peiqing Wang's dissertation [30].

3.3.5 Tracking Chambers

During the tracking mode part of the Q_{weak} experiment there were three different detectors that were added into the experiment to gather information on the path of

the scattered electrons, as illustrated in Fig. 3.8. In order to not overload the tracking detectors, the beam current was lowered to between 50 pA and 200 nA [28]. As the electrons travel to the MDs, the first type of tracking chambers are the horizontal drift chambers (HDCs), and the second set of chambers were the vertical drift chambers (VDCs), followed directly by the trigger scintillator. The trigger scintillator, which was placed right after the VDCs, was used for timing and triggering, to know when we had an electron travel through the VDCs to the main detectors. There were only two sets of tracking chambers for each case, which were able to be rotated so they could cover all eight MDs. All of the tracking chambers were also able to move in and out of the path of the scattered electrons, in for tracking mode and out for integration mode.

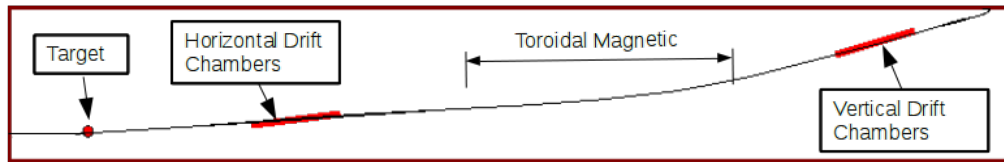


Figure 3.8: Path the electrons take from the target to the main detector bars with tracking system in place. After scattering off the target they travel through the HDCs, followed by the QTOR magnet and finally through the VDCs.

3.3.5.1 Horizontal Drift Chambers

The HDCs were built by Virginia Tech, and were placed upstream of the QTOR magnet, between a set of collimators. Two chambers made up a “package” which was then placed in an octant. Two packages, 180° , apart were then located in opposite octants. This pair of packages were placed on a rotator such that they were able to be rotated to take measurements in all eight octants. Each HDC had a transverse size of $28\text{ cm} \times 38\text{ cm}$ and consisted of six wire planes, giving 12 wire planes in each package. The six wire planes were oriented in the order of XUV and $X'U'V'$ where the U , V wires were at a $\pm 53.1^\circ$ angle to the X wires [28, 31]. The HDCs were used to take the measured scattered electrons and project them back to the target, therefore determining the scattering angle of these electrons. A full description of the HDCs can be found in Juliette Mammei’s dissertation [31].

3.3.5.2 Vertical Drift Chambers

The VDCs were built at William & Mary and were located right before the main detector bars. Like with HDCs, the VDCs are made in pairs, where a pair is called a package and were placed on a rotator so they could be placed in all eight octants. An individual VDC had a dimension of $204.5 \text{ cm} \times 53.2 \text{ cm} \times 10.2 \text{ cm}$ with 2 wire planes, each with 279 wires [28]. The two wire planes were oriented in the order of UV where the UV wires were $\pm 26.56^\circ$ from the long axis of the VDC [28, 32]. A full description of the VDC system can be found in John Leckey's [32] and Josh Hoskins' dissertations [33].

3.3.5.3 Trigger Scintillators

Besides the HDCs and the VDCs the tracking mode of the experiment included a pair of trigger scintillators. Built by George Washington University, they each consisted of a $218.45 \text{ cm} \times 30.48 \text{ cm} \times 1.00 \text{ cm}$ piece of plastic scintillator [34] one for each package. Connected to the same rotating apparatus used for the VDCs, they were situated in front of the main detectors but behind the VDCs. The trigger scintillator were used as a timing apparatus in event mode, this allowed for precisely knowing when an electron went through the VDCs. By having the time in which a scattered electron traveled through the VDCs, and using this as a reference time, the time of the hit on the wires in the drift chambers is then related to the distance of the electron's path from the given wire. These distances can then be used to find the path of the electron through the HDCs and VDCs [35]. A full description of the Trigger Scintillators can be found in Katherine Myers' dissertation [34].

3.3.6 Beam Position Monitors

The Beam Position Monitors (BPMs), were placed at various locations along the beamline, and were used in the main experiment to correct for false asymmetries due to beam motion. They consisted of two +/- pairs of stripline detectors placed at 90°

with respect to each other. In total there were 23 placed in the Hall C beam line, however 4 or 5 of them that were 1.5 m to 10.5 m upstream of the target were used to calculate the beam position and angle [28, 35]. During the tracking part of the experiment there were studies where the beam positions and angles were deliberately changed. During these studies these BPMs were used to tell where the beam was with respect to its nominal position and what angle the beam came into the target. Since the BPMs only work at high beam current ($1 \mu\text{A}$ to $180 \mu\text{A}$) this was done by raising the beam current, temporarily measuring the beam position and angle, then lowering it to take the tracking measurement.

3.3.7 Beam Current Monitors

To measure the beam current, RF cavity Beam Current Monitors (BCMs) were used. They were located 16 m, 13.4 m, and 2.7 m upstream of the target and provided a stable, low noise and continuous (non-invasive) measurement of the beam current. They were used to normalize the beam current in the asymmetry analysis part of the Q_{weak} experiment [28]. For more information on the BCMs see [28].

3.3.8 Luminosity Monitors

There were two sets of Luminosity monitors (Lumis) placed around the beamline. The upstream Lumis were placed before the primary collimator and the downstream Lumis 17 m downstream of the target. The four upstream Lumis were designed to be primarily sensitive to Møller scattering electrons with a scattering angle of $\approx 5^\circ$. They were $7 \text{ cm} \times 27 \text{ cm} \times 2 \text{ cm}$ in size and made of similar quartz to the MDs, with the short side positioned radially to the beamline. The eight downstream lumis were mainly sensitive to Møller and Mott scattering electrons at a scattering angle of $\approx 0.5^\circ$. They were made of similar quartz to the MDs, $4 \text{ cm} \times 3 \text{ cm} \times 1.3 \text{ cm}$, in size with a 45° taper at one end, and like the MDs had a 2 cm Pb pre-radiator in front to suppress low-energy backgrounds. For more information on the Lumis see [28].

Chapter 4

Tracking Mode: Data and Simulation Analysis

A crucial component in the measurement of Q_W^p is the momentum transfer to the proton from the electron (Q^2), as seen in Eq. 2.41. Therefore it is important to make as precise of a measurement of Q^2 as possible.

Throughout this chapter there are direct comparisons between data and simulation. However, one will see that there is not an exact agreement between the simulation of and data for the scattering angle, θ and therefore Q^2 . The primary cause for this is because the position and angle of the HDCs has not yet been properly calibrated and implemented in the track reconstruction software. The originally surveyed geometry of the HDCs was found to be inadequate. This was determined through projecting tracks back to a thin solid target, where it was found that different octants yielded different target positions. Work on this discrepancy is continuing by collaborator Anna Lee [36]. This still allows the comparison between data and simulation for the sensitivities of Q^2 to the many variables explored in this chapter.

The dedicated tracking periods during November 2011, January 2012 and May 2012 of the Q_{weak} experiment were used to measure and calculate the uncertainty on Q^2 . During these tracking periods the studies in this chapter were accomplished,

which included changing the beam raster size, position, and angle, along with a scan of different QTor currents. Other tracking periods in January 2011, March 2011 were used for initial commissioning of the tracking system, and no results from these times are presented here. In addition there was an April 2012 tracking period which had a higher beam energy for an ancillary measurement.

Determination of the Q^2 for the Q_{weak} experiment was done through reconstruction software used for both the data and the Q_{weak} simulation. The track reconstruction software takes the information gathered about the electron's path in the HDCs, which gives the scattering angle. Then the software extrapolates or "swims" that electron track through the magnetic field of QTor, to match up with the measured path of the electron in the VDCs, which gives the scattered electron energy. Given the scattering angle from the HDCs and the scattered electron energy one can verify that the electron was elastically scattered. Details on the track reconstruction software can be found in Siyuan Yang's dissertation [35].

4.1 Q_{weak} Experiment Simulation

The Q_{weak} experiment's simulation was written with GEANT4 C++ libraries [37]. Its detailed geometry of the Q_{weak} experiment includes a realistic QTor magnetic field, surveyed positions of the main detectors, but assumes ideal locations of the collimators. It can be used both with and without the VDCs and HDCs. When the tracking chambers are in the simulation the output from the simulation can be analyzed using the same track reconstruction software as the tracking data.

The detailed geometry includes not just the main detectors, but also the beam line, VDCs, HDCs, collimators, shielding, QTor magnet, supporting structures, and their materials. The LH_2 target is included along with the other targets such as Al targets that were used for different studies that are beyond the scope of this dissertation.

While this dissertation is concentrated on elastic scattering off of LH_2 , the simulation however is not limited to just this. It includes elastic scattering off of ^{27}Al , Møller

scattering, inelastic scattering off the LH_2 ($\text{N} \rightarrow \Delta$ resonance), and inelastic and quasi-elastic scattering off of ^{27}Al . The simulation also generates and tracks the optical photons created by the Cherenkov effect in the MDs, and determines their signals as seen by the PMTs.

4.2 Measured Q^2 vs. Interaction Q^2

For elastic scattering the square of the four-momentum transfer, Q^2 can be found by:

$$Q^2 = 2E^2 \frac{(1 - \cos \theta_{Lab})}{1 + \frac{E}{m_p} (1 - \cos \theta_{Lab})} \quad (4.1)$$

where E is the energy of the incoming electron right before the interaction, m_p is the mass of the proton, and θ_{Lab} is the scattering angle in the lab. Using the HDCs the electron trajectory can be projected back to the target, which provides θ_{Lab} and the interaction vertex.

While θ_{Lab} can be determined by the HDCs alone, additional information is required to determine if the electron was elastically scattered. The momentum of the scattered electron is used to isolate the elastically scattered electrons from electrons scattered through other processes. The VDCs are used to isolate elastic electrons due to their placement after QTOR and right before the main detector bars. Therefore using both the HDCs and the VDCs together allows θ_{Lab} for the elastically scattered electrons to be found.

The scattering angle that is determined by the projection from the HDCs to the target isn't necessarily the scattering angle at the interaction; rather, it is the scattering angle we can see, θ_{visible} . After the electron scatters off the proton, it travels through the target and from the target to the HDCs, where it can scatter or interact with other matter. When the HDCs project the electron back to the target to measure the scattering angle the projection doesn't necessarily match the actual interaction point, so the observed scattering angle, θ_{visible} , therefore is not θ_{physical} of the interaction.

Similarly the energy at the interaction point is estimated from the incoming beam energy and an average expected loss due to traveling in the target used in Eq. 4.1.

What is needed for the Q_{weak} experiment is the Q^2 at the interaction point, or Q_{physical}^2 . However what is measured directly from the HDCs and VDCs is a visible Q^2 , Q_{visible}^2 these are not the same as seen in Eq. 4.2.

$$Q_{\text{visible}}^2 = 2E_{\text{est}}^2 \frac{(1 - \cos \theta_{\text{visible}})}{1 + \frac{E_{\text{est}}}{m_p} (1 - \cos \theta_{\text{visible}})} \neq Q_{\text{physical}}^2 \quad (4.2)$$

The only way to get to the physical values, θ_{physical} and Q_{physical}^2 is through comparison of data and the GEANT4 simulation of the Q_{weak} experiment. By comparing the values in Eq. 4.2 to the equivalent variable in the GEANT4 simulation, as seen in Eq. 4.3, the variables for the interaction point can be extracted.

$$Q_{\text{visible,G4}}^2 = 2E_{\text{G4}}^2 \frac{(1 - \cos \theta_{\text{visible,G4}})}{1 + \frac{E_{\text{G4}}}{m_p} (1 - \cos \theta_{\text{visible,G4}})} \quad (4.3)$$

Matching Q_{visible}^2 (Eq. 4.2) and $Q_{\text{visible,G4}}^2$ (Eq. 4.3) when the GEANT4 simulation is analyzed in the same way as the data, then the GEANT4 simulation will give the Q_{physical}^2 at the interaction vertex.

Direct comparison between Q_{visible}^2 and $Q_{\text{visible,G4}}^2$ is not included here. Anna Lee is working on the ‘‘pointing’’ of the HDCs and her work will be included in her dissertation.

4.3 Kinematics Validations Using Tracking Data

Tracking data were also used to test various parts of the Q_{weak} apparatus, to see how they differ from the ideal design and see the effects these differences have on the overall experiment. By using the Q_{weak} simulation and changing an aspect of the experimental setup in the simulation the effect of that change can also be seen, and in some cases compared to tracking data. As mentioned at the beginning of this chapter we don’t

expect the data and simulation to have agreement in the average Q^2 value, however the sensitivities should be in agreement.

4.3.1 Target Properties

The Q_{weak} target has a few different properties that can affect Q^2 . It's length and location influence the scattering angle of the electrons that reach the MDs. Also, any boiling in the target and variation in the energy loss in the target can affect the energy of the electron both before and after the scattering vertex, and thus affect Q^2 .

4.3.1.1 Target Location

The target location is an important component to determine the angle with which an electron scatters from the target. The target's cold motion, *i.e.* the change in position due to the cooling of the target adds an uncertainty to the position of the target. Taking into account the cold motion of the target there is a 0.2 cm uncertainty on the location of the target [38], as determined by the JLab survey group.

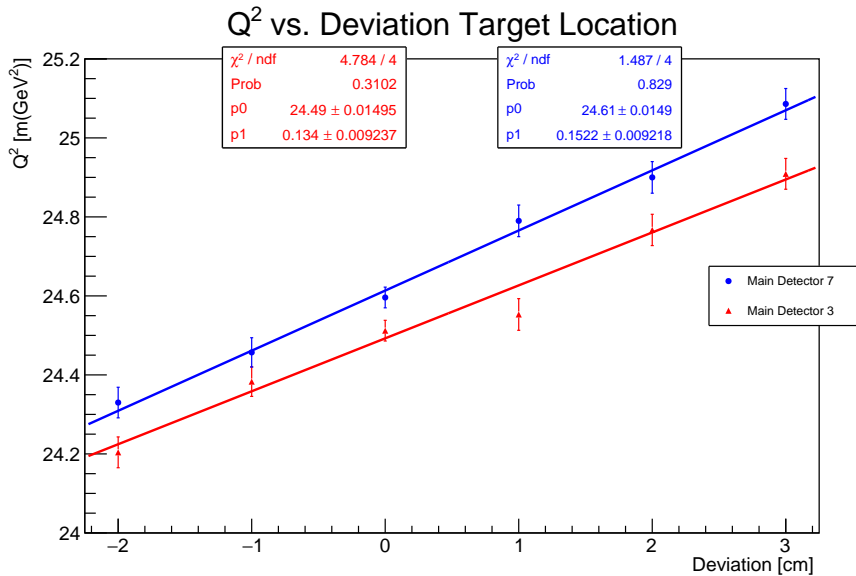


Figure 4.1: Q^2 vs. changes in location of the target along the beam in MDs 3 (blue circles) and MD 7 (red triangles) [39] as determined from the simulation¹. Here and in following figure the uncertainties on each data point are the statistical error on the means of each Q^2 distribution.

In principle the effect of the target location on the scattering angle can be calculated by simple geometry, however this is exactly true only in the case of a point target. Therefore for the long LH₂ target the effect on the uncertainty on Q^2 from uncertainty in the target location can best be investigated through the use of the simulation. Through changing the location on the target around the nominal in the simulation the target position's effect on Q^2 can be found, as seen in Fig. 4.1. The average of the two simulated dependencies was used to determine the sensitivity of Q^2 to the target position, dQ^2/dz_{Target} , yielding $0.143 \text{ m}(\text{GeV}^2) \text{ cm}^{-1}$. The 0.2 cm uncertainty on the target position correlates to a $0.029 \text{ m}(\text{GeV}^2)$ or 0.117% uncertainty on Q^2 .

4.3.1.2 Target Boiling

As the electrons travel through the target they deposit energy into the target through various scattering processes, which can cause a change in density in the target *i.e.* boiling of the LH₂ of the target. During the integrating mode of the Q_{weak} experiment, with the beam current of $180 \mu\text{A}$, the density reduction due to the target boiling was $0.8 \pm 0.2\%$ [40, 41].

Boiling in the target will cause a decrease in the density of the target, therefore an increase in the prescattering electron energy as it travels through less LH₂ than if there is no boiling. Boiling could happen throughout the whole length of the target *i.e.* “bulk boiling”. However, target boiling could alternatively take place primarily at one or both of the windows on the target, causing “film boiling”, where a pocket (or film) is created where the LH₂ is not the same density as the rest of the target. This has a different impact on Q^2 , as the location of the interaction in the target changes Q^2 . The interactions at the upstream end of the target have a lower Q^2 than those at the downstream end of the target, as seen in Fig. 4.2.

By excluding interactions that take place within a certain distance of either end of the target in the simulation, we can estimate the effect of film boiling on

¹For this plot and other plots like this “Prob” is the probability, the variables of the fit are defined through the general linear equation: $y = p_0 + p_1 \times x$.

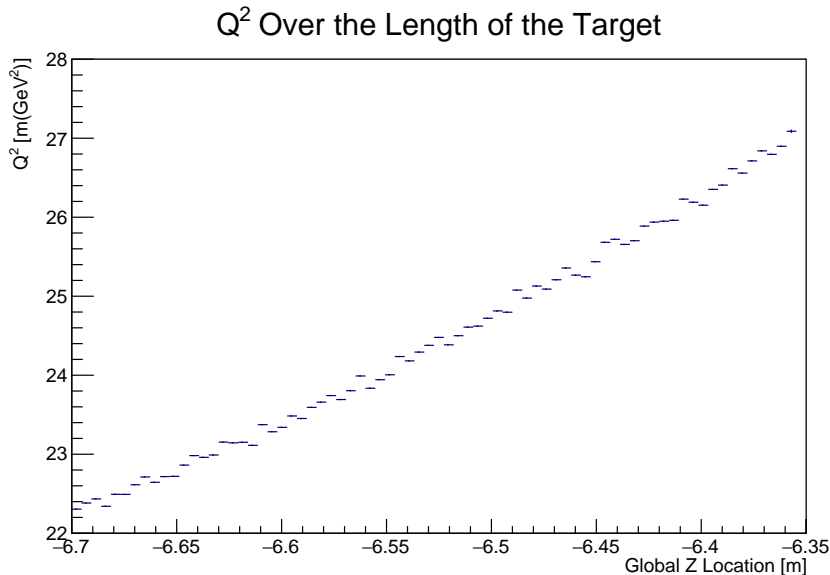


Figure 4.2: Simulated Q^2 over the LH₂ target length. Interactions at the upstream end of the target have a lower Q^2 (smaller scattering angle) than those at the downstream end of the target.

Q^2 . Conservatively it was chosen a distance of 1% (3.44 mm) of the target length, corresponding to $0.8 \pm 0.2\%$ density loss. Cutting out the 3.44 mm from the upstream end of the target shifts Q^2 by $+0.09\%$ and for the downstream end of the target a shift in Q^2 of -0.10% was found. Therefore target boiling leads to a $\pm 0.1\%$ uncertainty on Q^2 . In comparison bulk boiling would have an order of magnitude smaller effect on Q^2 .

4.3.2 Beam Properties

Various properties of the electron beam during the Q_{weak} experiment were important to look at. These include the position and angle at which the beam came into the target and the size to which the beam was rastered on the target. These properties can vary over time, especially between long down periods, and how these changes effect the experiment, mainly the Q^2 , needed to be investigated and understood.

The JLab accelerator and the Q_{weak} experiment have different coordinate systems and for most of the tracking analysis this is irrelevant. However, in the beam position and angle studies this matters, because the beam was deliberately moved in the \hat{x} and

\hat{y} directions. The JLab accelerator coordinate system has the beam moving in the $-\hat{z}$ direction while the Q_{weak} experiment² coordinate system has the beam moving in the $+\hat{z}$ direction. Therefore the Q_{weak} experiment coordinate system has a parity transformation for the \hat{x} and \hat{z} directions from the JLab accelerator coordinate system as illustrated in Fig. 4.3. All of the analysis related to the beam position and angle results will be shown using the JLab accelerator coordinate system.

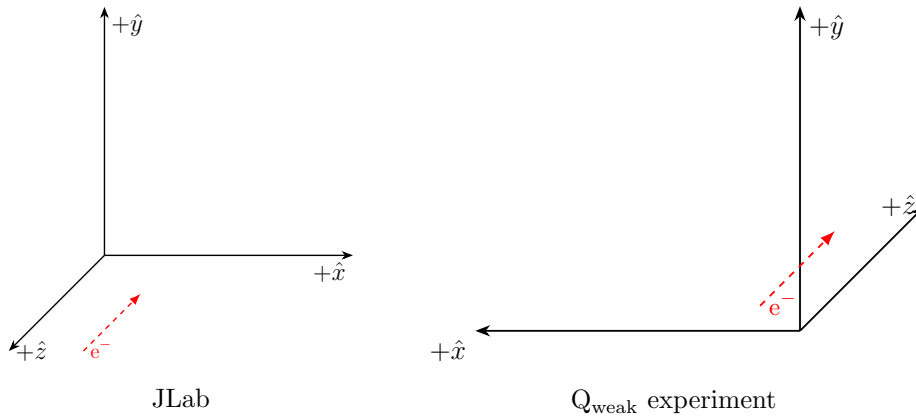


Figure 4.3: The JLab accelerator and Q_{weak} experiment's coordinate systems. The beam direction is illustrated in red, it travels in the $-\hat{z}$ in the accelerator coordinate system and the $+\hat{z}$ in the Q_{weak} experiment coordinate system.

4.3.2.1 Raster Size

As stated in Sec. 3.3.1, the beam was rastered uniformly over a $4\text{ mm} \times 4\text{ mm}$ area. During tracking runs the raster could be varied without damaging the target because of the lower beam current, therefore during this time the effect of the raster on Q^2 can be investigated. Rastering the beam over a uniform area by modest amounts is not expected to change Q^2 . For a sequence of tracking runs the raster was varied from $1\text{ mm} \times 1\text{ mm}$ to $5\text{ mm} \times 5\text{ mm}$ in sequential steps of 1 mm in each direction. The extracted Q^2 for these runs is shown in Fig. 4.4.

There is no evidence of a change in Q^2 due to change in the raster size, $dQ^2/d(\text{Raster Size})$ is $0.005 \pm 0.008\text{ m}(\text{GeV}^2)\text{ mm}^{-2}$ and $0.001 \pm 0.008\text{ m}(\text{GeV}^2)\text{ mm}^{-2}$ for MDs 1 and 5 respectively. Assuming a maximum possible raster difference of $\pm 1\text{ mm}$

²This is also the coordinate system used in the GEANT4 simulation.

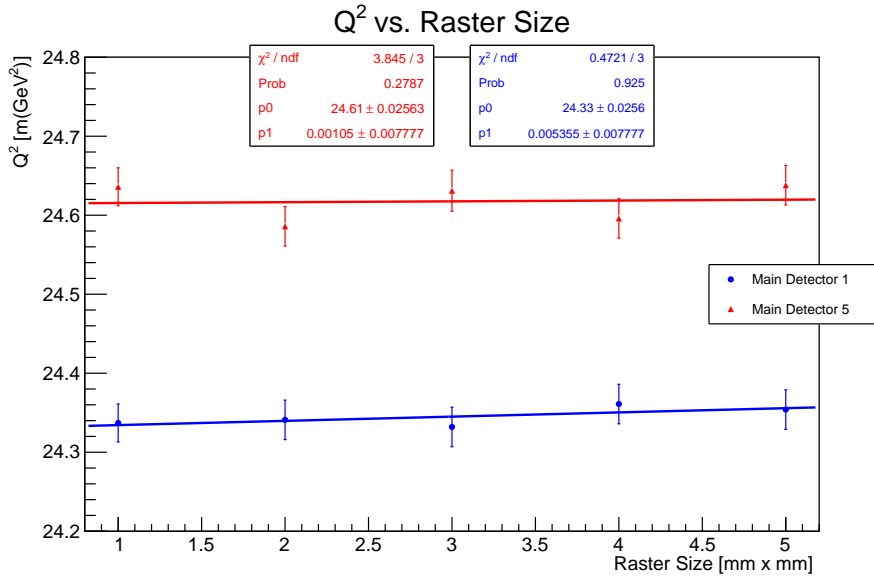


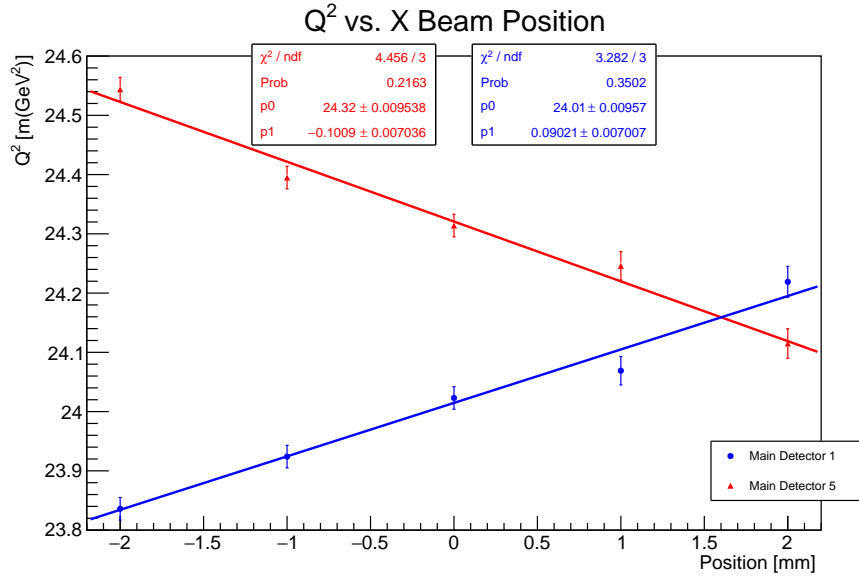
Figure 4.4: The effect of changing the raster size on Q^2 in MDs 1 (blue circles) and MD 5 (red triangles) from tracking data.

between tracking and parity mode and a maximum change in Q^2 due to the raster of the maximum slope with one sigma, the uncertainty on Q^2 is 0.054% due to the raster size. The simulation results confirm this result.

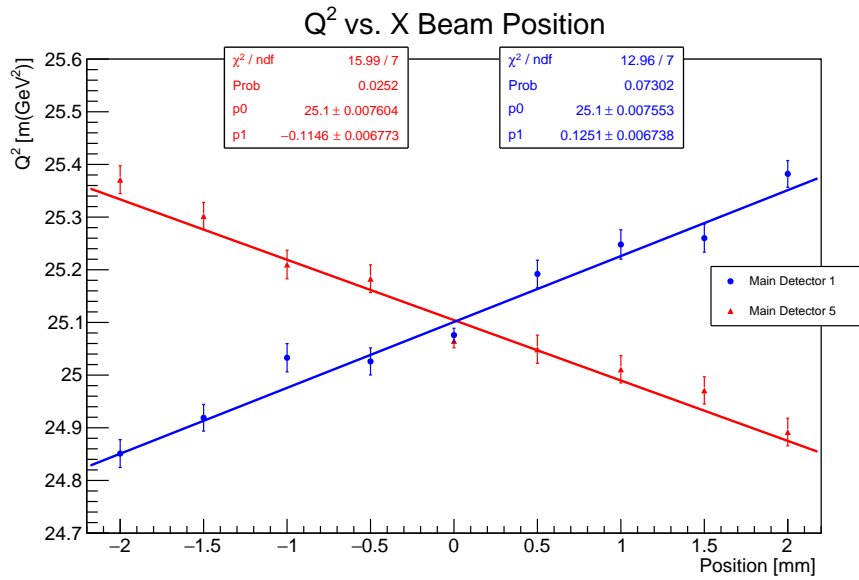
4.3.2.2 Beam Position

The position at which the beam impinges on the target can affect the Q^2 values in individual MDs. If the beam is closer to one MD the scattering angle (θ) and Q^2 for that MD will decrease and therefore both will increase in the opposite MD. Due to the symmetric layout of the detectors in the Q_{weak} experiment, this increase and decrease in individual bars should, to first order, cancel between opposite pairs. However symmetry-breaking imperfections in the actual apparatus will spoil this cancellation.

During the tracking mode there were dedicated runs where the position of the center of the beam on the target was changed. These changes were from -2 mm to 2 mm from the nominal beam position in steps of 1 mm in both the \hat{x} and \hat{y} direction independently. Moving the beam only took place in the \hat{x} and \hat{y} direction and not along the diagonal (45° to the \hat{x} and \hat{y} directions) due to time constraints. For the GEANT4



Data



GEANT4

Figure 4.5: \hat{x} Beam Position Scans for MDs 1 (blue circles) and 5 (red triangles) from tracking data (top) and from GEANT4 (bottom).

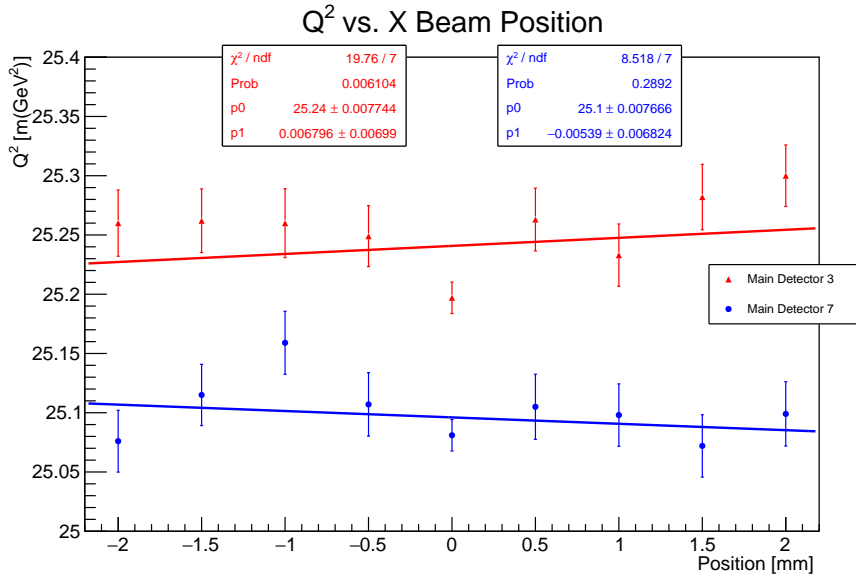


Figure 4.6: \hat{x} Beam Position Scans for MDs 3 and 7 from GEANT4.

simulation the beam was moved in the same way as was done in the experiment with the same MDs.

As expected, when the beam position is varied along the axis joining two opposite detectors (*e.g.* along the \hat{x} for MD 1 and MD 5, or along the \hat{y} axis for MD 3 and MD 7, see Fig. 3.6), the Q^2 in one MD increases and that in the other MD decreases. This can be seen in both the data and simulation in Figs. 4.5 and 4.7. The simulation and data agree, as expected.

When the beam moves in one direction and Q^2 is measured in the MDs that are perpendicular to the beam motion (*i.e.* moving the beam in the \hat{y} direction and measuring Q^2 in MDs 1 and 5), it would be expected that Q^2 wouldn't change. The measured Q^2 for both simulation and data in this case is seen in Figs. 4.6 and 4.8, and is consistent with a slope of zero, within errors, as expected.

The slopes for all of these cases are shown in Table 4.1. When moving the beam in either the \hat{x} or \hat{y} direction and measuring Q^2 in the MDs that are centered on that axis, the data and simulations agree quite well. In opposite MDs there is an increase of Q^2 in one and decrease of Q^2 in the other, which cancel out within errors.

In the MD 1 and MD 5 data taken during the \hat{y} position scan, the slope agrees with

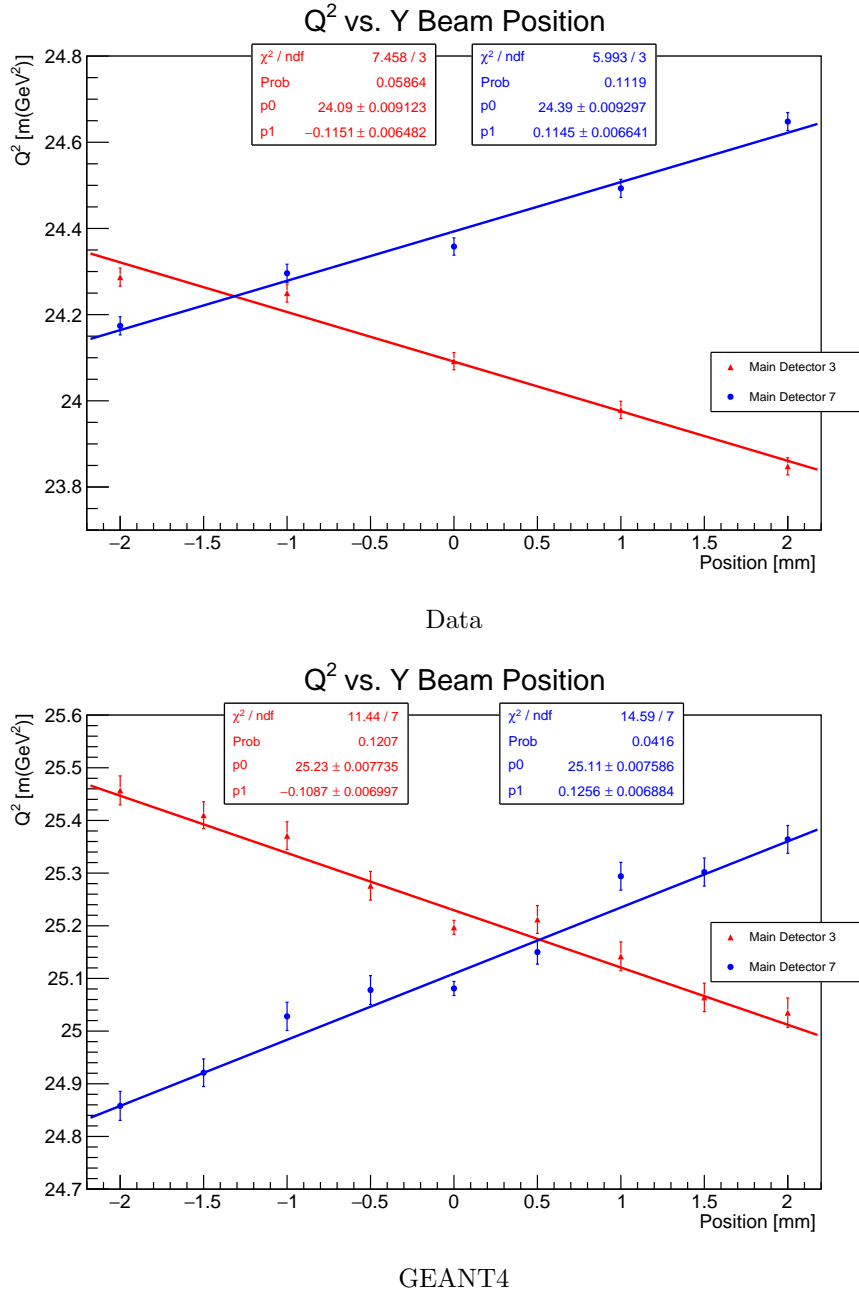


Figure 4.7: \hat{y} Beam Position Scans for MDs 3 (red triangles) and 7 (blue circles) from tracking data (top) and from GEANT4 (bottom).

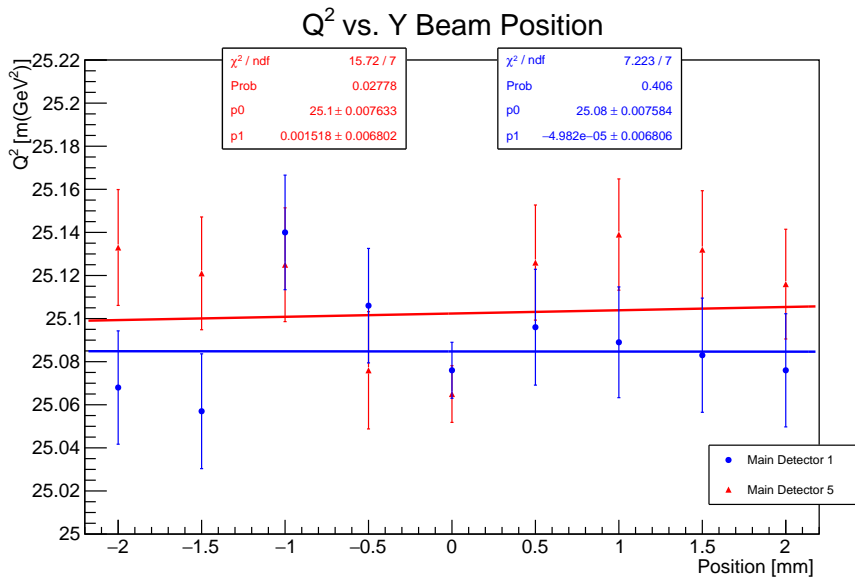
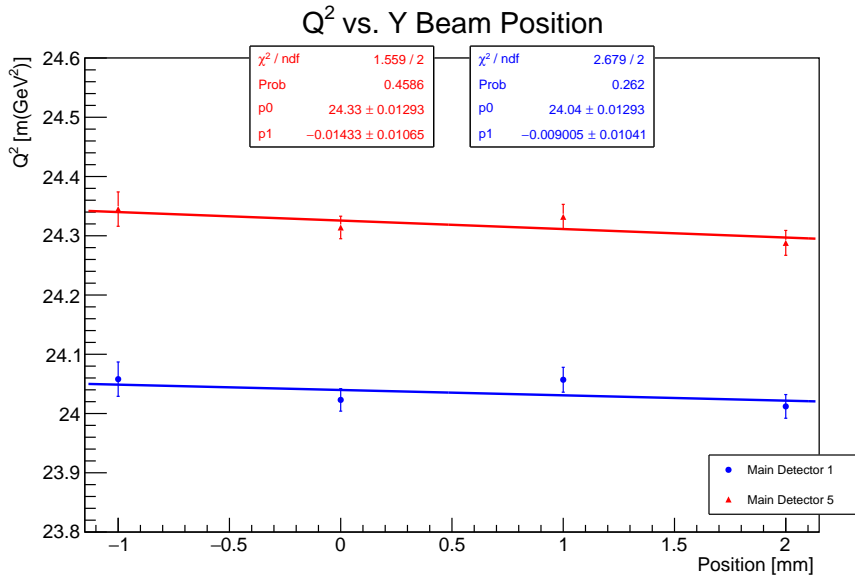


Figure 4.8: \hat{y} Beam Position Scans for MDs 1 (blue circles) and 5 (red triangles) from tracking data (top) and from GEANT4 (bottom). For discussion of the small slopes see text.

Direction	MD	$\frac{dQ^2}{d\hat{x}}$ or $\frac{dQ^2}{d\hat{y}}$ $\left(\frac{\text{m}(\text{GeV}^2)}{\text{mm}}\right)$	
		Data	GEANT4
\hat{x}	Both	-0.006 ± 0.005	0.005 ± 0.005
	1	0.090 ± 0.007	0.125 ± 0.007
	5	-0.101 ± 0.007	-0.115 ± 0.007
	Both	—	0.001 ± 0.005
	3	—	0.007 ± 0.007
	7	—	-0.005 ± 0.007
\hat{y}	Both	-0.012 ± 0.007	0.001 ± 0.005
	1	-0.009 ± 0.010	0.000 ± 0.007
	5	-0.014 ± 0.010	0.002 ± 0.007
	Both	-0.007 ± 0.005	0.085 ± 0.005
	3	-0.115 ± 0.006	-0.109 ± 0.007
	7	0.115 ± 0.006	0.126 ± 0.007

Table 4.1: Comparison of the slopes of the fits from the beam position scans for tracking data and simulation. “Both” refers to the Q^2 average between the two opposite MDs.

zero within 2σ , however the possible deviation from a zero slope could be due to the beam not staying constant in \hat{x} during this scan. Assuming that is true, a shift of only $139 \mu\text{m}$ in \hat{x} would explain this. A shift of this magnitude would not be unreasonable, as it is smaller than the intrinsic (or “unrastered”) beam profile, $\approx 200 \mu\text{m}$ [28].

Taking the maximum average slope between two opposite MDs with a 1σ uncertainty, $(0.012 \text{ m}(\text{GeV}^2) \text{ mm}^{-1})$ and $0.011 \text{ m}(\text{GeV}^2) \text{ mm}^{-1}$ for \hat{x} and \hat{y} beam position respectively) the average of opposite MDs of slopes and the uncertainty on the beam position from the neutral axis the uncertainty on Q^2 due to the beam position can be found. Based on optical surveys of the BPMs pre- and post-experiment, it was found that the BPMs were not measured to be reproducible to better than 1.5 mm, which is taken to be the uncertainty on the absolute beam position [42–44].

Since beam motion in the \hat{x} direction is independent of the movement in the \hat{y} direction, the total uncertainty on Q^2 due to the beam position is the quadrature sum of the uncertainty measuring Q^2 in MDs along or perpendicular to the axis of the beam motion. This, coupled with the 1.5 mm uncertainty on the beam position, leads to a 0.14% uncertainty on Q^2 .

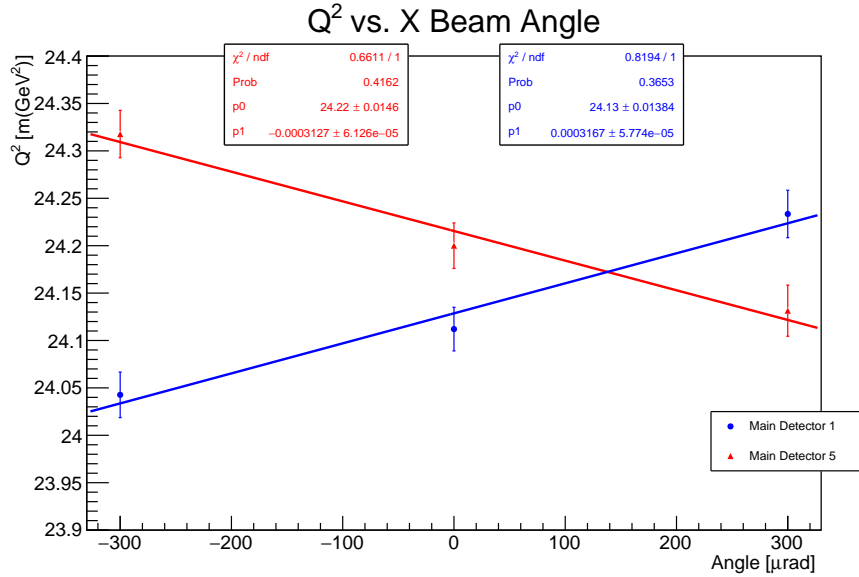
4.3.2.3 Beam Angle

As with the beam position, the angle with which the beam arrives at the target was also varied during dedicated tracking runs. The \hat{x} beam angle was varied from $-300 \mu\text{rad}$ to $300 \mu\text{rad}$ in steps of $300 \mu\text{rad}$ in the data. In the simulation, in both \hat{x} and \hat{y} , the beam angle was varied from $-600 \mu\text{rad}$ to $600 \mu\text{rad}$. As stated before, and as with the other direct comparisons between data and simulation, absolute Q^2 values may not be in agreement. Like with the beam position, the data and simulation were compared, the dependencies of Q^2 on beam angle are found to be similar as seen in Figs. 4.9, 4.10, 4.11 and 4.12.

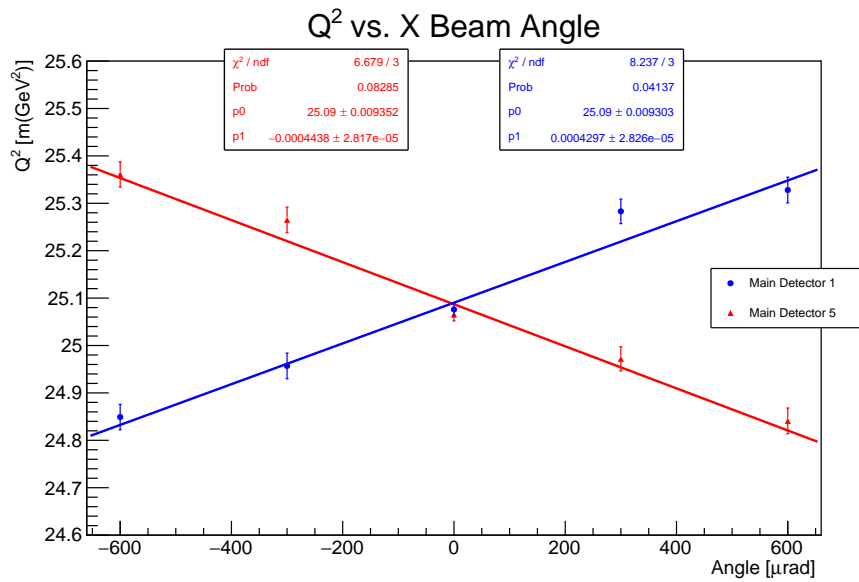
All of the slopes are summarized in Table 4.2 and cancel between opposite MDs. Therefore the beam angle does not have a significant impact on Q^2 and is therefore not a contributing uncertainty on Q^2 ($\ll 0.1\%$).

Direction	MD	$\frac{dQ^2}{d\theta_{\hat{x}}}$ or $\frac{dQ^2}{d\theta_{\hat{y}}}$ $\left(\frac{\text{m}(\text{GeV}^2)}{\mu\text{rad}}\right)$ in units of 10^{-5}			
		Data		GEANT4	
\hat{x}	Both	0.20 \pm	4.21	0.70 \pm	2.0
	1	31.7 \pm	5.77	44.4 \pm	2.82
	5	-31.3 \pm	6.13	-43.0 \pm	2.83
	Both	—	—	1.12 \pm	1.98
	3	—	—	0.199 \pm	2.80
	7	—	—	2.04 \pm	2.86
\hat{y}	Both	—	—	3.69 \pm	1.99
	1	—	—	4.56 \pm	2.76
	5	—	—	2.81 \pm	2.84
	Both	—	—	0.55 \pm	2.02
	3	—	—	-42.7 \pm	2.85
	7	29.2 \pm	2.44	43.8 \pm	2.86

Table 4.2: Comparison of the slopes of the fits from the beam angle scans for data and simulation. “Both” refers to the Q^2 average between the two opposite MDs.



Data



GEANT4

Figure 4.9: \hat{x} Beam Angle Scans for MDs 1 (blue circles) and 5 (red triangles) with tracking data (top) and from GEANT4 (bottom).

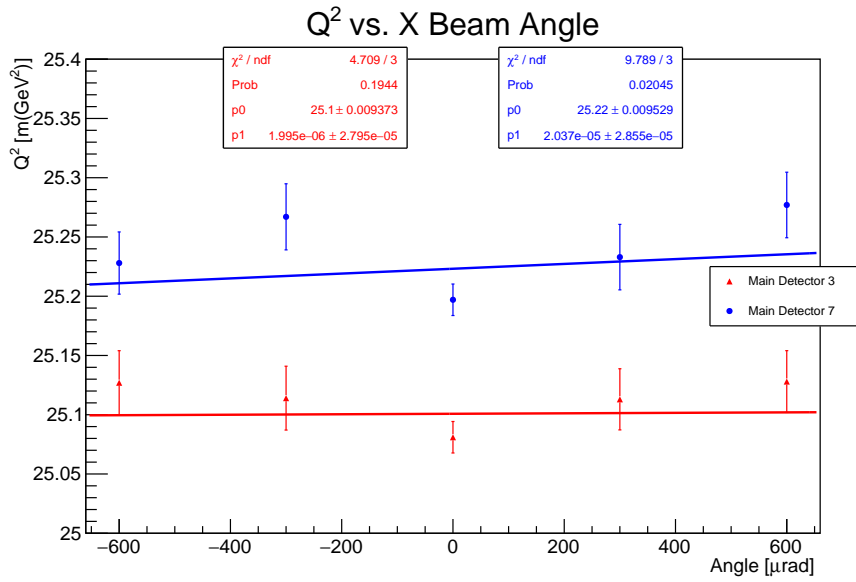


Figure 4.10: \hat{x} Beam Angle Scans for MDs 3 (red triangles) and 7 (blue circles) from GEANT4.

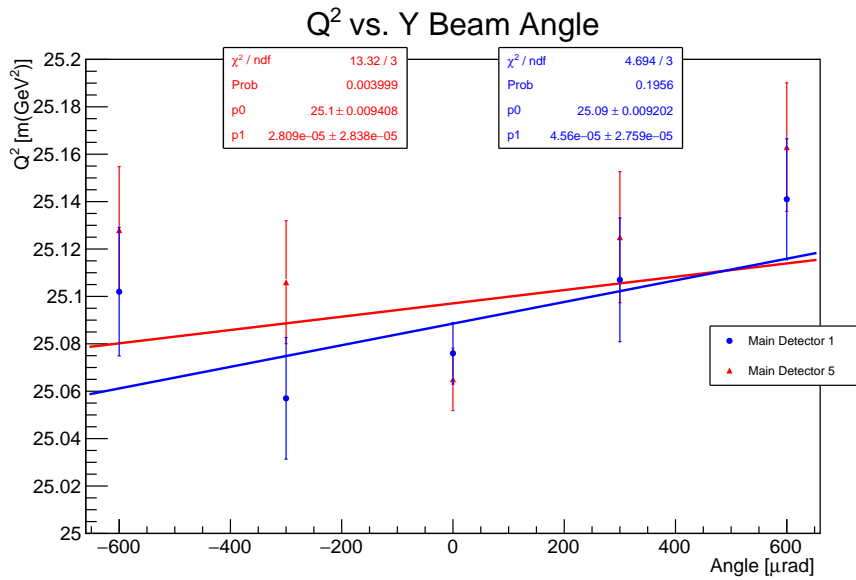


Figure 4.11: \hat{y} Beam Angle Scans for MDs 1 (blue circles) and 5 (red triangles) from GEANT4.

4.3.2.4 Beam Energy

During the Q_{weak} experiment the beam energy was measured. The uncertainty on this measurement contributes to the uncertainty on Q^2 , because of the relationship

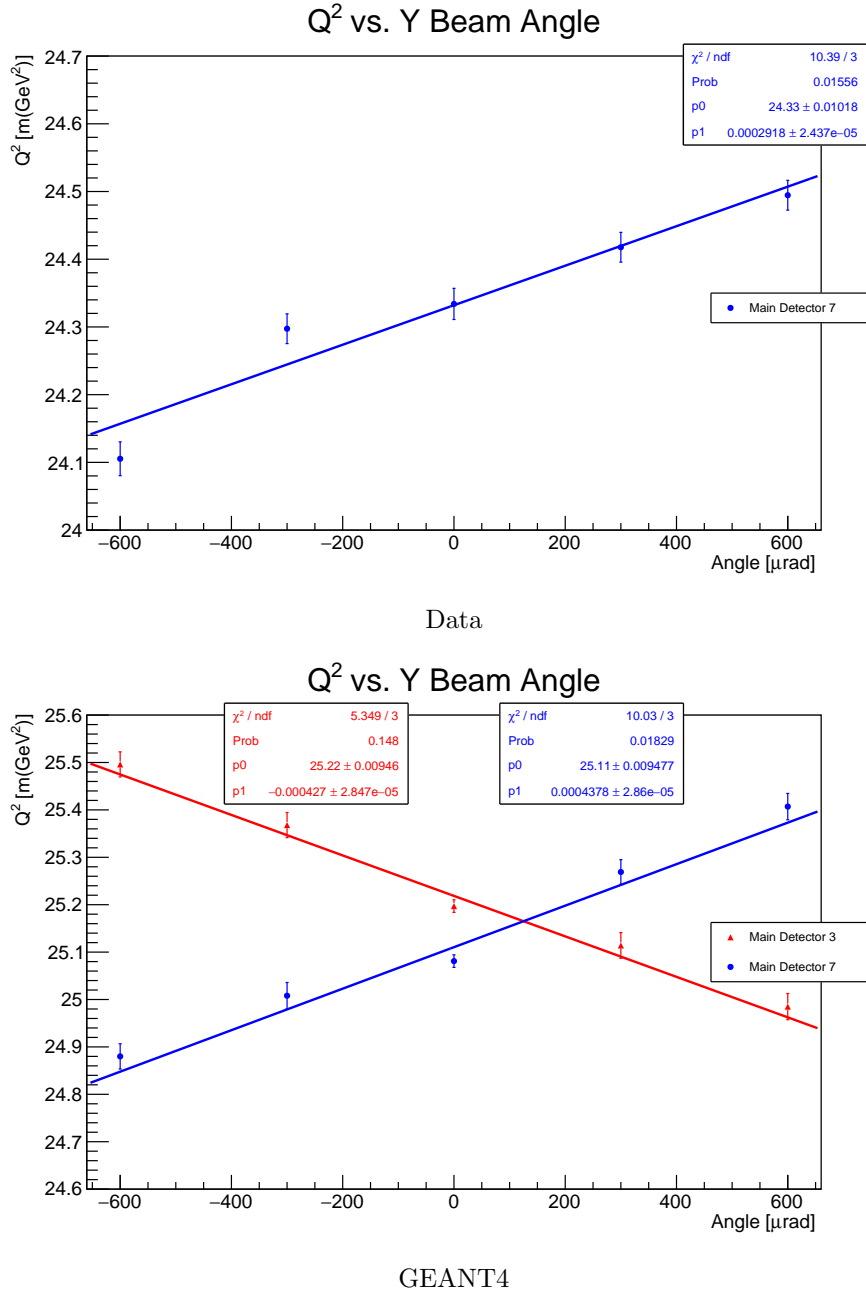


Figure 4.12: \hat{y} Beam Angle Scans for MDs 3 (red triangles) and 7 (blue circles) with tracking data (top) and from GEANT4 (bottom).

between E_B and Q^2 . At various points in the tracking periods this was measured invasively through the use of three position sensitive 3-wire scanners placed in the Hall C arc [28]. Figure 4.13 shows the relative beam energy³ during part of the experiment, showing that beam energy was very stable throughout Q_{weak} . The beam energy was measured to be 1158.4 ± 1.1 MeV for Run 2 (see Sec. 4.4.1), which correlates to a 0.19% uncertainty on Q^2 .

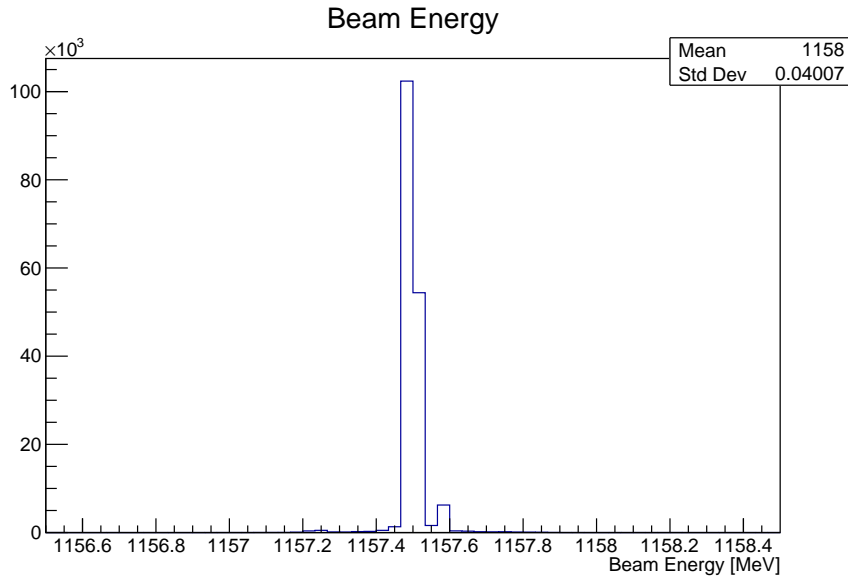


Figure 4.13: Stability of the beam energy during part of the Q_{weak} experiment.

4.3.3 QTor Magnet Properties

As stated earlier, the QTor magnet focuses the electrons on the MD bars, therefore it is important to investigate aspects of QTor’s magnetic field. How well the QTor current (which determines the overall strength of the field) is known will contribute to an uncertainty on Q^2 . This was investigated both through a specific study taken during a tracking period in the Q_{weak} experiment and with the simulation.

As mentioned in Chap. 3, the Q_{weak} apparatus was built to be symmetric, this assumes that the magnetic field is identical (in r , θ , and ϕ) in each of the 8 octants. The reality however is that QTor’s field varies from octant to octant, this variation’s

³The relative beam energy, measured non-invasively, is known at JLab as the “Tiefenbach” energy.

effect on Q^2 can only be investigated with the simulation.

4.3.3.1 Magnetic Field Strength Scan

During the experiment the current at which QTor ran was chosen such that the elastically scattered electrons would be focused onto the main detector bars. By changing this current to different values, different sets of electron tracks can be focused on the detectors, thereby changing the Q^2 of the detected tracks. An extraction of the average Q^2 from elastic scattering for all eight of the MDs in the simulation for a range of QTor currents from 8000 A to 9000 A is shown in Fig. 4.14.

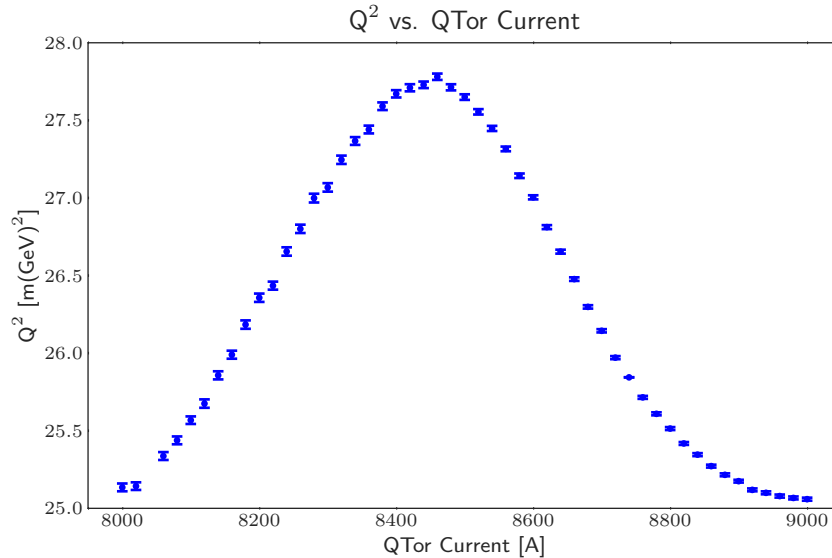


Figure 4.14: Q^2 for elastic scattered electrons vs. QTor current from 8000 A to 9000 A averaged over all eight MDs, from the simulation. The Q_{weak} experiment used a current of 8900 A.

During the Q_{weak} experiment a similar scan of QTor current was performed, from 8800 A to 9100 A, which is shown in Fig. 4.15. The data are fitted with a quadratic dependence to help guide the eye. Comparing this to Fig. 4.14, we see a similar dependence over this small range in QTor current.

Looking at a smaller range in QTor current near the set current of around 8900 A used in the Q_{weak} experiment, we can use a linear fit. This is done for a current

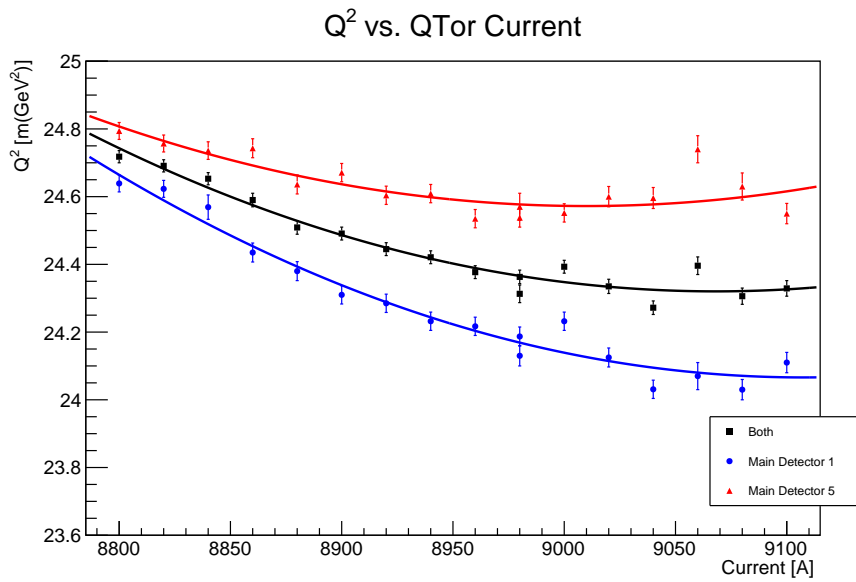


Figure 4.15: Q^2 vs. QTor current in the tracking data over the QTor scan for currents from 8800 A to 9100 A. In MD 1 (blue circles), MD 5 (red triangles), and the average of the two MDs (black squares). All of these have a quadratic fit to help guide the eye.

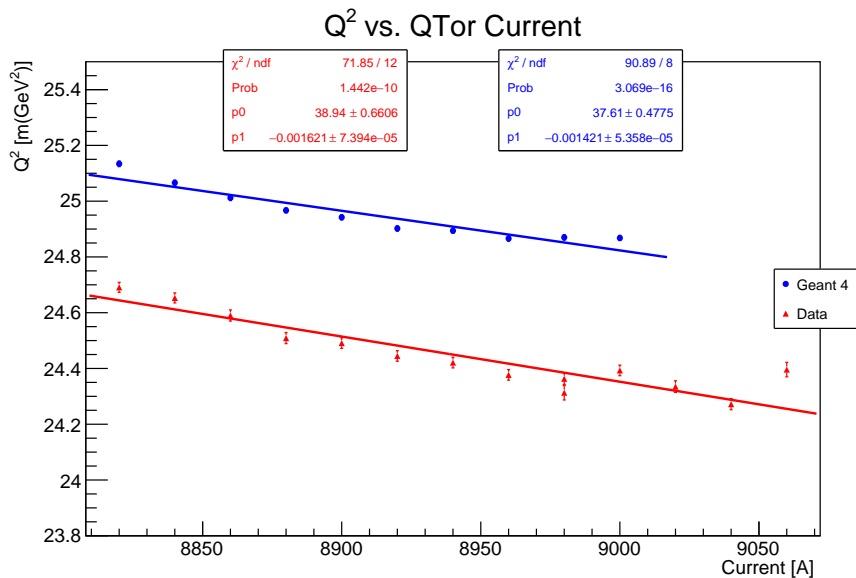


Figure 4.16: Q^2 vs. QTor current for tracking data (red triangles: average of MD 1 and 5) and GEANT4 (blue circles). The error bars on the simulation are included but are less than or equal to the size of the plotting symbols.

range of 8820 A to 9060 A in the data and 8820 A to 9000 A in simulation, as shown in Fig. 4.16. As explained in the beginning of this chapter, the discrepancy in the

absolute values between the data and simulation is likely due to the inability to achieve agreement between the visible scattering angle in data and simulation. The fit for the data leads to a slope of $-1.62 \pm 0.07 \times 10^{-3} \text{ m}(\text{GeV}^2) \text{ A}^{-1}$ and a very similar value of $-1.42 \pm 0.05 \times 10^{-3} \text{ m}(\text{GeV}^2) \text{ A}^{-1}$ for the simulation. There was a $\pm 10 \text{ A}$ uncertainty on the absolute calibration of the QTor current; along with the slope from the fit to the data, this leads to a 0.066% uncertainty on Q^2 [45].

4.3.3.2 Magnetic Field Sector Rotation Study

As described in Sec. 3.3.4, the MDs were set up to use symmetry as a way to help reduce false asymmetries. However, QTor’s field, as actually constructed and mapped via a 3-axis mapper, is not perfectly symmetric [46]. The imperfect symmetry of the magnetic field can lead to an MD dependent variation in Q^2 . However, imperfections in the locations of the MDs or in the primary collimator can also lead to variations in Q^2 in a given MD. To isolate the effect due to the magnetic field we need to use the simulation, since the physical magnet cannot be rotated in the apparatus. By rotating the QTor’s magnetic field map [28] included in the Q_{weak} simulation the full effect that the magnetic field has in each MD can be seen.

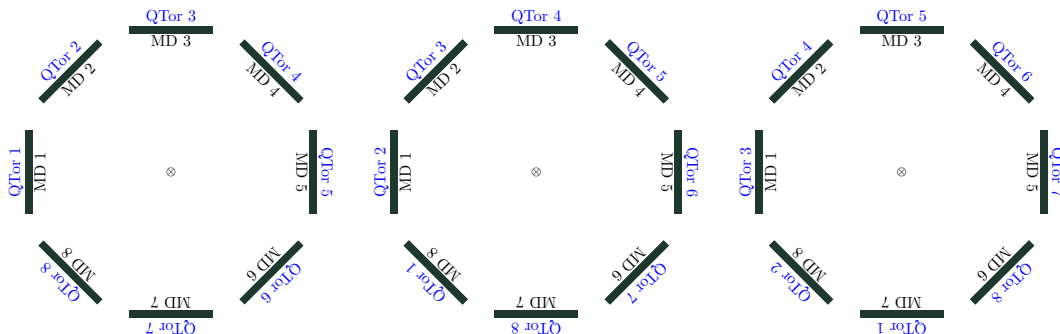


Figure 4.17: Rotation of each octant of QTor’s magnetic field, relative to the MD. The MD number is written inside the MD in black and the QTor octant is written in blue outside the MD. From left to right, rotations of QTor of 0.0° , -45.0° , and -90.0° .

Three simulations were run, each with the QTor field rotated by a different angle around the beam axis, 0.0° , -45.0° , and -90.0° ; the scheme of these rotations are illustrated from left to right in Fig. 4.17. When rotating QTor section or octant

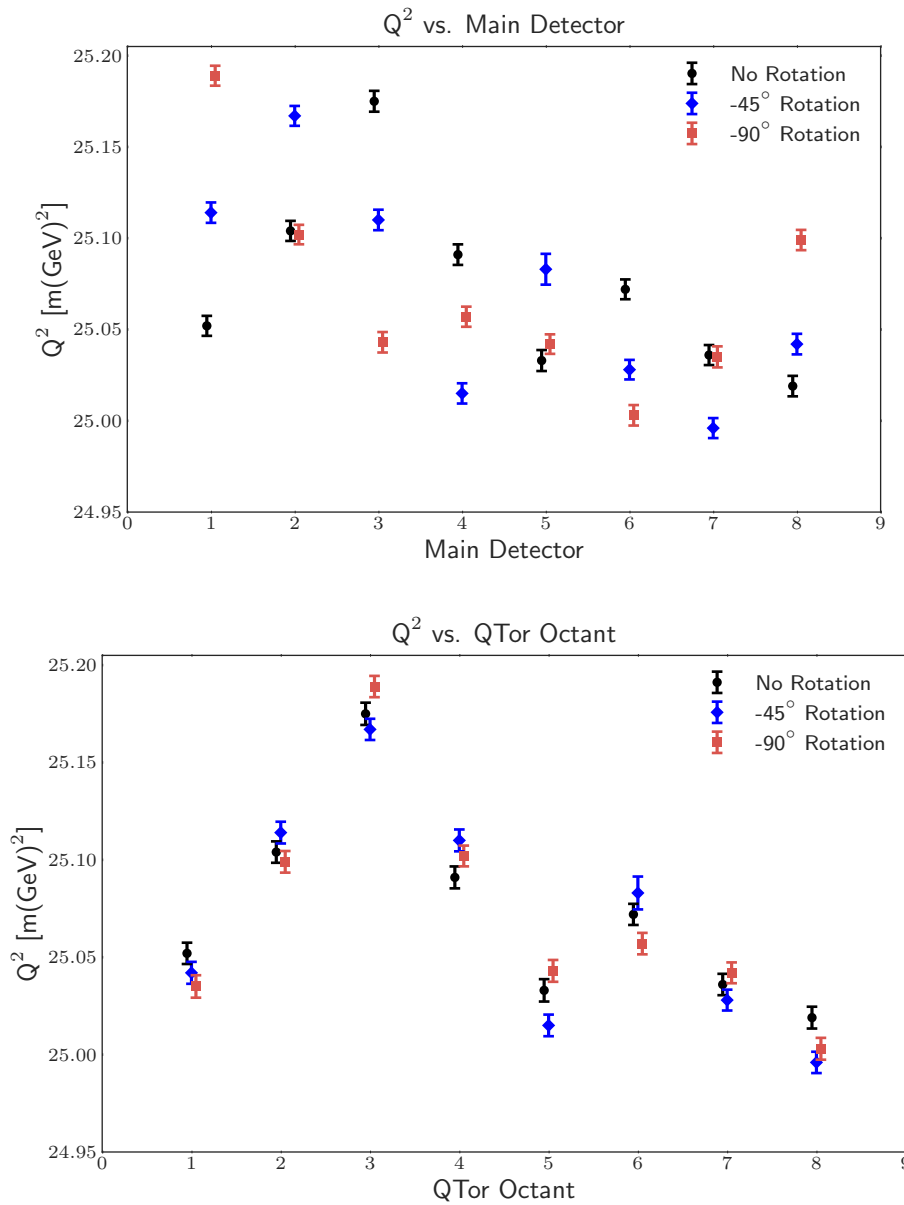


Figure 4.18: Simulated results. On the top, the Q^2 for each section in QTor is plotted vs. MD number. On the bottom the Q^2 for each octant in QTor is plotted vs. QTor octant. In both figures, the black circles correspond to where there is no rotation in the magnetic field. The blue diamonds correspond to where there is a -45° rotation in the magnetic field. The red squares correspond to where there is a -90° rotation in the magnetic field. These are illustrated from left to right in Fig. 4.17.

into various MDs placed in their survey locations, Q^2 will change in each of these MDs, to that of the counterclockwise adjacent MD for each step of -45° that is taken. Each octant of QTor, regardless of what MD it is rotated into, should result in a consistent value of Q^2 for that octant of QTor, with any variations only being due to the differences in the MDs. This is consistent with what is found through use of the simulation as seen in Fig. 4.18; the variation in the bottom figure is due to the small variation between the MD locations. There is a spread in Q^2 over all the MDs of $0.156 \text{ m}(\text{GeV}^2)$ with an RMS of $0.051 \text{ m}(\text{GeV}^2)$. Rather than assuming that the field map is 100% accurate, the conservative assumption is made that the MD to MD variation in the field map is about the same as the variation that the real field has. By assuming that this amount of variation (RMS) is realistic and randomly distributed the average effect of this is $\text{RMS}/\sqrt{8}$, giving an $0.018 \text{ m}(\text{GeV}^2)$ or 0.072% uncertainty on Q^2 .

4.3.4 Main Detector and Primary Collimator

The location of both the MDs and the primary collimator and it's holes, and any imperfections in those holes can affect Q^2 . The effects on Q^2 from these are only able to be studied through the simulation.

The standard GEANT4 simulation has the locations of the MDs and primary collimators as determined from survey. These locations were varied to study the sensitivity of Q^2 to the collimator and MDs positions. Changes in both of these will cause changes in the distribution of scattered electrons on the MDs. The primary collimator defines the acceptance, therefore any changes in these holes will impact the acceptance, specifically the scattering angle which has a direct relationship with Q^2 .

4.3.4.1 Position of Main Detectors

The positions of the MDs didn't end up being their ideal positions in the actual, as-constructed apparatus due to tolerances in their support structure. The effect of this can only could be studied with the Q_{weak} simulation similar to the imperfections

of the QTor field discussed in the previous section. The ideal location of the main detectors places them at the same location along the \hat{z} -axis from the target and radial distance from the center of the MD array. The maximum difference between the ideal and the surveyed positions [47] were in MD 1 in the \hat{z} and radial direction, and were 1.215 cm and 0.446 cm with an RMS of 0.645 cm and 0.293 cm respectively.

The impact on Q^2 of changing the MD locations to their ideal location, from that which was in the experiment is illustrated in Fig. 4.19. The change in location does not have significant impact on the Q^2 seen in each MD, all agreeing within errors. Rather than rely on the survey positions and their claimed precision, the conservative choice to use the size of the difference in Q^2 between the ideal and surveyed locations as the uncertainty on Q^2 , this gives a $0.006 \text{ m}(\text{GeV}^2)$ or a 0.024% uncertainty on Q^2 .

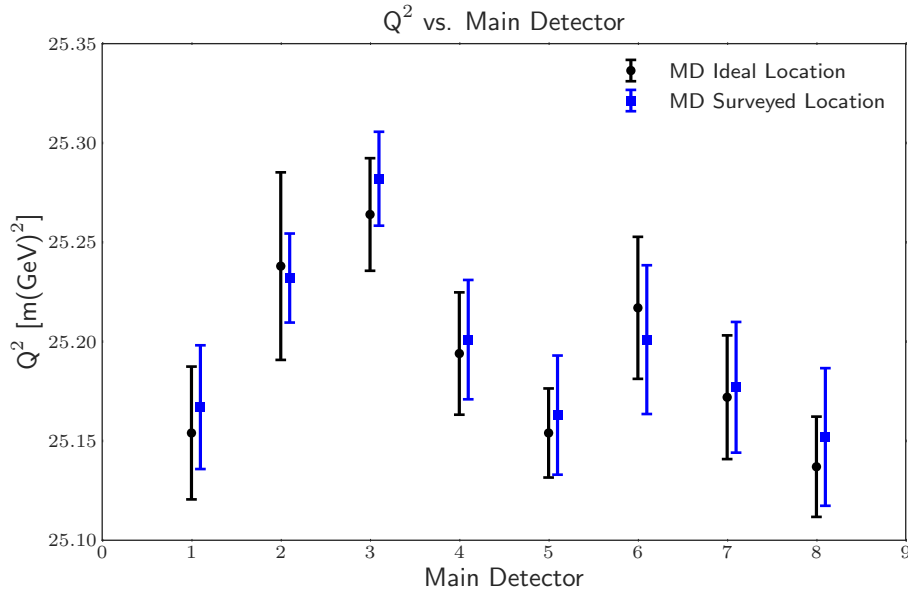


Figure 4.19: The simulated Q^2 measured in each MD, for the MDs in their ideal locations (black circles) and their surveyed positions (blue squares). The variation in Q^2 due to non-ideal locations of the MDs is seen to be very modest. The MD dependence is due to the magnetic field imperfections.

4.3.4.2 Primary Collimator Location

The primary collimator location has a simple contribution to Q^2 based on geometry, for a point-like target, and the assumption that the MDs accepts all the events that make it through the collimator,

$$\frac{dQ^2}{Q^2} = 2\frac{d\theta}{\theta} = 2\sqrt{\left(\frac{dR}{R}\right)^2 + \left(\frac{dL}{L}\right)^2} \quad (4.4)$$

where R is the effective radius of the collimation system, and L is the separation between target and primary collimator. The uncertainty in effective radius determined by survey is $dR = 0.5$ mm. The location of the primary collimator sets $L = 2.72$ m and $dL = 0.5$ mm, then $dL/L = 0.02\%$ also determined by survey [28, 48–51].

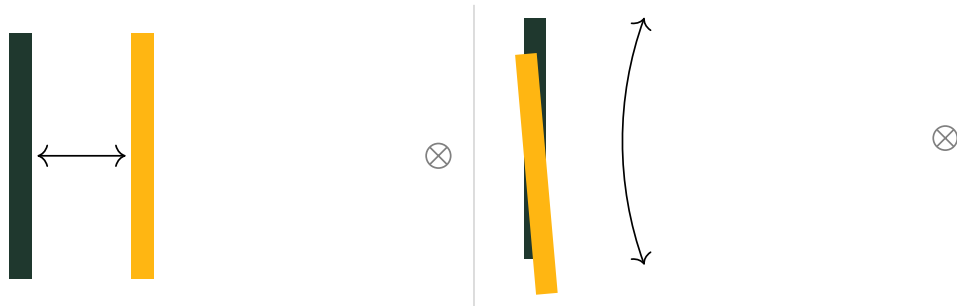


Figure 4.20: The primary collimator was shifted in the simulation around the beam line (gray circle), radially (left) and azimuthally (right). Note: the figures do not show the actual shape of the collimator aperture.

If the location of the primary collimator is slightly off from the ideal position this will effect θ and consequently Q^2 . The only way to look beyond the simple geometric estimate with a point-like target of this effect is to change the primary collimator location through the simulation. The primary collimator holes were moved in the simulation from -8 mm to 8 mm in steps of 4 mm, both radially and azimuthally, as illustrated in Fig. 4.20.

Moving the collimator holes radially should be similar to moving the beam position, so Q^2 would be expected to have a linear relationship with the radial shift of the collimator hole location. In contrast, making an azimuthal shift should have a symmetric

effect around the nominal location, which is what is seen illustrated in Fig. 4.21. The azimuthal shift is tiny and its effect is negligible compared to the radial shifts.

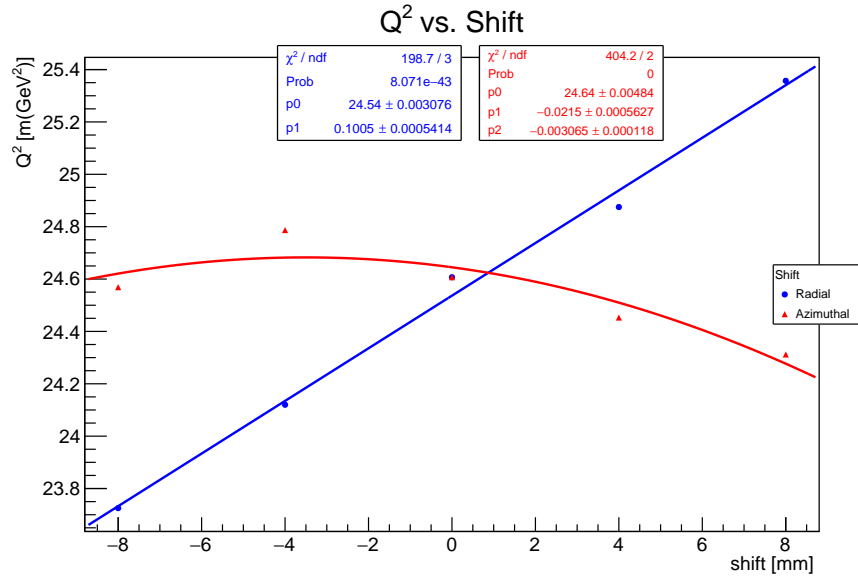


Figure 4.21: The primary collimator shifts effect on Q^2 . Blue circles are for radial shifts, and red triangles are for azimuthal shifts.⁴

Making the radial shift leads to a slope of $0.1005 \pm 0.0005 \text{ m(GeV}^2) \text{ mm}^{-1}$, assuming the survey radial shift of 0.5 mm [50, 51] the change in Q^2 from just the radial shift is $0.0503 \text{ m(GeV}^2)$ or 0.202%. Combining this with the distance between the target and the primary collimator leads to a total of 0.206% uncertainty on Q^2 from the primary collimator location.

4.3.4.3 Primary Collimator Imperfections

In the previous section the effect on Q^2 of moving the location of the primary collimator holes was examined. However, this does not look at what happens if the shape of the collimator holes are not exactly as designed. Imperfections in the collimator aperture can be investigated by studying the effect on Q^2 of cutting events on the tracking data which arise from tracks close to the edges of the holes in the primary collimator. This is different from the study in the previous section because rather than moving the

⁴For the azimuthal shift fit the variables are defined through the general quadratic equation: $y = p0 + p1 \times x + p2 \times x^2$.

whole collimator hole, this moves just one of the edges. This analysis would change the face area of the collimator hole.

Figure 4.22 shows the projection of tracks through the primary collimator for package one. Using this distribution and making cuts on it azimuthally and radially allows one to show how imperfections of the collimator holes affect Q^2 .

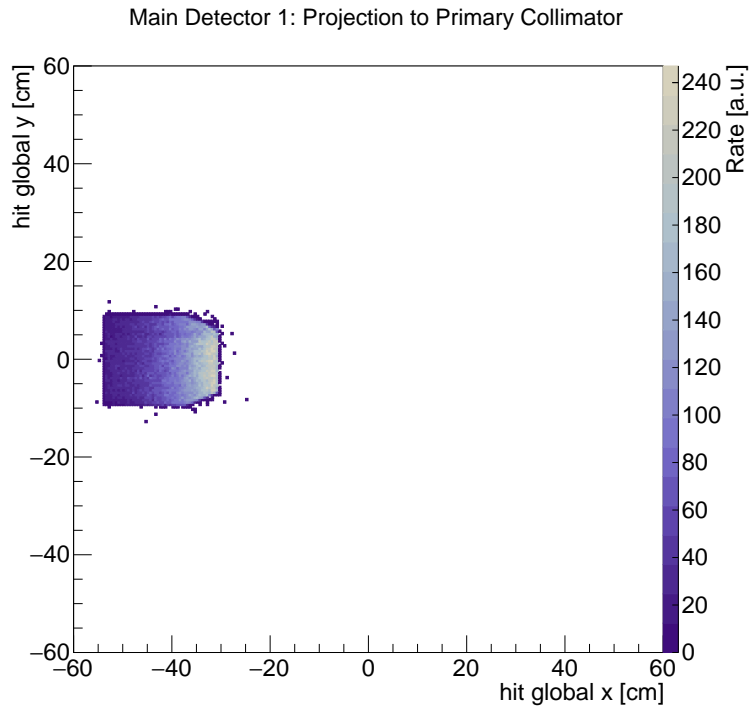


Figure 4.22: Projection from tracking data of detected electrons to the primary collimator. The shape of the collimator hole is clearly visible.

The maximum size of the collimator imperfection as determined by survey is ± 0.5 mm [50, 51]. Changing the outer radial edge changes Q^2 by 0.033% and the azimuthal edges changes Q^2 by 0.056%. Both of these are independent, therefore there is a 0.065% uncertainty on Q^2 due to collimator imperfections. As might be expected, the collimator's effect on Q^2 is dominated by the location of the inner radial edge (see Sec. 4.3.4.2). Fig 4.22 illustrates that the inner radial edge has the highest rate and therefore small changes to its location will have a larger impact than any other edge of the collimator hole.

4.3.5 Radiative Corrections

The GEANT4 simulation includes external bremsstrahlung but ignores internal bremsstrahlung in the interactions. Tracking data includes both internal and external bremsstrahlung. What we wish to report is the Q^2 and A_{ep} at the vertex which doesn't include either of these, as illustrated in Fig. 4.23. Since the GEANT4 simulation is used to determine the central Q^2 value only external bremsstrahlung needs to be corrected for.

This can be corrected for by running two simulations, one with the external bremsstrahlung turned on and the other with it off, and looking at the shift in the Q^2 between the two simulations. The difference in Q^2 between these simulations (*i.e.* the effect of external bremsstrahlung) is $0.11 \text{ m}(\text{GeV}^2)$, which leads to a $+0.44\%$ correction on Q^2 [52]. A conservative 50% error is assigned to this or 0.22% .

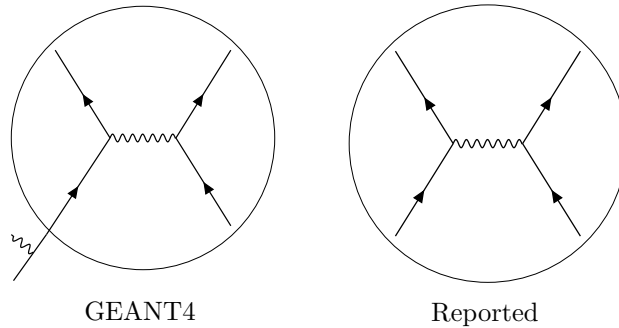


Figure 4.23: Cartoon for the radiative correction. GEANT4 doesn't include internal bremsstrahlung, but does include external bremsstrahlung (one diagram for which is illustrated in the left). On the right there is no external or internal bremsstrahlung which is what is reported for the Q^2 of the Q_{weak} experiment.

An earlier simulation using GEANT3 gave almost exactly the same result; they differed by 0.1% on the central value of Q^2 . To be conservative we chose to add this discrepancy in quadrature with the 0.22% uncertainty from above to yield 0.242% .

4.3.6 Q^2 Uncertainty Synopsis

The compilation of the results from all the studies in Sec 4.3 determines a total uncertainty on Q^2 , as listed in Table 4.3, of 0.446% . The proposal for the Q_{weak}

experiment had a goal for the uncertainty on $Q^2 = 0.5\%$, which was met. The Q^2 uncertainty is dominated by systematic uncertainties and not statistics.

Source	Error (%)	Running Total (Quadrature)(%)
Statistics	0.03	0.03
LH ₂ Target Location	0.117	0.121
Target Boiling	0.1	0.157
Raster Size	0.054	0.166
Beam Position	0.141	0.218
Beam Energy	0.19	0.289
Absolute B-Field	0.066	0.296
QTor Field Map	0.072	0.305
MD locations	0.024	0.306
Primary Collimator Location	0.206	0.369
Primary Collimator Imperfections	0.065	0.375
Radiative Corrections	0.242	0.446
Total (Quadrature Sum)	—	0.446

Table 4.3: The final uncertainties on the Q^2 measurement.

The simulation statistics which gave 0.03% uncertainty on Q^2 required ≈ 62.5 d of computing time on the JLab scientific computing farm. Each simulation in the previous sections needed anywhere between half or the same amount of simulations, using at least 8.6 yr of computing time.

Aside from the radiative corrections, the dominant sources of uncertainty are the primary collimator location, the target position along the beam line, beam energy, and the beam position. Three of these depend heavily on physical measurements of different aspects of the Q_{weak} experiment.

Spending more time to further lower the uncertainty on Q^2 would have little effect on the final result, as the uncertainty on the weak charge is dominated by other contributions, which are discussed in Sec. 5.2.

4.4 Q^2 Determination

The asymmetry data were taken in two separate running periods, Run 1 and Run 2, which had slightly different experimental conditions, and which were separated by a 6 month pause. The central value of Q^2 was taken from the GEANT4 simulation (Q_{G4}^2) and then corrected for each Run individually, and for the different light yield of the electrons traveling through different parts of the main detector bars, which will be discussed in Secs. 4.4.2 and 4.6.1.

The simulations used the Q_{weak} experiment's Run 2 configuration without the tracking chambers in because they slightly change the Q^2 value, providing a Q^2 value that is not equal to the main experiment. For electrons that travel through the main detectors and leave light which reaches the PMTs there is a Q^2 distribution as seen in Fig. 4.24. For Run 2 the central Q_{G4}^2 from the simulation is $24.595 \pm 0.007 \text{ m}(\text{GeV}^2)$. The statistical precision of this simulation thus provides a 0.03% uncertainty to Q^2 .

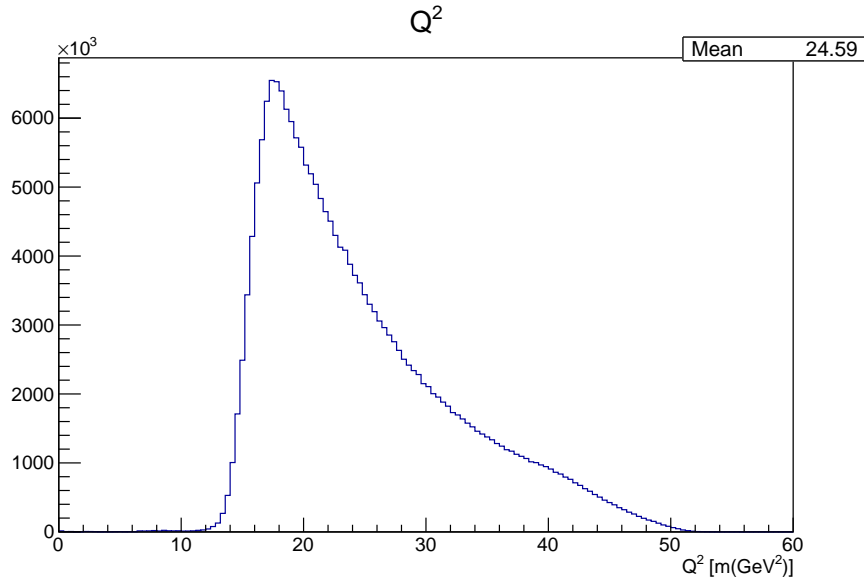


Figure 4.24: The Q^2 distribution from GEANT4 simulation for Q_{weak} 's Run 2 configuration.

In order to get the Q^2 for Run 1 ($Q_{\text{Run 1}}^2$) and Run 2 ($Q_{\text{Run 2}}^2$), corrections to the simulation value need to be made. These can be divided into two different corrections:

corrections due to differences between the conditions of the simulation and the data, and corrections due to differences in conditions between Run 1 and Run 2. These are discussed in the following sections.

4.4.1 Simulation to Data Correction for Run 2

Correcting for the difference between the simulations and the data was done by comparing at the Run 2 conditions for data and the simulation. The simulations were done in advance of knowing the final target position and beam energy. Because these are small effects and the simulations take a significant amount of time, updated simulations were not run. Table 4.4 shows the difference between the data and the simulation for the target position, beam current, and QTor current.

Property	Data		GEANT4	
	Run 1	Run 2	Run 1	Run 2
Target Position ⁵ (cm)	-652.466	-652.856	-652.67	-653.075
Beam Energy (MeV)	1161.09	1158.38	1159.65	1157.48
QTor Current (A)	8920.10	8899	8920.10	8899

Table 4.4: Differences between the Run 1 and Run 2 configurations in the Q_{weak} experiment and its GEANT4 simulation.

The Run 2 data has a beam energy that is 0.08% higher than was used for the simulation. Since $dQ^2/Q^2 \propto 2(dE_B/E_B)$ (Eq. 4.1) the effect the beam energy has on Q^2 is doubled, therefore the difference in beam energy increases the $Q_{\text{Run 2}}^2$ by 0.16% from the Q_{G4}^2 .

In both the data and the simulation the target position changes between Run 1 and Run 2. For both the data and the simulation the difference in the target position is ≈ 0.40 cm, and the difference between the data and the simulation are also approximately the same, with the largest for Run 2 at 0.219 cm. The position of the target affects Q^2 by $0.583\% \text{ cm}^{-1}$ as seen in Sec. 4.3.1.1. Therefore the 0.219 cm difference in target positions leads to a 0.128% increase in $Q_{\text{Run 2}}^2$ from Q_{G4}^2 .

⁵The target position is measured relative to the center of QTor.

A total increase of 0.288% from the Q_{G4}^2 is required to correct for the differences in the beam energy and target position between the simulation and data.

4.4.2 Extraction of Q^2 for Run 1

Correcting for the difference between Run 1 and Run2 can be done similarly to correcting the simulation to data for Run 2. The beam energy for Run 1 is 0.233% higher than Run 2 in the data; as in the last section, since $dQ^2/Q^2 \propto 2(dE_B/E_B)$ (Eq. 4.1) this means $Q_{\text{Run 1}}^2$ is 0.467% higher than $Q_{\text{Run 2}}^2$. Between Run 1 and Run 2 the difference in the target position is ≈ 0.40 cm, combining this with the target position affects on Q^2 by $0.583\% \text{ cm}^{-1}$ as seen in Sec. 4.3.1.1, means there the $Q_{\text{Run 1}}^2$ has a 0.234% increase from $Q_{\text{Run 2}}^2$. The change in the strength of QTor's magnetic field between Run 1 and Run 2 was calculated with a different beam energy therefore a 0.15% decrease in $Q_{\text{Run 1}}^2$ from $Q_{\text{Run 2}}^2$ as determined from tracking data [53].

Combining each of these $Q_{\text{Run 1}}^2$ is 0.55% higher than $Q_{\text{Run 2}}^2$. The Run 1 simulation gives results consistent with this difference.

4.5 Final Q^2

The $Q_{\text{Run 2}}^2$ is 0.288% higher than $24.595 \text{ m}(\text{GeV}^2)$ due to the beam energy and target position differences between the simulation and data. Also since GEANT4 includes external bremsstrahlung therefore an additional 0.49% increase in the $24.595 \text{ m}(\text{GeV}^2)$ also must be added, as discussed in Sec. 4.3.5. Therefore $Q_{\text{Run 2}}^2$ is,

$$\begin{aligned} Q_{\text{Run 2}}^2 &= 24.595 \text{ m}(\text{GeV}^2) \times 1.00288 \times 1.0049 \\ &= 24.787 \text{ m}(\text{GeV}^2). \end{aligned} \tag{4.5}$$

The $Q_{\text{Run 1}}^2$ is 0.55% higher than $Q_{\text{Run 2}}^2$ due to the differences in the beam energy,

target position, and QTor current. Thus $Q_{\text{Run 1}}^2$ is,

$$\begin{aligned} Q_{\text{Run 1}}^2 &= 24.787 \text{ m}(\text{GeV}^2) \times 1.0055 \\ &= 24.923 \text{ m}(\text{GeV}^2). \end{aligned} \tag{4.6}$$

Finally, applying the 0.446% uncertainty, the $Q_{\text{Run 1}}^2$ and $Q_{\text{Run 2}}^2$ are 24.923 ± 0.111 $\text{m}(\text{GeV}^2)$ and $24.787 \pm 0.111 \text{ m}(\text{GeV}^2)$, respectively.

4.6 Asymmetry Correction from Tracking

While the tracking system was mainly used for measuring the Q^2 , it was also used to make some corrections to the main asymmetry measurement. These corrections are (i) a lightweighting correction, which is due to the differences in the amount of light reaching the PMTs at different places across the MDs (ii) correcting for the acceptance of the Q_{weak} experiment and (iii) the effects of measuring over a range Q^2 while the final result required a single average Q^2 .

4.6.1 Lightweighting Correction

The amount of light detected by the PMTs at the end of each MD changes depending on where the electron passes through the bar, as illustrated in Fig. 4.25. In order to accurately determine the optical response of the MDs, tracking data is used to measure the light yield and Q^2 across the MD. Electrons passing through the ends of a bar have more total light detected by the PMTs than for those in the center of the bar, this affects the Q^2 which is reconstructed from the tracking data as illustrated in Fig. 4.26. Lightweighting means that each entry in the Q^2 distribution is weighted proportionally to the summed amount of the light seen in the two PMTs. This can be quantified by the ratio of calculated Q^2 with lightweighting, Q_{LW}^2 and without lightweighting, Q^2 , R_{Det} .

$$R_{\text{Det}} = \frac{Q^2}{Q_{\text{LW}}^2} \tag{4.7}$$

This has a 0.9895 ± 0.0021 effect on the Q^2 value [54]. The largest effects that contribute to this uncertainty are inefficiencies in the reconstruction of the tracks in the HDCs and VDCs, and variations between repeated measurements in different tracking periods.

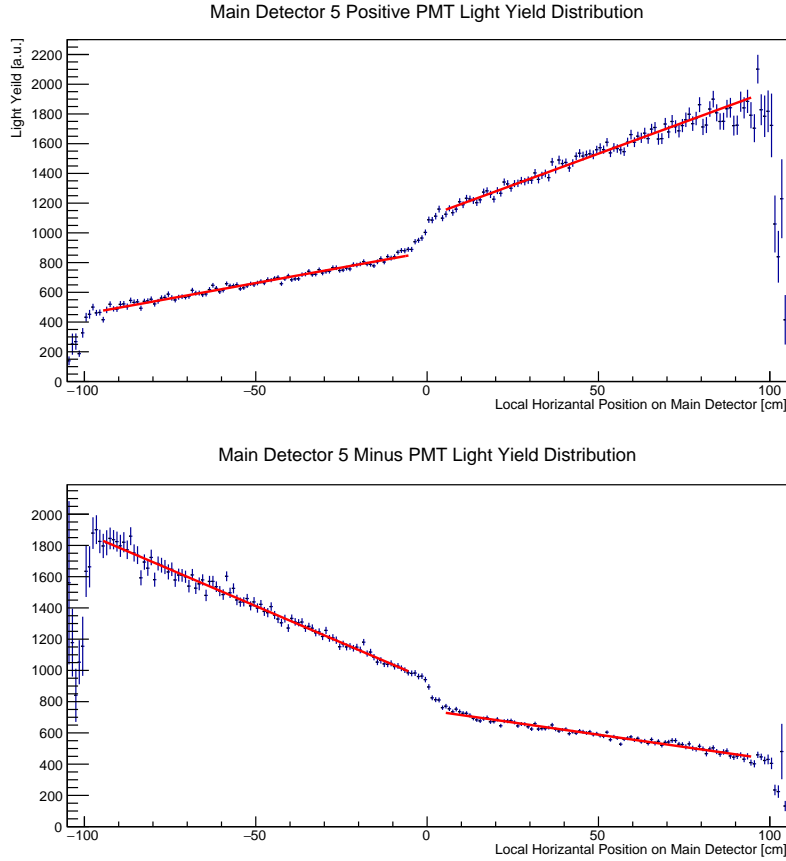


Figure 4.25: The distribution of the light yield across the MD as seen in the tracking data by each individual PMT for a typical MD bar. There is a higher light yield on the side of the bar where the PMT is, the discontinuity in the center of the bar is where the two 1 m quartz bars are glued together. The fits are there to help guide one's eye [55].

4.6.2 Acceptance Correction

The Q_{weak} experiment makes an average measurement of the asymmetry over the range of Q^2 , $\langle A(Q^2) \rangle$, however the final result that we wish to quote is the asymmetry at an average Q^2 , $A(\langle Q^2 \rangle)$. To correct for this, an acceptance correction factor (R_{acc}) is

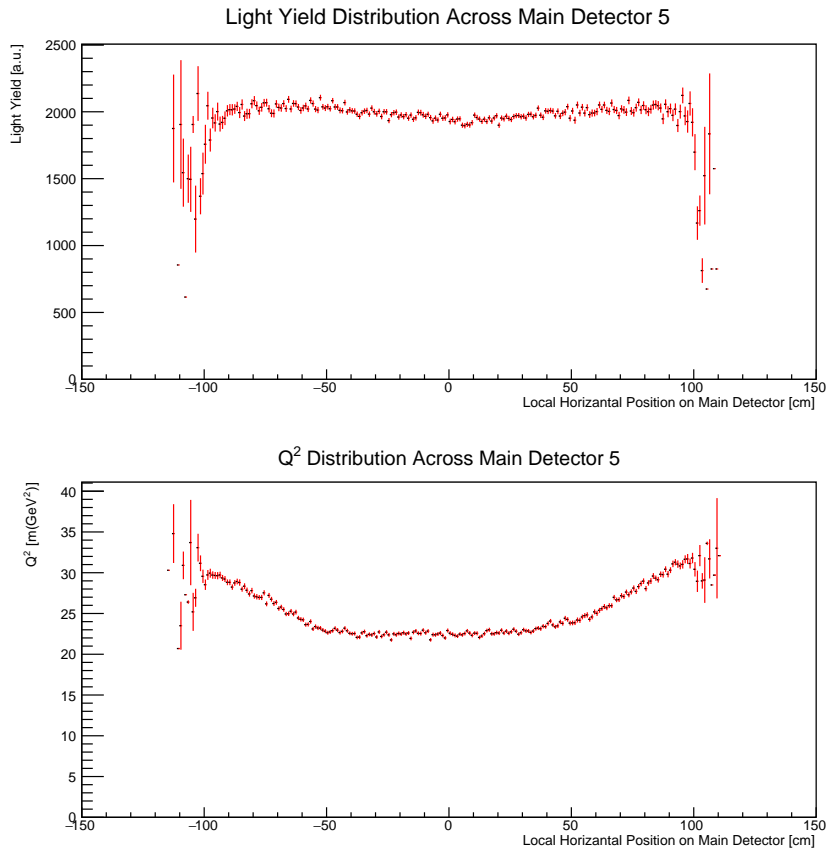


Figure 4.26: The distribution of the total light yield across the MD (top) and Q^2 (bottom), plotted vs. position of the electron track along the bar, for a typical detector bar in the tracking data.

defined,

$$R_{acc} = \frac{\langle A(Q^2) \rangle}{A(\langle Q^2 \rangle)}. \quad (4.8)$$

By using the GEANT4 simulation, $\langle A(Q^2) \rangle$ can be found like Q^2 in Fig. 4.24 for each MD. From the GEANT4 simulation Q^2 has an approximate range of 12.8 m(GeV²) to 48.5 m(GeV²), and the asymmetry has an approximate range of -548 ppb to -96.9 ppb. Then for each MD $\langle A(Q^2) \rangle$ can be calculated with the corresponding Q^2 from each one and Eq. 2.41. Averaging this ratio in all eight MDs gives $R_{acc} = 0.977$ with a statistical uncertainty of 0.001. Conservatively the “ B ” term in Eq. 2.41 is known to within 10% of itself providing a 0.002 uncertainty on Q^2 . Combining these, the acceptance correction factor is $R_{acc} = 0.977 \pm 0.002$ [56].

Chapter 5

Final Result from the Q_{weak} Experiment

5.1 Uncertainties on A_{ep}

The analysis of the asymmetry data is not the topic of this dissertation. The various corrections and sources of uncertainty were the responsibility of other collaborators (aside from R_{Q^2}), and so will be only briefly described in the following.

The raw asymmetry, A_{raw} , was first corrected for a number of false asymmetries as shown in Eq. 5.1, and then corrected for various experimental backgrounds, beam polarization, and multiplicative corrections as shown in Eqs. 5.2 and 5.3. All of these are defined in [22], and only the largest are outlined here.

$$A_{msr} = A_{\text{raw}} + A_T + A_L + A_{\text{BCM}} + A_{\text{BB}} + A_{\text{beam}} + A_{\text{bias}} \quad (5.1)$$

$$A_{\text{ep}} = R_{\text{tot}} \frac{A_{msr}/P - \sum_{i=1,3,4} f_i A_i}{1 - \sum_{i=1}^4 f_i} \quad (5.2)$$

$$R_{\text{tot}} = R_{\text{RC}} R_{\text{Det}} R_{\text{acc}} R_{Q^2} \quad (5.3)$$

The highest sources of systematic uncertainties were due to beam current monitoring (A_{BCM}), beamline background asymmetries (A_{BB}), beam asymmetries (A_{beam}), rescattering bias (A_{bias}), beam polarization (P), target windows (A_{b1}), and the kinematics (R_{Q^2}), which are summarized in Table 5.1.

Source	Run 1		Run 2	
	Error (ppb)	Fractional (%)	Error (ppb)	Fractional (%)
BCM Normalization: A_{BCM}	5.1	25	2.3	17
Beamline Background: A_{BB}	5.1	25	1.2	5
Beam Asymmetries: A_{beam}	4.7	22	1.2	5
Rescattering Bias: A_{bias}	3.4	11	3.4	37
Beam Polarization: P	2.2	5	1.2	4
Target Windows: A_{b1}	1.9	4	1.9	12
Kinematics: R_{Q^2}	1.2	2	1.3	5
Total of Others	2.5	6	2.2	15
Combined in Quadrature	10.1	—	5.6	—

Table 5.1: Final quadrature systematic uncertainties for sources with fractional contributions $((\sigma_i/\sigma_{\text{tot}})^2)$ of $\geq 5\%$ to A_{ep} on either Run 1 or Run 2.

A_{BCM} : The integrated signal for each helicity window is normalized to the integrated beam current during that helicity window. This is to eliminate any variation in the detector signals caused by any difference in current. The beam current was measured non-invasively with two BCMS in Run 1 and three BCMS in Run 2. The uncertainty was determined by comparing the results from the different BCMS.

A_{BB} : Secondary events can scatter off of the beamline or the tungsten collimator as they travel to the MDs. These events come from mostly low-energy neutrals and contribute only a small amount to the signal but were observed to have a large asymmetry. The contribution of these events to the MD signals was determined in special dedicated runs in which the main signal was blocked at the first collimator. The asymmetry of this background was monitored using the luminosity monitors. For more details see Emmanouil Kargiantoulakis' dissertation [57].

A_{beam} : The beam asymmetries are from non-vanishing fluctuations in the helicity-

correlated beam properties, these properties were transverse position and angle¹ and beam energy. These were monitored continuously throughout the Q_{weak} experiment using the BPMs. The sensitivity of the asymmetry to such fluctuations was calibrated by a system that deliberately varied these beam properties periodically. More details on the beam asymmetries can be found in Josh Hoskins' [33] and Donald Jones' dissertations [58].

A_{bias} : An unforeseen feature of the MDs was caused by the use of the Pb pre-radiator. The electron spin when it arrives at the MD is not purely longitudinal, but has a transverse component due to spin precession in the QTor magnet. Due to the transverse component of the electron's spin a left-right difference in the scattering probability will occur as it scatters off the Pb. This difference is parity-conserving and particularly large for the low-energy electrons in the electromagnetic shower in the Pb. The PMT at each end of MD measures a different amount of light across the bar as seen in Fig. 4.25. Therefore the two PMTS on a MD will measure a difference in the asymmetry, which should cancel when averaged for a perfect detector. Imperfect cancellation was modeled using simulation and input from the tracking data and was found to be small, with $A_{\text{bias}} = 4.3 \pm 3.0$ ppb.

P : Details on the beam polarization analysis with the Møller polarimeter can be found in Josh Magee's dissertation [59] and with the Compton polarimeter in Amrendra Narayan's [60] and Juan Carlos Cornejo's dissertations [61]. In Run 1 only the Møller polarimeter was used for determining the beam polarization, because the Compton polarimeter was being commissioned. However, in Run 2 both polarimeters were functional and their results were in excellent agreement and were combined.

A_{b1} : Al has a parity-violating asymmetry which is about an order of magnitude larger than that of the proton, therefore, like with the beam beamline background, any small contribution from electrons that scattered from the Al windows of the target to the overall signal will be a significant contribution to the asymmetry measurement.

¹The beam travels in the \hat{z} direction, therefore the direction transverse to the beam are the \hat{x} and \hat{y} directions.

Over the course of the Q_{weak} experiment dedicated time was taken in order to make a measurement of this asymmetry using a thin solid Al target. To determine the fraction of the light yield in the MDs that arises from Al ($\approx 2.5\%$), dedicated low current runs were taken in tracking mode with an evacuated target; details can be found in Josh Magee’s dissertation [59].

R_{Q^2} : The final of the largest sources of uncertainty is from the kinematics which is discussed in this dissertation.

5.2 Final Q_{W}^{P}

The final result for the Q_{weak} experiment has been submitted for publication. The measured asymmetry was $A_{\text{ep}} = -226.5 \pm 9.3$ ppb at $Q^2 = 24.8 \text{ m}(\text{GeV}^2)$. Table 5.2 summarizes the measured A_{ep} for Run 1, Run 2 and the combination of the two Runs. Both Run 1 and Run 2 have excellent agreement. Figure 5.1 shows the reduced asymmetry plot for all parity-violating electron scattering experiments on proton targets [22, 62–73]. This allows us to extract the value for the weak charge of $Q_{\text{W}}^{\text{P}} = 0.0719 \pm 0.0045$.

Property	Asymmetry (ppb)	Uncertainty (ppb)		
		Statistical	Systematic	Total
Run 1	−223.5	15.0	10.1	18.0
Run 2	−227.2	8.3	5.6	10.0
Run 1 and 2 combined with correlations	−226.5	7.3	5.8	9.3

Table 5.2: Final asymmetries A_{ep} and their statistical, systematic and total uncertainties for Run 1 and Run 2 and their combined values.

When compared to the SM prediction, $Q_{\text{W}}^{\text{P}} = 0.0708 \pm 0.0003$, it is seen that these are in good agreement.

While this result is in good agreement with the SM prediction it can also be used to put a limit on the mass of a hypothetical particle exchanged in the scattering process which is not predicted by the SM. Assuming an effective coupling for this

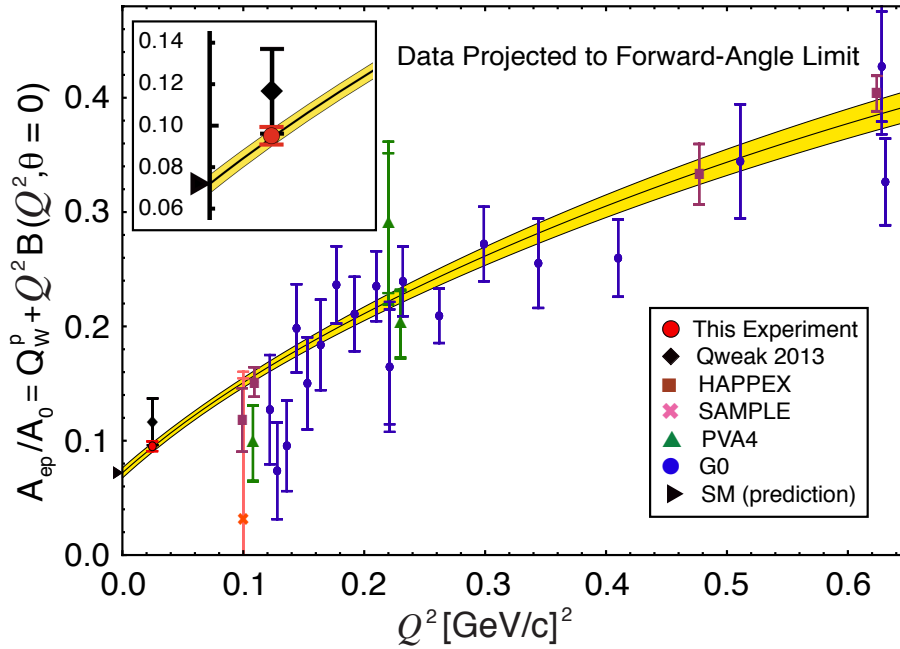


Figure 5.1: The reduced asymmetry $A_{\text{ep}}/A_0 = Q_W^p + B(\theta = 0, Q^2)Q^2$ vs. Q^2 . The solid line represents a global fit to the complete set of previous parity-violating electron scattering experiments, the yellow band indicates the fit uncertainty. The arrowhead at $Q^2 = 0$ indicates the Standard Model prediction for $Q_W^p = 0.0708 \pm 0.0003$, which agrees well with the intercept of the fit ($Q_W^p = 0.0719 \pm 0.0045$). The inset zooms in on the region around this experiment's result at $\langle Q^2 \rangle = 24.8 \text{ m}(\text{GeV}^2)$, where the upper datum is from an analysis of a short commissioning Run of the Q_{weak} experiment results [22], and the lower datum is from the full experiment reported here.

particle, g , lower limits for the mass of this hypothetical particle are given as $\Lambda_{\pm/g}$ [74]. The present result sets these lower limits at 7.5 TeV and 8.4 TeV for $\Lambda_{+/g}$ and $\Lambda_{-/g}$, where the two limits correspond to the upper and lower bounds of the experimental uncertainty.

More information on the final result of the Q_{weak} experiment and physics beyond the SM reach can be found in the upcoming paper.

5.3 Possible Improvements to Q^2

As discussed in Chap. 4 a final calibration of the HDC geometry is still underway. This is essential for an absolute measurement of the scattering angle for the tracking data.

Without this calibration the target location had to be determined by survey alone.

The original Q_{weak} experiment proposal included Gas Electron Multiplier (GEM) chambers as part of the tracking system [27]. The GEMs would have been placed 1 m downstream of the target and would have had a $100 \mu\text{m}$ position resolution which is better than the measured HDC resolution of $150 \mu\text{m}$ to $200 \mu\text{m}$ [28]. With this resolution and location they would have been the ideal way to improve the precision of the scattering angle measurement. Without these, only the HDCs were used for the scattering angle determination, which, as stated, limited the precision of the Q^2 measurement. Unfortunately, the GEMs were not available for the Q_{weak} experiment.

While what the tracking system measures is the Q^2 for the LH_2 and the Al walls, the Q^2 for LH_2 alone is what is required. During parts of the tracking periods the target was emptied and partially filled with H_2 gas. The plan was to use these tracking runs to be able to subtract the contribution to Q^2 from the Al walls. Only a few runs were taken in these conditions. Ideally more runs would have been taken, and so again, we relied on simulation for this correction.

Throughout the tracking periods during the Q_{weak} experiment there were some studies that would have been very helpful to have had, had the time been available. These could also be used to further bench mark the simulation. Since the GEMs were not part of the Q_{weak} experiment's apparatus they couldn't be used as a check for the HDCs calculation of the scattering angle. Another approach to be able to do this would be by blocking areas of one of the collimator octants. If a block with holes in specific places is placed into a collimator octant, the path of the electrons and their scattering angle is then known, and the reconstruction can be checked and calibrated².

In Sec. 4.3.4.3 cuts were made to the data on the distribution to see how any imperfections that the collimator might have would effect the Q^2 . While this is done with the data, it is done in the data analysis not during the data taking. Taking time to block part of the collimators while taking tracking data might have provided a better

²This technique is commonly used in Hall A at JLab and is known as a "sieve-slit" collimator calibration.

understanding of this effect and allow for checking the effect found in the data analysis.

Another example where more data would have been useful is the beam position and angle scan; these scans were only done with MDs (1, 3, 5 and 7) along the \hat{x} and \hat{y} directions, which were compared to the simulation as seen in Secs. 4.3.2.2 and 4.3.2.3. However it would have been useful to also have the done these scans with MDs (2, 4, 6, and 8) 45° to the \hat{x} and \hat{y} directions. For the scans where a direct comparison between the data and simulation were able to be done, there was only one beam scan which could be used. There was also an incomplete scan in the case of the beam \hat{y} angle with MDs 3 and 7 only MD 3 was working. Rather than just having a single scan, there would have been a benefit to having several of these scans, not just as a check on the simulation but also as a check on the scans themselves.

It would have been beneficial to have BPMs that would be able to measure the beam position at the beam currents used during tracking periods.

It should be noted that Q^2 was not measured at the same conditions as the asymmetry due to the factor of 10^6 difference in the beam current. To deal with this concern the Q_{weak} experiment did include a focal-plane scanner which had the goal of attaining a profile of the electrons on the face of one of the MDs in both tracking and integration parts of the experiment. The profiles were successfully compared up to a beam current of $\approx 50 \mu\text{A}$ however the scanner was not able to attain a profile at the full beam current of $180 \mu\text{A}$ [75].

Possible causes of a change in Q^2 with beam current are few. The location of the collimator and MDs, the QTor current do not change with beam current. However, target boiling would be impacted by a change in the beam current, this was looked at in Sec. 4.3.1.2 and provided a 0.1% uncertainty on Q^2 .

Chapter 6

Electron Beam Polarimetry

6.1 Theory of Møller Scattering

Møller scattering (see Fig. 6.1) refers to elastic electron-electron scattering ($e^-e^- \rightarrow e^-e^-$). It is a purely quantum electrodynamics (QED) process which was first calculated by Christian Møller in 1932 [76]. Since then it has been calculated with improved accuracy using the developments of new techniques in quantum field theory. Møller scattering has both a large cross section and a large theoretical asymmetry or analyzing power, or difference in the measured cross section for changes in the polarization of the beam or target, when both initial state electrons are polarized along the same axis. This analyzing power (A_{zz}) is shown in Eq. 6.1, where the spin of the electrons of the beam is denoted by \uparrow and \downarrow and the target is denoted by \uparrow ,

$$A_{zz} = \frac{\sigma_{\uparrow\uparrow} - \sigma_{\downarrow\uparrow}}{\sigma_{\uparrow\uparrow} + \sigma_{\downarrow\uparrow}}. \quad (6.1)$$

The analyzing power is energy independent making it a good way to measure the polarization of the electron beam.

The polarized differential cross section, $(d\sigma/d\Omega)_{zz}$, for Møller scattering is dependent upon the relative longitudinal polarizations of the electrons in the beam and the

¹Mandelstam variables are defined as $s = (p_1 + p'_1)^2$, $t = (p_2 - p_1)^2$, $u = (p'_2 - p_1)^2$, where for particles 1 and 2, p_1, p_2 and p'_1, p'_2 are the incoming and outgoing four-momentum respectively.

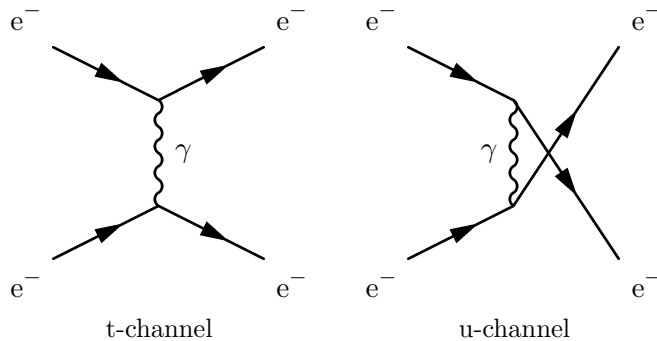


Figure 6.1: Lowest-order Feynman Diagrams for Møller Scattering. Møller Scattering happens through the t and u channel of the Mandelstam variables¹.

target, as seen in Eq. 6.2. Given the polarization of the electron beam (P_b^z) and target electrons (P_t^z) respectively, where A_{zz} is the analyzing power, and $d\sigma_0/d\Omega$ is the unpolarized differential cross section [2, 77], we have

$$\left(\frac{d\sigma}{d\Omega}\right)_{zz} = [1 + P_b^z P_t^z A_{zz}(\theta_{CM})] \frac{d\sigma_0}{d\Omega}. \quad (6.2)$$

The unpolarized differential cross section at high energy² depends on the center of mass scattering angle θ_{CM} (but not the azimuthal angle ϕ_{CM}) as shown in Eq. 6.3,

$$\frac{d\sigma_0}{d\Omega} = \left[\frac{\alpha(4 - \sin^2 \theta_{CM})}{2m_e \gamma \sin^2 \theta_{CM}} \right]^2, \quad (6.3)$$

where α is the fine structure constant, m_e is the mass of the electron, and γ is the relativistic Lorentz transformation factor. Finally A_{zz} for both electrons polarized in the same directions in the relativistic limit is independent of energy and only depends on θ_{CM} as shown in Appendix C.2, specifically for longitudinally polarized electrons this is

$$A_{zz}(\theta_{CM}) = \frac{-\sin^2 \theta_{CM}(8 - \sin^2 \theta_{CM})}{(4 - \sin^2 \theta_{CM})^2}. \quad (6.4)$$

For Møller scattering the maximum analyzing power, A_{zz}^{max} , is $-7/9$ at 90° as shown in Fig. 6.2. Møller scattering is an ideal way to measure the polarization of an electron

²For $E_B \gg m_e$, for details see Appendix C.2. The $E_B > 100$ MeV which are used in the HMolPol analysis qualify as high energy.

beam because of the energy independence of A_{zz} and large A_{zz}^{max} .

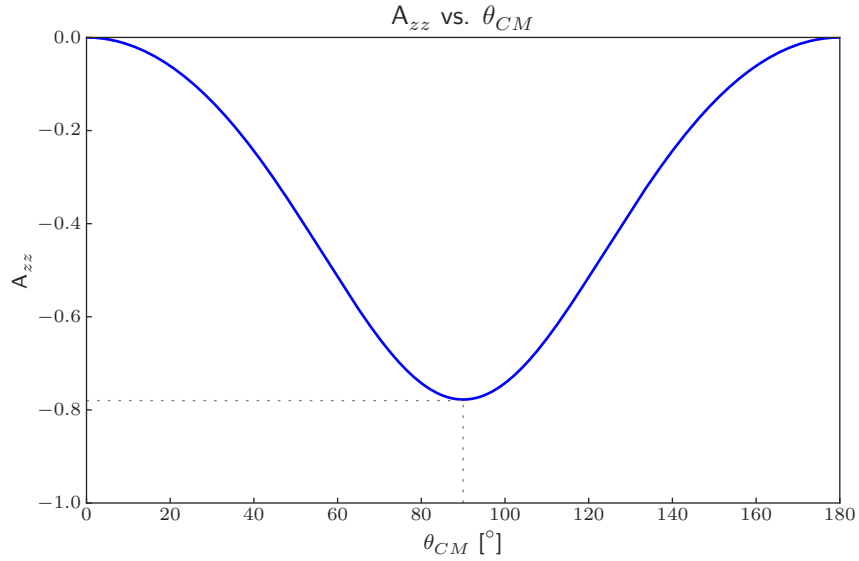


Figure 6.2: Møller scattering analyzing power vs. θ_{CM} . The analyzing power is $-7/9$ at $\theta_{CM} = 90^\circ$.

6.2 Theory of Compton Scattering

Compton scattering (see Fig. 6.3) refers to electron-photon ($e^- \gamma \rightarrow e^- \gamma$) scattering, which can also be used to find the polarization of an electron beam. This is achieved by scattering circularly polarized photons off of polarized electrons. At tree level

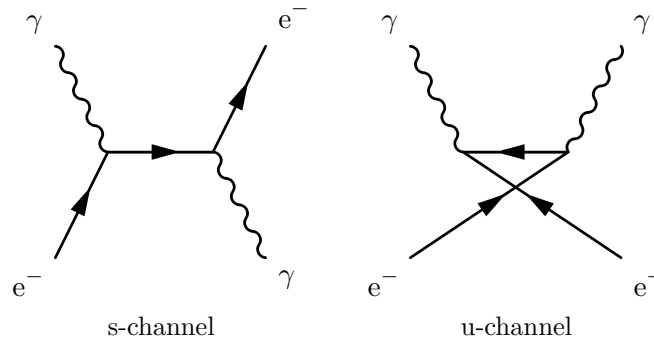


Figure 6.3: Lowest-order Feynman Diagrams for Compton Scattering. Compton Scattering happens through the s and u channel of the Mandelstam variables¹.

the differential cross section ($d\sigma/d\rho$), when integrating over the azimuthal angle ϕ ,

for longitudinally polarized electron beam with opposite momentum to the polarized photons is [78]

$$\frac{d\sigma}{d\rho} = \frac{d\sigma_0}{d\rho} \mp P_e P_\gamma \cos \theta_e \frac{d\sigma_1}{d\rho}, \quad (6.5)$$

where $d\sigma_0/d\rho$ is the unpolarized, $d\sigma_1/d\rho$ is the longitudinally spin-dependent cross sections, P_e and P_γ are the polarization of the electron and photon respectively, and θ_e is the spin of the electron with respect to its momentum (the $\hat{\mathbf{z}}$ direction). If the longitudinal component of the photon's spin is parallel to its direction of motion then the negative sign is chosen for the second term. The unpolarized cross section and longitudinally spin-dependent part of the cross section are

$$\frac{d\sigma_0}{d\rho} = 2\pi r_0^2 a \left\{ \frac{\rho^2(1-a)^2}{1-\rho(1-a)} + 1 + \left[\frac{1-\rho(1+a)}{1-\rho(1-a)} \right]^2 \right\}, \quad (6.6)$$

and

$$\frac{d\sigma_1}{d\rho} = 2\pi r_0^2 a \left\{ \left[1 - \rho(1+a) \right] \left[1 - \frac{1}{1-\rho(1-a)} \right]^2 \right\}. \quad (6.7)$$

Here r_0 is the classical radius of the electron³, $\rho = k_\gamma/k_\gamma^{max}$ the ratio of the scattered photon energy to the maximum scattered photon energy in the lab frame, and a is defined as,

$$a = \frac{1}{1 + \frac{4k_{\gamma 0} E_B}{m_e}}, \quad (6.8)$$

where $k_{\gamma 0}$ is the initial momentum of the photon in the lab frame and E_B is the electron beam energy. The maximum scattering energy for the photon happens in the case where the photon is back-scattered in the lab frame and is given by,

$$k_\gamma^{max} = \frac{4aE_B^2 k_{\gamma 0}}{m_e^2} \quad (6.9)$$

which is known as the Compton edge. The Compton edge correspond to the photon energy where the analyzing power (A_l) is at a maximum, and where $\rho = 1$. The

³Classical electron radius or, $r_0 = e^2/4\pi\epsilon_0 m_e$, is the radius of a sphere with charge e , when its electrostatic potential is equal to m_e [79].

analyzing power can be found by taking the ratio of Eqs. 6.6 and 6.7,

$$A_l = \frac{\frac{d\sigma_1}{d\rho}}{\frac{d\sigma_0}{d\rho}}. \quad (6.10)$$

Both the polarized and the unpolarized cross-sections are dependent upon energy, and these energy dependencies don't cancel when taking the ratio. Therefore the analyzing power is energy dependent. At the Compton edge the analyzing power becomes

$$A_l \Big|_{\rho=1} = A_l^{max} = -\frac{(a-1)^2}{1+a^2}, \quad (6.11)$$

where it can be seen that A_l still depends on a , thus A_l is dependent on the beam energy (E_B) and the initial momentum of the photon ($k_{\gamma 0}$).

6.3 Existing Polarimeter Technology

JLab, along with other laboratories past, present, and future which run parity-violating electron scattering experiments require knowledge about the polarization of the electron beam. Ideally a perfectly polarized electron beam is desired for electron scattering experiments. However, in reality this not possible due to engineering and physics limitations in producing 100% polarized electrons from polarized photons. For any polarized electron scattering experiment how much of the beam is actually polarized needs to be taken into account in the final calculation, so the precision with which the beam polarization is measured is important.

The Q_{weak} experiment reached a 0.6% [59] absolute measurement of the beam polarization and the future MOLLER experiment will require a 0.4% measurement to reach their systematic uncertainty goal [80]. In the past at JLab, Mott polarimeters, Møller polarimeters, and/or a Compton polarimeters, have been used to determine the beam polarization. Often multiple polarimeters are used at the same time to provide a redundant and more precise calculation of the beam polarization.

In order to find the polarization of the electron beam via a polarimeter of choice,

one must consider the relationship between the measured asymmetry, A_{msr} , and the analyzing power. For Møller scattering this relationship is completely independent of the beam energy, as shown in Eq. 6.4, while for Compton scattering this is dependent upon the beam energy, as seen in Eqs. 6.6, 6.7 and 6.10. Using A_{msr} , the polarization of the target, and the analyzing power, the P_b^z can be found using Eqs. 6.12 and 6.14 for Møller ($A_{msr}^{\text{Møller}}$) and Compton (A_{msr}^{Compton}) scattering respectively.

$$A_{msr}^{\text{Møller}} = P_b^z P_t^z A_{zz}(\theta_{CM}), \quad (6.12)$$

so

$$P_b^z = \frac{A_{msr}^{\text{Møller}}}{P_t^z A_{zz}(\theta_{CM})}, \quad (6.13)$$

and

$$A_{msr}^{\text{Compton}} = P_b^z P_\gamma A_l, \quad (6.14)$$

so

$$P_b^z = \frac{A_{msr}^{\text{Compton}}}{P_\gamma A_l}. \quad (6.15)$$

6.3.1 Møller Polarimeters

Present-day Møller polarimeters use magnetized ferromagnetic materials like iron (Fe) as the target, often at magnetic saturation. The target is placed in the beam line during times in the experiment that are dedicated to measuring the beam polarization. This is dedicated time because the target limits the beam current that can be used. High beam currents can melt a hole through the target or cause heating which in turn will depolarize the target. The target also degrades the beam properties making it unusable for the experiment.

The theoretical Møller scattering cross section assumes the scattering between two free electrons, which works for H, however for targets like Fe which has multiple electrons it is not the case. When such a target is placed in a magnetic field, the electrons in filled shells generally do not align with the field, so the polarization only

arises due to a fraction of electrons. The fraction of these electrons which align with the field is what determines the polarization of the target. A source of uncertainty arises from the binding energy and the inter-atomic motion that the inner shell electrons are subject to, meaning that the assumption of the target electron being free can't be made. These two effects will cause an over estimation of the calculated polarization of the beam, which is known as the Levchuk effect [81]. With a target that has only one electron there is no Levchuk effect, as there are no inner shell electrons.

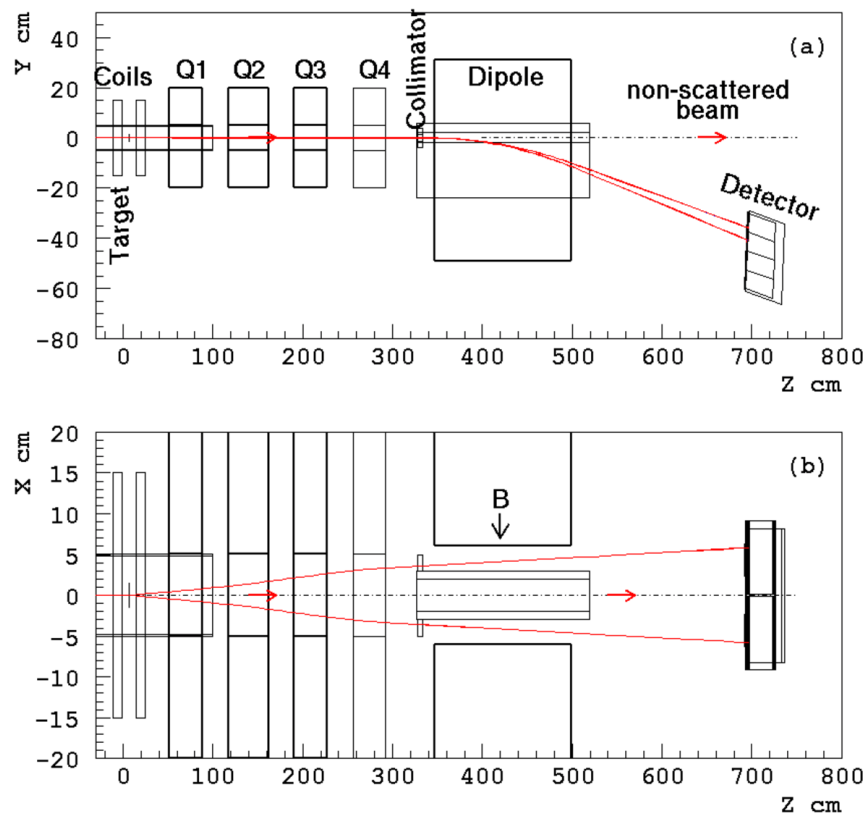


Figure 6.4: JLab's Hall A Møller polarimeter layout. The magnetic optics consisting of four quadrupoles focusing elements followed by a dipole bending element are shown. [82]

After the target, Møller polarimeters tend to have a series of magnetic elements to direct the scattered electrons away from the beam line and to focus the scattered electrons on to a detector. These magnetic optics also help select out the electrons that scatter closest to $\theta_{CM} = 90^\circ$ where the A_{zz} is maximized as discussed in Sec. 6.1. Occasionally, Møller polarimeters will also include collimators to help with the selection

and limiting of the detector acceptance. Figure 6.4 shows the layout of the Møller polarimeter in Hall A of JLab.

6.3.2 Compton Polarimeters

A Compton polarimeter uses polarized photons, which occasionally interact with the electron beam causing a small number of the electrons to scatter off the photons into a nearby detector. This is an example of a non-invasive polarimeter, like the Hydro-Møller, but unlike any existing solid target Møller polarimeters. Figure 6.5 shows the layout of the Compton polarimeter in Hall C. For a Compton polarimeter to work, the electron beam must be directed into the path of the polarized photons. A few of the electrons will then interact with some of the photons, both will scatter, and then either the electrons or the photons would be detected or both. The electrons in the beam that don't interact then will continue down the beamline to the experiment's target.

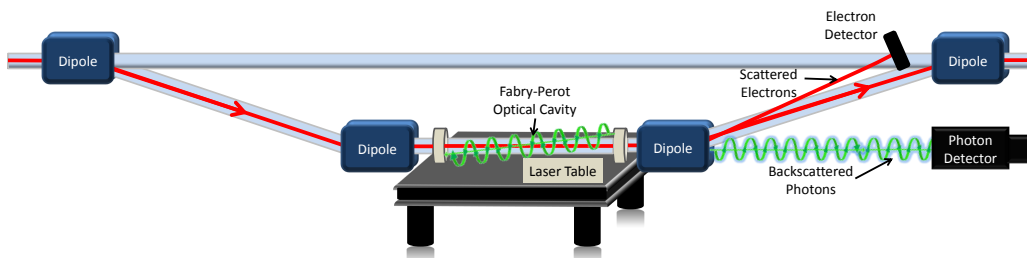


Figure 6.5: Schematic of JLab's Hall C Compton polarimeter [58]. The path of the beam is in red, it is directed from the beamline into the path of the laser by two dipoles and then back to the beamline by another two dipoles. The scattered electrons bend more when traveling through the first dipole after the laser than the ones that do not interact with the laser; the electron detector is placed in the path of the scattered electrons. The photon detector is placed directly behind the dipole to detect the scattered photons.

6.4 Advantages of a Hydro-Møller

The Hydro-Møller has some characteristics that are similar to either a Fe Møller polarimeter or a Compton polarimeter, but takes the best from both of these existing technologies, for example simultaneous measurement, and an energy independent analyzing power. Table 6.1 list various characteristics of these three polarimeters.

The relative uncertainties on the measured asymmetry for the existing Hall C Møller polarimeter that are limited by the Fe target include: the Levchuck effect (0.33%), target temperature (0.14%), Fe spin polarization (0.25%) and high-current extrapolation (0.50%); these contribute 0.66% to the overall systematic uncertainty of 0.84% [59]. The Hydro-Møller eliminates these contributions.

6.5 Future Needs for Precision Polarimetry

Two future parity violating experiments specifically are interested in using the Hydro-Møller: the P2 and MOLLER experiments. Each of these are briefly discussed in this section.

6.5.1 The P2 Experiment

The P2 Experiment [84] is planned to run at the new Mainz Energy Recovery Superconducting Accelerator (MESA) at Johannes Gutenberg University, Mainz, in Germany. By making a measurement of A_{ep} , it aims to determine $\sin^2 \theta_W$ to a precision of 0.13%, which will improve on the Q_{weak} experiment's measurement. The planned parameters the P2 experiment will require are similar to what Q_{weak} used. To meet the experiment's proposed figure of merit the following conditions are required: 10 000 hours of beam, a low Q^2 value ($4.5 \times 10^{-3} \text{ GeV}^2$), a highly polarized beam of $>85\%$, a high current beam ($150 \mu\text{A}$), and 155 MeV beam energy. One big difference between the P2 and Q_{weak} experiments will be the spectrometer magnet used to select out the elastically scattered electron from the target scattering flux. P2 will be using a solenoid magnet compared to Q_{weak} 's toroidal magnet. In order to reach their precision

Characteristic	Polarimeter		
	Fe Møller	Compton	Hydro-Møller
Invasive Measurement	Yes	No	No
Simultaneous Measurement	No	Yes	Yes
Levchuk Effect	Yes	No	No
Maximum Beam Current ⁴	Target (μA)	Experiment	Experiment
Systematic Uncertainty: Q_{weak} Achieved	0.84% [59]	0.59% [83]	—
Systematic Uncertainty: Proposed	—	—	0.5% [2]
Analyzing Power Energy Dependence	No	Yes	No
Target Depolarization	Yes	No	Negligible ⁵

Table 6.1: Comparison of the Fe Møller, Compton, and Hydro-Møller polarimeters. The characteristics that makes that polarimeter stand out compared to the other polarimeters are in bold.

⁴The maximum beam current is denoted as determined by either the target material or by an experiment's beam current.

⁵Estimation of the target depolarization is 0.004% with an upper limit of 0.01% [2, Sec 4.1.6].

they must know the beam polarization to better than 0.5%. One method which they have to measure the beam polarization is through an invasive double Mott polarimeter. The other will be via the Hydro-Møller, which will be vital for achieving this desired precision on their beam polarization. The technology of the Hydro-Møller is ideal for this application due to it being a continuous and non-invasive measurement of the beam's polarization.

6.5.2 The MOLLER Experiment

The MOLLER experiment [80], is planned to run at JLab making use of the 12 GeV upgrade. It will measure the weak charge of the electron, Q_W^e , via Møller scattering. The goal is to measure Q_W^e to 2.3% relative precision, which will improve on the results found by the SLAC E158 experiment which ran in 2002 and 2003 [19]. The experiment plans to use an 11 GeV electron beam with a polarization of 85% and current of $85 \mu\text{A}$; the Q_{weak} experiment showed that this should be attainable. Like the P2 and Q_{weak} experiments, the MOLLER experiment will use a low Q^2 value, designed to be $5.6 \times 10^{-3} \text{ GeV}^2$. In order to reach the desired precision on Q_W^e the beam polarization has to be measured to a precision of 0.4%. Employing existing technology in Hall A, both Møller and Compton polarimeters will allow independent measurements of the beam polarization. The former is well understood but invasive so would be used during certain dedicated times during beam delivery. The latter is noninvasive therefore can be run simultaneously. In addition it also allows for independent determination of the beam polarization via separate analysis of the scattered electrons and photons. While the two of these combined should be able to reach the desired precision on the beam polarization, the Hydro-Møller would provide another continuous noninvasive measurement of the beam polarization, through Møller scattering.

Chapter 7

Concept and Design of the Hydro-Møller

7.1 Hydro-Møller Concept

Here the concept of the Hydro-Møller is introduced, which will be a new Møller polarimeter that uses H gas as a target rather than an Fe target. Compared to the target of the Møller polarimeter discussed in Sec. 6.3.1, the Hydro-Møller's target will use H gas stored in a ultra-cold magnetic trap, which will provide a 100% polarization of the atomic electrons in the H gas. A diagram of the proposed apparatus can be seen in Fig. 7.1 [1, 2]. The Hydro-Møller target will be placed into the beam line, upstream of the target of the main experiment. First the H_2 will be dissociated into H, then it will be cooled down to 0.3 K and pumped into the storage cell. The H gas will be kept in the storage cell at 0.3 K and will be contained within a solenoidal magnetic field. In order to keep the H gas polarized, the magnetic field will have to be very strong; the proposed strength is 8.0 T as can be seen in Fig. 7.1 [1, 2]. Vacuum pumps will be placed right before and after the H target of the polarimeter in order to maintain the beam line upstream and downstream of the target as close to vacuum conditions as possible. The storage cell itself will have a thin coating of superfluid ^4He , which will aid in maintaining the polarization and atomic state of the hydrogen gas.

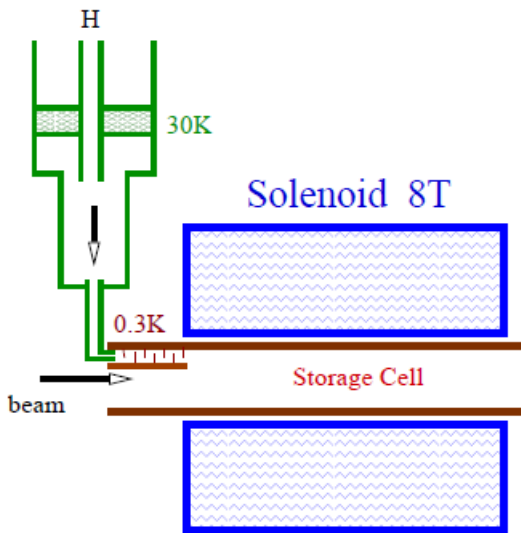


Figure 7.1: Schematic of the Hydro-Møller [1, 2]. The dissociator (green) is feeding the H gas into the storage cell (red) enveloped by the 8.0 T solenoid magnetic (blue).

7.2 Electron Polarization States of Atomic Hydrogen

One crucial requirement for the Hydro-Møller is the polarization of the H. While H is the most abundant element in the universe it does not exist in its atomic form on Earth, rather it prefers to form bonds with other atoms. Because of this, H_2 will have to be dissociated into atomic hydrogen; this will be discussed in Sec. 7.3.1. Once atomic hydrogen atoms are created they must be polarized and have a long lifetime.

The electrons and protons in the ground state of H split into four different eigenstates as shown in Table 7.1, where the spins are denoted by \uparrow and \downarrow for the proton and \uparrow and \downarrow for the electron. The basic Hamiltonian, \mathcal{H} , for a hydrogen atom is shown in Eq. 7.1.

$$\mathcal{H} = A\hat{i}\cdot\hat{s} + g_e\mu_B\vec{B}\cdot\hat{s} - g_p\mu_N\vec{B}\cdot\hat{i}. \quad (7.1)$$

Here A is the hyperfine splitting energy for the ground state, \hat{i} is the spin of the proton, \hat{s} is the spin of the electron, μ_B and μ_N are the Bohr and nuclear magnetons respectively, g_e and g_p are the spin g-factors for the electron and proton respectively, and \vec{B} is the magnetic field in the \hat{z} direction.

State	Wave Function	Energy	
$ d\rangle$	$ \uparrow\uparrow\rangle$	$A - \mu_+ B$	High Energy
$ c\rangle$	$\sin\theta \cdot \downarrow\uparrow\rangle + \cos\theta \cdot \uparrow\downarrow\rangle$	$A\left(-1 + 2\sqrt{1 + \left(\frac{\mu_- B}{2A}\right)^2}\right)$	
$ b\rangle$	$ \downarrow\downarrow\rangle$	$A + \mu_+ B$	Low Energy
$ a\rangle$	$\sin\theta \cdot \uparrow\downarrow\rangle - \cos\theta \cdot \downarrow\uparrow\rangle$	$A\left(-1 - 2\sqrt{1 + \left(\frac{\mu_- B}{2A}\right)^2}\right)$	

Table 7.1: Eigenstates and energies for atomic H.

From this Hamiltonian the energies associated with each of the states can be found (see Appendix B). Table 7.1 lists these energies using the following definitions: μ_+ and μ_- are defined as $\mu_+ \equiv -g_e\mu_B + g_p\mu_N$ and $\mu_- \equiv -g_e\mu_B - g_p\mu_N$. For the mixed states, $|a\rangle$ and $|c\rangle$ the mixing angle, θ is determined by Eq. 7.2,

$$\tan 2\theta = \frac{A}{\hbar\gamma_e\gamma_p B}, \quad (7.2)$$

where, \hbar is the reduced Planck constant, and γ_e and γ_p are the gyromagnetic ratios of the electron and proton, respectively [85, 86].

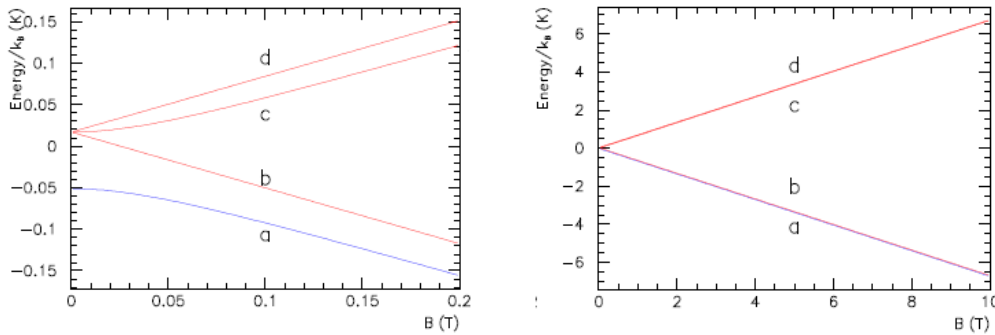


Figure 7.2: The splitting of energy levels for H for the four states in Table 7.1, for low magnetic fields (0 T to 0.2 T) on the left, and high magnetic fields (0 T to 10 T) on the right [1, 2]. Here k_B is the Boltzman constant therefore the y-axis is in units of temperature.

As shown in Fig. 7.2, for H at the proposed temperature of 0.3 K and solenoid strength of 8.0 T, the H gas will predominantly populate the $|a\rangle$ and $|b\rangle$ states. For H in the ground state, using Eq. 7.2 and for $A = 5.884 \times 10^{-6}$ eV, the angle θ can be found to be $\tan 2\theta \approx \frac{0.05 \text{ T}}{B(\text{T})}$. Then in a solenoid of 8.0 T, $\tan 2\theta \approx 0.006$. Then it

follows that $\cos \theta \approx 0.999$, therefore most of the H populates the $|\downarrow \downarrow\rangle$ and $|\downarrow \uparrow\rangle$ spin states, meaning almost all of the electrons are in the same spin state.

7.3 Requirements on the Hydrogen Gas Target

There are many aspects that need to be investigated in order to accomplish building the Hydro-Møller. One of these is the dissociation of H_2 to H; this is outside the scope of this dissertation, but a brief history of this is provided in Sec. 7.3.1.

To make the Hydro-Møller feasible the atomic H gas must have a long lifetime. The lifetime can be limited by depolarization as well as recombination into H_2 . By changing the environment through decreasing the temperature and also polarizing the H in a strong magnetic field the lifetime can be greatly increased. This was first shown in 1980 by I. F. Silvera and J. T. M. Walraven where the H had a lifetime of up to 532 s (8.87 min) [87]. The lifetime of the H gas can be affected by thermal escape through the magnetic field gradient and recombination of the H gas both within the volume and from interactions on the surface of the storage cell [1, 2, Sec. 2.3].

The H gas can be contaminated by unpolarized sources, which can come from atoms or molecules. The contamination can be from the H atoms through their high energy $|c\rangle$ and $|d\rangle$ states. Other possible sources of contamination are H_2 molecules and their excited states, He, and other residual gases in the storage cell [1, 2, Sec. 2.5].

Finally, the electron beam will have an impact on the H gas, as it travels through to the main experiment. This impact can be from the H gas heating by ionization energy and H gas excitation, and depolarization by the ionization losses. Other impacts include the heat load of the beam on the cell and depolarization by the radio-frequency (RF) electromagnetic radiation of the beam [1, 2, Chap. 3].

Some resources for more information on each of these and the dissociation of H_2 can be found in [2, 85–100].

7.3.1 Dissociation of Diatomic Hydrogen

The Hydro-Møller will need polarized atomic hydrogen gas which has a long lifetime; this has successfully been done for many years, and a detailed summary and description of this work through 1986 can be found in [88].

RF dissociation of H_2 has been done at room temperature by J. T. M. Walraven and I. F. Silvera [97]. Liquid-nitrogen and liquid-helium RF dissociation along with the confinement of the produced atomic hydrogen was first shown by S. B. Crampton *et al.* and W. N. Hardy *et al.* respectively [89, 93, 101].

At low temperatures dissociation has been done by feeding H_2 inside of a dissociator placed in a Dewar. RF pulses are injected into the Dewar. The frequency of the RF pulses are chosen based on the strength of an external magnetic field. This frequency is determined by the transition between the hyperfine states; this is discussed in more detail in [86].

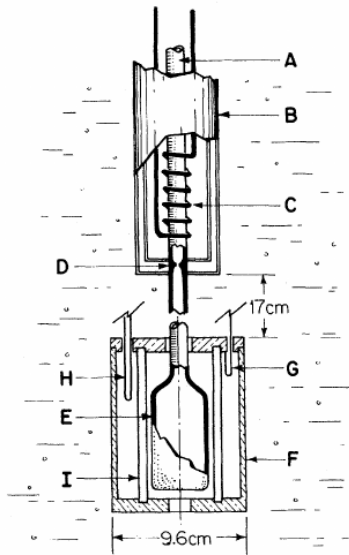


Figure 7.3: Schematic of the apparatus used by S. B. Crampton *et al.* [89]. H_2 is fed in from the top of the dissociator (A) which is placed in a liquid-nitrogen Dewar (B), the H is then stored in the bulb at the bottom (E) which is immersed in liquid helium.

For the Hydro-Møller design, the dissociator is above the target cell and the H gas is placed in the beam line, as shown in Fig. 7.1. This is unlike the early linear designs

which had the H gas fed into a cell at the end of the dissociator, *e.g.* Fig. 7.3 [89].

In the early 1990s T. Roser *et al.* and W. A. Kaufman *et al.* worked on the development of an atomic H beam [102, 103] shown in Fig. 7.4. The schematic of Hydro-Møller apparatus has a similar design. Unlike the previous dissociators and storage cells, this design is closer to what would be needed at JLab and MAMI.

The vertical section is the dissociator, where the H is produced by an RF dissociator. The horizontal section consists of a high-field solenoid magnet similar to the design for the Hydro-Møller (see Fig. 7.1). Instead of a storage cell, it has a mixing chamber from which the polarized H beam exits the apparatus.

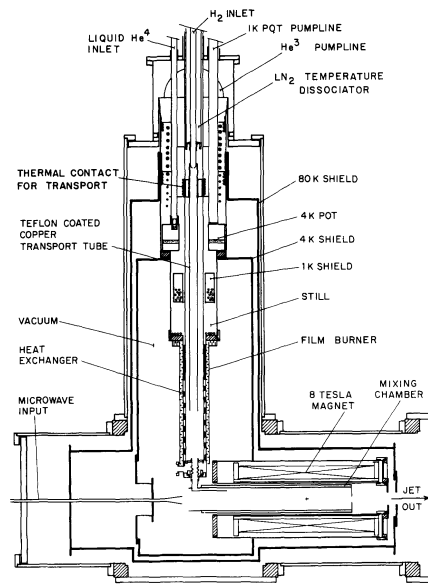


Figure 7.4: Schematic of the apparatus used for creating electron polarized H beam at the University of Michigan [102, 103]. H_2 is fed into the top of the dissociator, traveling down to the outlet the H_2 is cooled, dissociated into H atoms, and polarized before exiting on the right, creating a polarized H beam.

More details on spin-polarized atomic hydrogen can be found in [88].

Chapter 8

The Hydro-Møller Simulation: HMolPol

8.1 HMolPol Simulation

A general-purpose Monte-Carlo simulation was written for the Hydro-Møller polarimeter. It was needed in order to determine possible detector systems, backgrounds, rates, and study feasibility. Using GEANT4 C++ libraries [37], the HMolPol simulation was written for the Hydro-Møller. HMolPol uses GDML [104] for the geometry implementation, which allows the simulation to be used easily with different geometries and targets if needed. This will allow easy changes to reflect the specific target, simple detectors, or magnetic optics of the Hydro-Møller at JLab or Johannes Gutenberg University, Mainz. Presently, HMolPol includes the atomic H gas target, detector(s), and magnetic optics modeled after the JLab Hall A Fe Møller magnetic system.

8.1.1 Primary Generator

For each event that occurs in HMolPol, the Møller scattered and recoiling electrons are generated. Their generation is at a uniform random point within the length of the H gas in the target for given beam raster in \hat{x} and \hat{y} direction of where the electron beam was. This raster was set to $0.0 \text{ mm} \times 0.0 \text{ mm}$ for all of the simulations that are

included in this dissertation. The angles at which the Møller electrons scattered are chosen isotropically, points are chosen randomly on a sphere in the center of mass frame. Specifically the θ_{CM} scattering angle is randomly selected by taking the arccos of a randomly chosen value between $\cos 0^\circ$ to $\cos 180^\circ$ for a θ_{CM} range of 0° to 180° , or within a specified range in θ_{CM} stated at the beginning of a run. Likewise, the ϕ_{CM} scattering angle was generated uniformly over the range 0° to 360° , or within a specified range in ϕ_{CM} stated at the beginning of a run. The momentum of both primary Møller electrons is totally determined, as the ϕ_{CM} angle for the two primaries differ by 180° and the θ_{CM} angle for the two primaries total 180° . Along with the momentum of both particles their lab scattering angles, θ_{Lab} and ϕ_{Lab} are also determined by the appropriate boost from CM to Lab frames. Using Eqs. 6.3 and 6.4 and the variables determined above, the un-polarized differential cross-section and the analyzing power is calculated.

8.1.2 Atomic Hydrogen Target

The physical dimensions of the H target in the simulation are defined by the proposal for this polarimeter by E. A. Chudakov and V. G. Luppov [1, 2]. Figure 7.1 shows the layout of the Hydro-Møller target for the Monte Carlo. The target consists of a cylindrical 40.0 cm long copper storage cell with an inner radius of 2.0 cm and an outer radius of 3.0 cm.

Based on calculations done in the proposal for the Hydro-Møller the H gas is concentrated only in the center of the target [1, 2]. Figure 8.1 shows the predicted relative density and the relative difference in the magnetic field strength compared to the central value. From this, an effective length can be chosen for the HMolPol target of 20.0 cm where the density of H gas and the strength of the magnetic field are approximately constant. The H gas is placed in the center of this cell with a length of 20.0 cm. The 8.0 T solenoidal field is generated by GEANT4 and is ideal and located around just the H gas. All the properties of the H gas in HMolPol are summarized in Table 8.1. Figure 8.2 shows the target from HMolPol; the Cu cell is in gray and the H

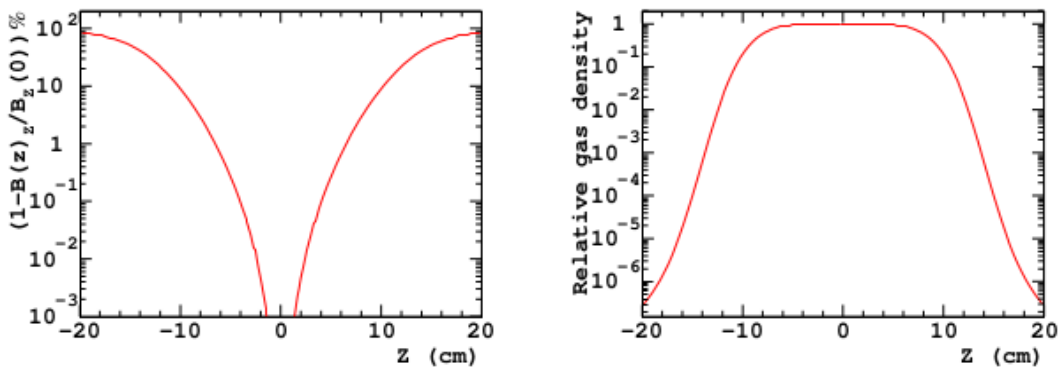


Figure 8.1: Left: plot of the relative differences of the magnetic field strength of the solenoid with respect to the field at the center. Right: relative gas density in the target along the solenoid’s axis [1, 2]. Both the field strength and the density of the H gas can be taken to be constant for Z from -10 cm to 10 cm giving an effective length of 20.0 cm for both of these.

gas is in green.

Property of H gas	Value
Length (cm)	20.0
Radius (cm)	2.0
Temperature (K)	0.3
Number Density (cm^{-3})	3×10^{15}
Pressure (Torr)	1×10^{-15}

Table 8.1: The parameters used for the H gas in HMolPol.

8.1.3 Detectors

HMolPol has been written to allow simulations of various types of detectors. Two have been used for initial studies. The first is the “Dummy detector”, or DummyDet, which consists of a single thin cylindrical plane of kryptonite¹ whose center is placed 7.47 m downstream of the center of the target, corresponding to the distance between the target and detector in the present Møller polarimeter in Hall A [105]. The second type of detector, the “LeftRight detector” or LeftRightDet, is a set of detectors which are equal in size and placed equal distance from the beam center along the \hat{x} -axis. As the

¹Kryptonite, is a special GEANT4 material that immediately kills every particle track that hits an object made of it.

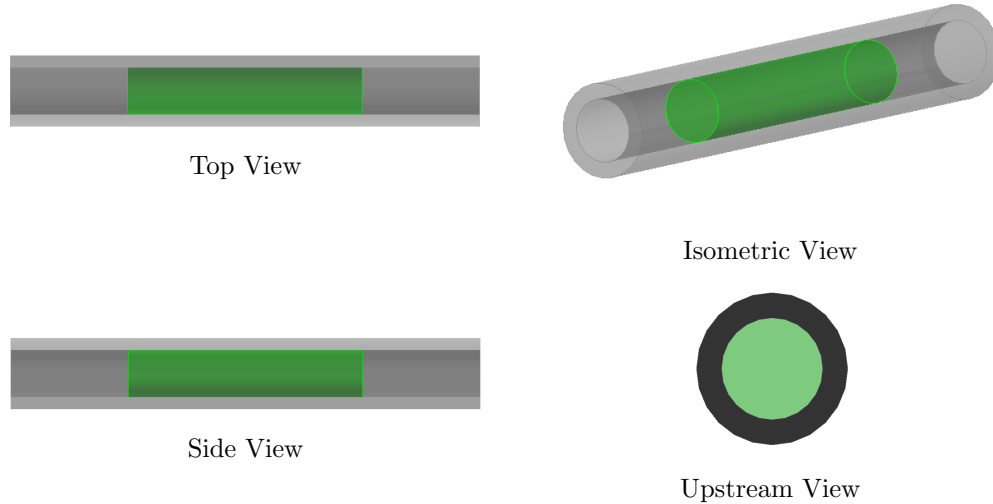


Figure 8.2: The target as implemented in the HMolPol simulation. The H gas is in green, and the Cu storage cell is in gray.

simulation develops, the type of detector(s) used, their material, shape, and location can be optimized for the Hydro-Møller apparatus.

8.1.4 Input/Output

The information stored about the particles as they travel through a detector is called a hit. Each detector type stores the information about the hits in all detectors of that type in the simulation. For a simulation that has more than one detector of the same type, all the hits for all the detectors of that type are stored in the same branch, which includes individual detector names and detector IDs. Using these, information about specific detectors of a type can easily be obtained. Each hit stores information about where it happened at that point; these include the momentum of the particle, where the interaction took place and what primary particle the hit is associated with.

Depending upon the detector configuration, one can detect either “primary 1” or “primary 2”, or both of the primary electrons. Ideally, detecting both of the primary electrons in coincidence would be done during an experiment to suppress backgrounds such as Mott scattering (*i.e.* ep scattering). However, due to the size of the DummyDet, all of the primary electrons generated in these simulations are detected for every event,

therefore all events will have a coincidence between two primaries. Because of this, the analysis in this dissertation has been done by looking purely at primary one, and thus no information is lost. In the case of using LeftRightDet, this is not necessarily the case and all three cases must be looked at separately.

8.1.5 Hall A Magnetic Optics

Since in Hall A at JLab there is an existing Møller polarimeter, it would be ideal if the same magnetic optics were able to be used for the Hydro-Møller. In order to study this, the existing magnetic optics from Hall A have been added to HMolPol.

The Hall A optical system consists of four quadrupole magnets and one dipole magnet as seen in Fig. 6.4. The size, distances between the magnets and the target, and their rotations were placed in HMolPol [105, 106]. All simulations made with the Hall A magnetic optics used the locations summarized in Table 8.2.

Hall A Magnet	Location (m)	Pitch (°)	Yaw (°)	Roll (°)
Quadrupole 1	0.683	-0.010	0.033	-44.980
Quadrupole 2	1.336	-0.024	0.038	-44.957
Quadrupole 3	2.022	0.011	-0.015	-44.996
Quadrupole 4	2.677	0.019	-0.067	-45.023
Dipole	4.165	0.025	-0.007	0.035

Table 8.2: The locations of the Hall A magnets from the center of the H gas target to the center of the magnet placed in HMolPol and rotation angles around the center of the magnet [105, 106]. The quadrupoles and dipole have an aperture of approximately 10 cm.

The field for each magnet is associated with the volume, which is generated by GEANT4 and is an ideal field existing only within the volume. They do not include fringe field effects. Figure 8.3 shows the implementation of the JLab Hall A magnetic optics in HMolPol.

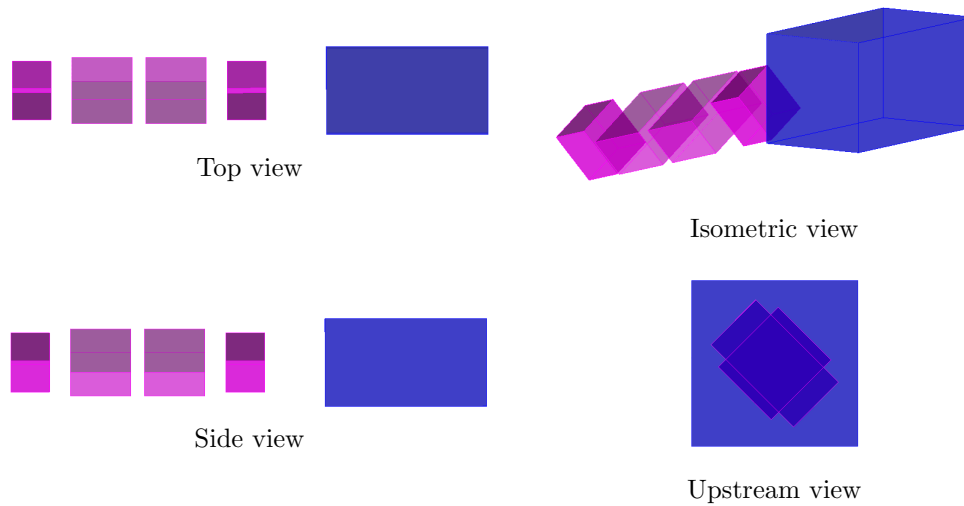


Figure 8.3: The Hall A magnetic optics as implemented in HMolPol. The four quadrupoles are in magenta, and the dipole in purple. In the top, side and isometric views, the electron beam travels from left to right, first passing through the four quadrupoles, followed by the dipole. The electron beam travels out of the page in the upstream view.

8.2 HMolPol Analysis

As discussed in Sec. 6.1, for Møller scattering at $\theta_{CM} = 90^\circ$, the A_{zz} is at a maximum. The A_{zz} is near its maximum within $\pm 15^\circ$ of 90° (see Fig 8.4). Thus, Monte Carlo events were thrown over a θ_{CM} range from 75° to 105° and a ϕ_{CM} range from 0° to 360° .

For this analysis only hits from the primary electrons are considered, as a way to isolate the hits that are not from secondaries. Secondaries would be of interest in a more sophisticated simulation aimed at investigating the details of detector response. To eliminate hits from secondaries created outside of the detector that make it into the detector, any hit used must be from an electron created in the target. Only the first hit which is from a primary electron created in the target is used, and this is referred to as the “naïve” primary.

The following sections discuss the initial analysis of simulations to both benchmark the Monte Carlo, and to gather information on basic aspects for the appropriate beam energies for MAMI and JLab, and the effect of the JLab Hall A Magnetic Optics. Both

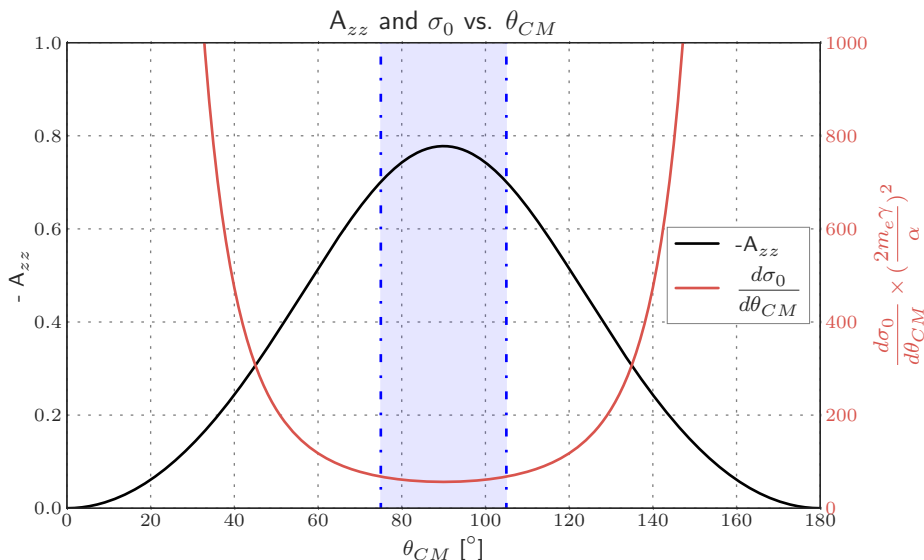


Figure 8.4: The normalized differential cross section with respect to θ_{CM} on the right axis in red and the A_{zz} on the left axis in black, vs. θ_{CM} for Møller scattering. The blue shaded region illustrates the θ_{CM} range used in the HMolPol simulations. Over this range both the A_{zz} and the cross section can be considered constant. Ideally the range in θ_{CM} that would be detected with the Hydro-Møller would be smaller than the range of θ_{CM} for generated events in these simulations.

analyses look at the distribution of θ_{CM} on the face of the DummyDet. Section 8.2.1 examines the σ_0 , A_{zz} , and the rate for different beam energies. Finally, Sec. 8.2.2 investigates how the JLab Hall A magnetic optics affect the distribution of θ_{CM} on the face of the DummyDet. These initial analyses can help with future simulations and analysis of possible designs of detectors and magnetic optics.

8.2.1 Beam Energy Scan

Multiple simulations were run at different beam energies with the only geometry being the target and the DummyDet. The impact of the beam energy on the cross section, σ_0 , analyzing power, A_{zz} , and the unpolarized rate normalized to the beam current, \widetilde{R}_0 was examined and the results are summarized in Table 8.3. Four beam energies were chosen for the simulation, similar to what one would find at MAMI: 100 MeV, 150 MeV, 200 MeV, and 250 MeV, and five beam energies for Hall A at JLab: 2.2 GeV, 4.4 GeV, 6.6 GeV, 8.8 GeV, and 11.0 GeV. The unpolarized rate normalized to the

beam current, \widetilde{R}_0 is calculated using the luminosity normalized to the beam current, $\widetilde{\mathcal{L}}$ and A_{zz} ,

$$\widetilde{R}_0 = \widetilde{\mathcal{L}}\sigma_0. \quad (8.1)$$

The rate, R then can be found from the following equations,

$$\begin{aligned} R &= I_B [1 + P_t^z P_b^z A_{zz}(\theta)] \widetilde{R}_0 \\ &= I_B [1 + P_t^z P_b^z A_{zz}(\theta)] \widetilde{\mathcal{L}}\sigma_0. \end{aligned} \quad (8.2)$$

The full calculation of the rate can be found in Appendix D.1.

The A_{zz} is only dependent on θ_{CM} , so it is the same over all these energies. However, σ_0 and therefore \widetilde{R}_0 does have an energy dependence, which decreases as the beam energy increases, as seen in Table 8.3. The rate can influence the type of detector material and the design of a detector system that is developed.

E_B (MeV)	σ_0 (μb)	$-A_{zz}$	\widetilde{R}_0 ($\text{Hz } \mu\text{A}^{-1}$)
100	6290	0.752	2350
150	4200	0.752	1570
200	3110	0.752	1180
250	2520	0.752	944

E_B (GeV)	σ_0 (μb)	$-A_{zz}$	\widetilde{R}_0 ($\text{Hz } \mu\text{A}^{-1}$)
2.2	287	0.752	108
4.4	144	0.752	53.8
6.6	95.7	0.752	35.9
8.8	71.8	0.752	26.9
11.0	57.4	0.752	21.5

Table 8.3: The unpolarized cross section, σ_0 , analyzing power, A_{zz} , and rate due to the unpolarized cross section, only normalized to beam current, \widetilde{R}_0 for various beam energies. On the top are beam energies in MeV, which are similar to energies that would be used at MAMI. On the bottom are beam energies in GeV which are similar to that available at JLab.

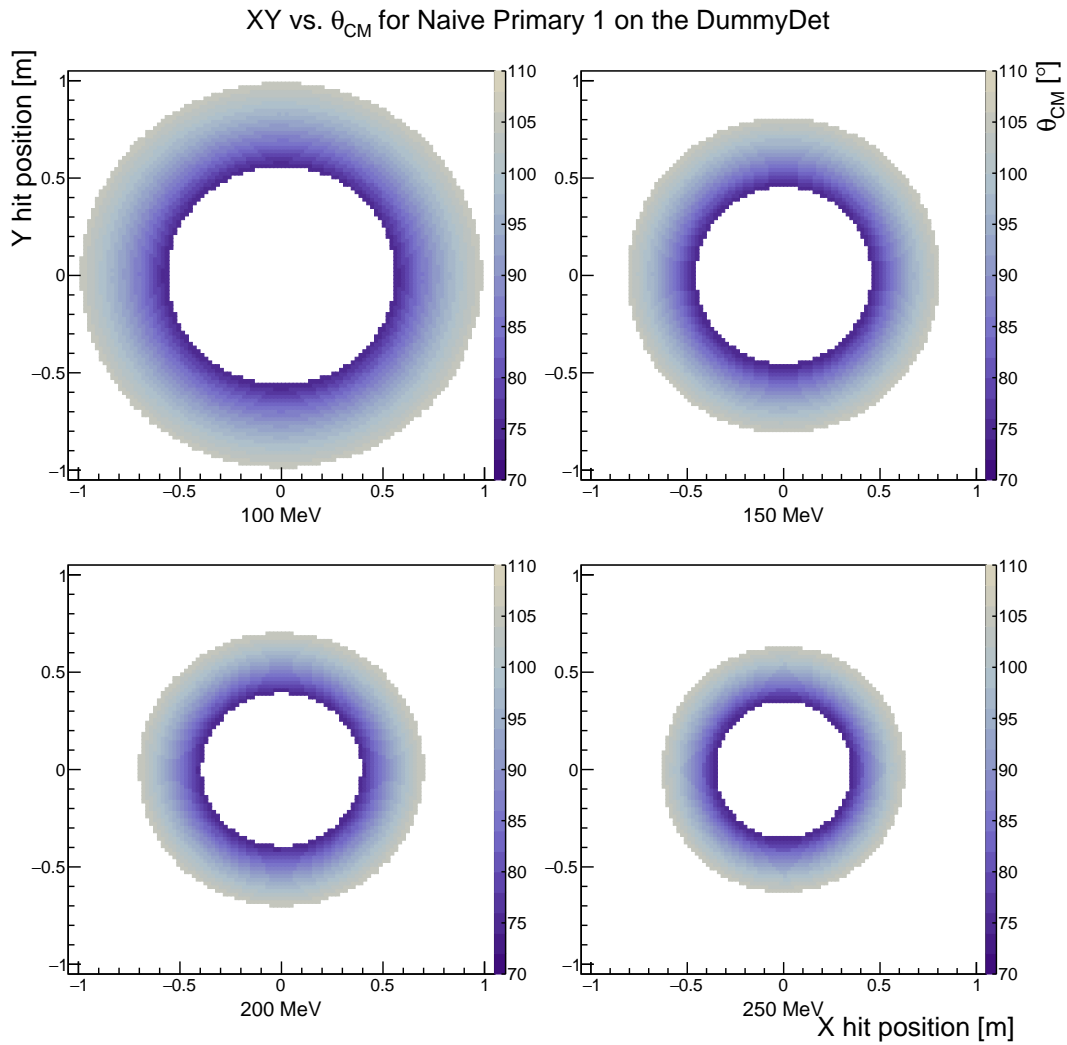


Figure 8.5: The θ_{CM} distribution on the face of DummyDet for naïve primary hits from primary electron 1 for various beam energies similar to MAMI. Here the horizontal axis is the X hit position (−1 m to 1 m), vertical axis is the Y hit position (−1 m to 1 m), and color axis is the θ_{CM} angle (70° to 110°).

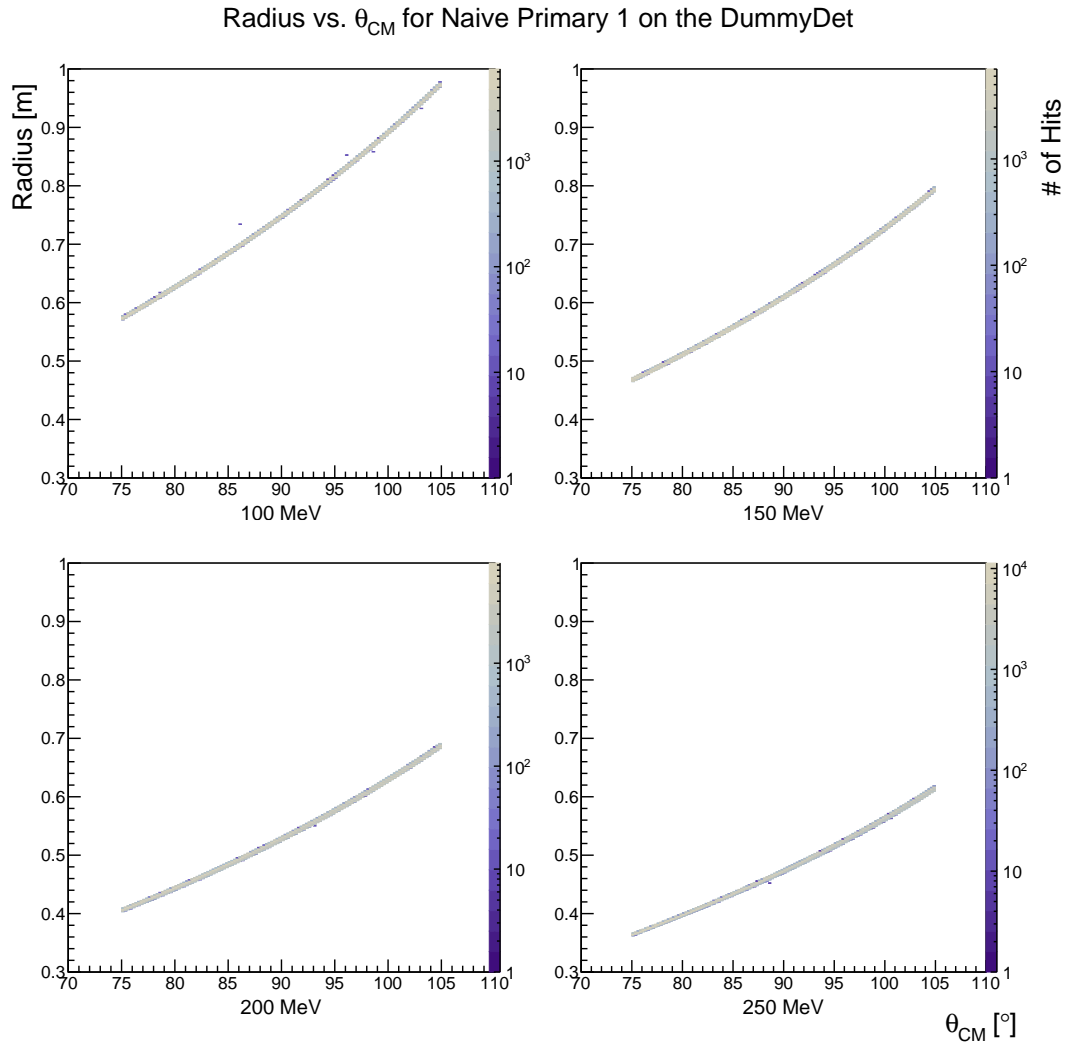


Figure 8.6: The radius of the distribution on the face of DummyDet for naïve primary hits from primary electron 1 for various beam energies similar to MAMI, vs. θ_{CM} . Here the horizontal axis is θ_{CM} angle (70° to 110°), vertical axis is the radius (0.3 m to 1.0 m), and the color axis is the relative number of hits.

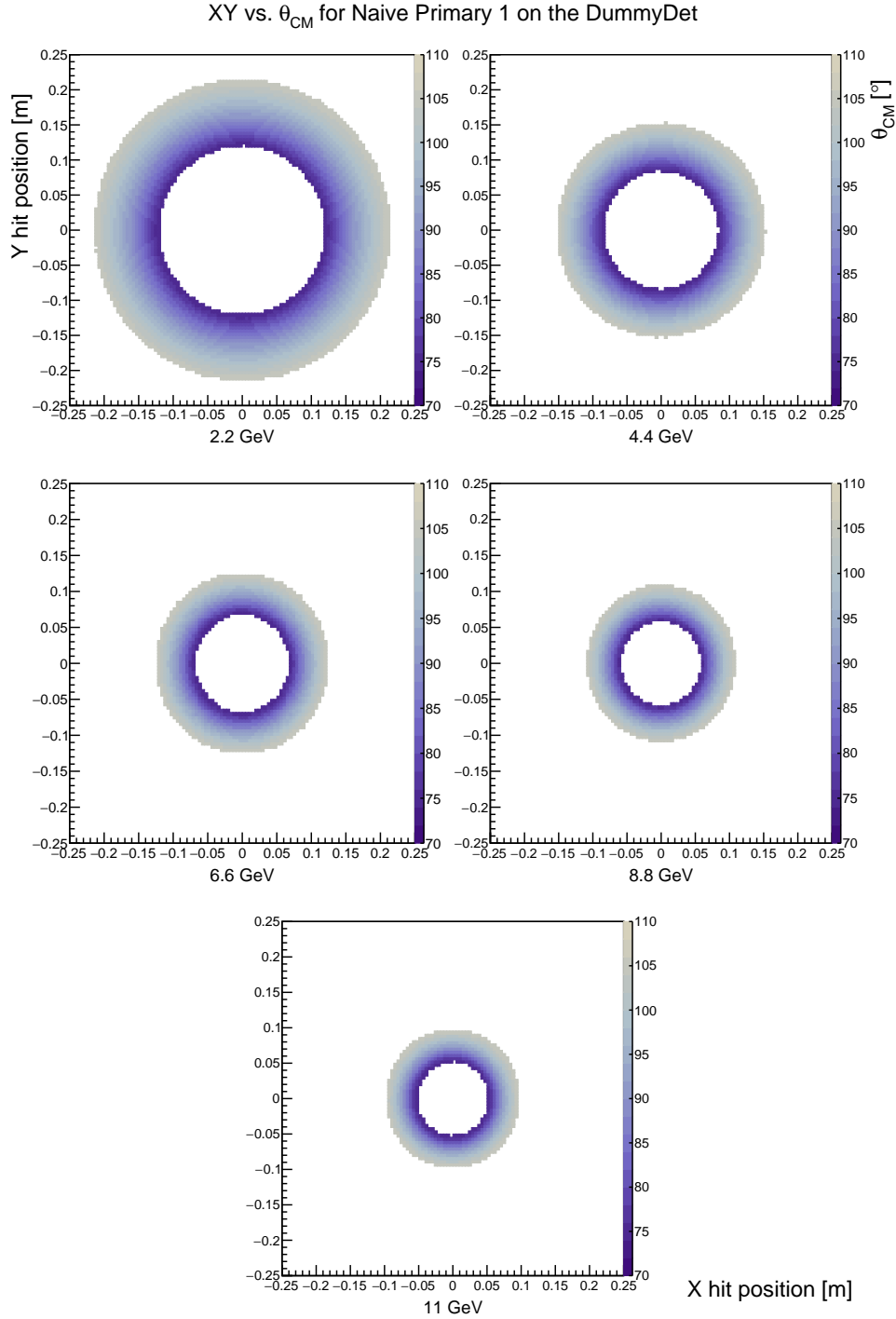


Figure 8.7: The θ_{CM} distribution on the face of DummyDet for naïve primary hits from primary electron 1 for various beam energies similar to JLab, from left to right and top to bottom 2.2 GeV, 4.4 GeV, 6.6 GeV, 8.8 GeV, and 11.0 GeV. Here the horizontal axis is the X hit position (-0.25 m to 0.25 m), vertical axis is the Y hit position (-0.25 m to 0.25 m), and color axis is the θ_{CM} angle (70° to 110°).

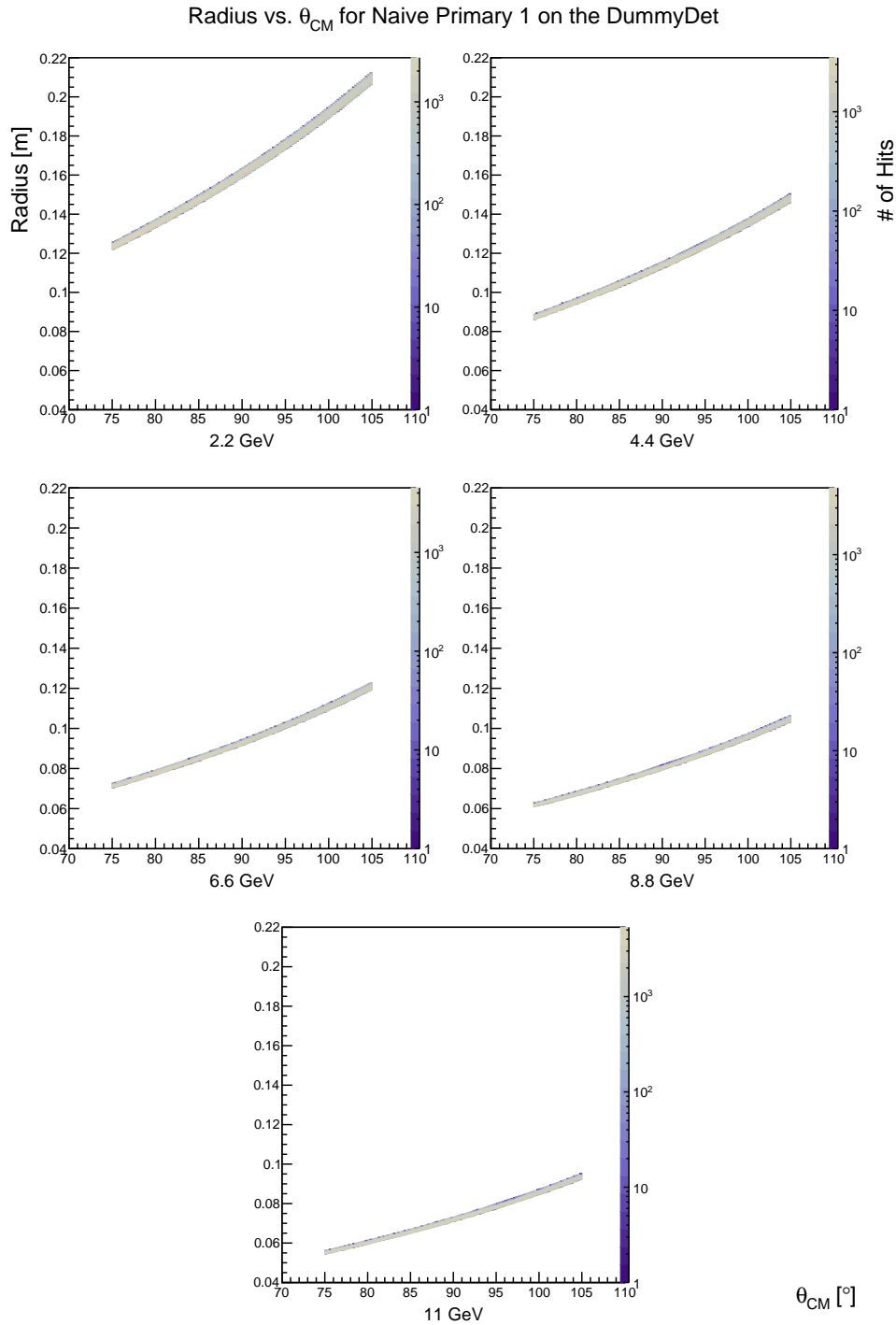


Figure 8.8: The radius of the distribution on the face of DummyDet for naïve primary hits from primary electron 1 for various beam energies similar to JLab, vs. θ_{CM} . Here the horizontal axis is θ_{CM} angle (70° to 110°), vertical axis is the radius (0.04 m to 0.22 m), and the color axis is the relative number of hits.

8.2.1.1 θ_{CM} Distribution

Due to the range of θ_{CM} and ϕ_{CM} that the simulated events are thrown over, it is expected that on the plane of DummyDet the naïve primaries will be distributed in a circle with a hole in the center, or a donut. Figures 8.5 and 8.7 illustrate this for naïve primary hits from primary electron 1; the inside of the donut has the smaller θ_{CM} angles which increase towards the outer part of the donut. This observation also shows that A_{zz} is independent of E_B , as seen in Eq. 6.4 in the center of mass frame, as the θ_{CM} distribution for the naïve primaries on the DummyDet will not change as the beam energy changes.

However, once boosted into the lab frame, the angular dependence (θ_{Lab}) of A_{zz} becomes dependent on the E_B (see Appendix C.1). Thus for a given θ_{CM} the radius of where the primary electron lands on the face of the DummyDet will change due to E_B ; this is illustrated in Figs. 8.5 and 8.7, and is most easily seen in Figs. 8.6 and 8.8, for naïve primary hits from primary electron 1.

8.2.2 Hall A Magnetic Optics

Multiple simulations were run to investigate how the Hall A magnetic optics would work with the solenoid magnetic field required for the HMolPol target. A beam energy of 11 GeV was chosen because it is the beam energy of interest for the proposed MOLLER experiment [80]. For these simulations the angle range in ϕ_{CM} was changed to -5° to 5° ; this corresponds to the angle range that the Fe Hall A Møller polarimeter detects, as noted in the Hydro-Møller proposal [1, 2].

As explained in Sec. 8.1.1, HMolPol randomly chooses the scattering angles for the primary electron 1 and then calculates the scattering angles for primary electron 2. These simulations have a small ϕ_{CM} angle range that is generated for primary electron 1, causing hits on DummyDet in the $+\hat{x}$ direction, while primary electron 2 will cause hits in the $-\hat{x}$ direction. Because of this, both of the primaries must be looked at in this case to get the full distribution of hits on DummyDet, unlike in Sec. 8.2.1.

For these simulations four separate configurations of magnetic optics were considered. For all of these configurations, the dipole was always off. The H target and the quadrupoles are varied between being on and off as described in Table 8.4. The four quadrupoles were set to “nominal” values for $E_B = 11$ GeV; these were -5.79 kG, -5.79 kG, 3.39 kG, and 5.79 kG for quadrupoles 1 through 4, respectively; these were found using Fig. 8.9 [107].

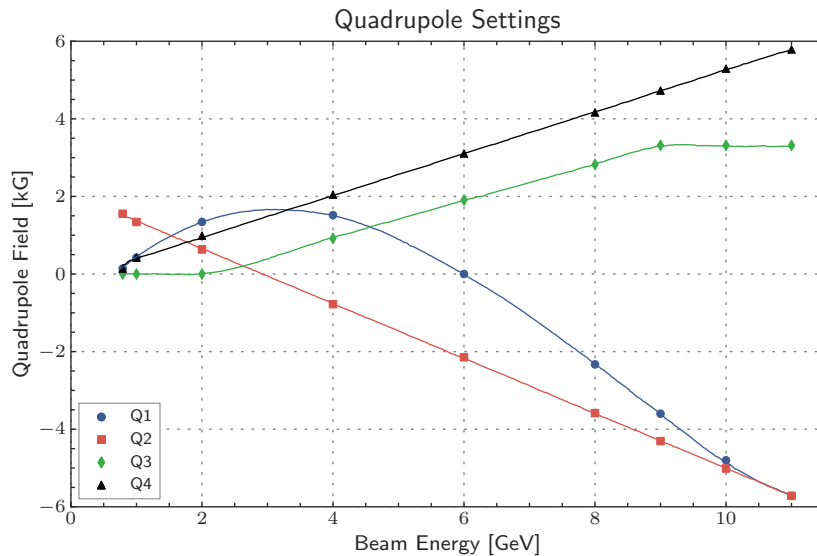


Figure 8.9: Hall A Møller polarimeter’s quadrupoles settings. Reproduced from [107].

Configuration	Magnetic Field		
	H Target	Quadrupoles	Dipole
1	Off	Off	Off
2	Off	On	Off
3	On	Off	Off
4	On	On	Off

Table 8.4: The status of magnetic fields for the Hall A magnetic optic simulations. For the H target “on“ is 8.0 T, and for the four Hall A quads “on” is the nominal values.

8.2.2.1 θ_{CM} Distribution

Configuration 1 doesn’t have any magnetic fields in the simulation, therefore the electrons travel straight to the dummy detector without any change in direction.

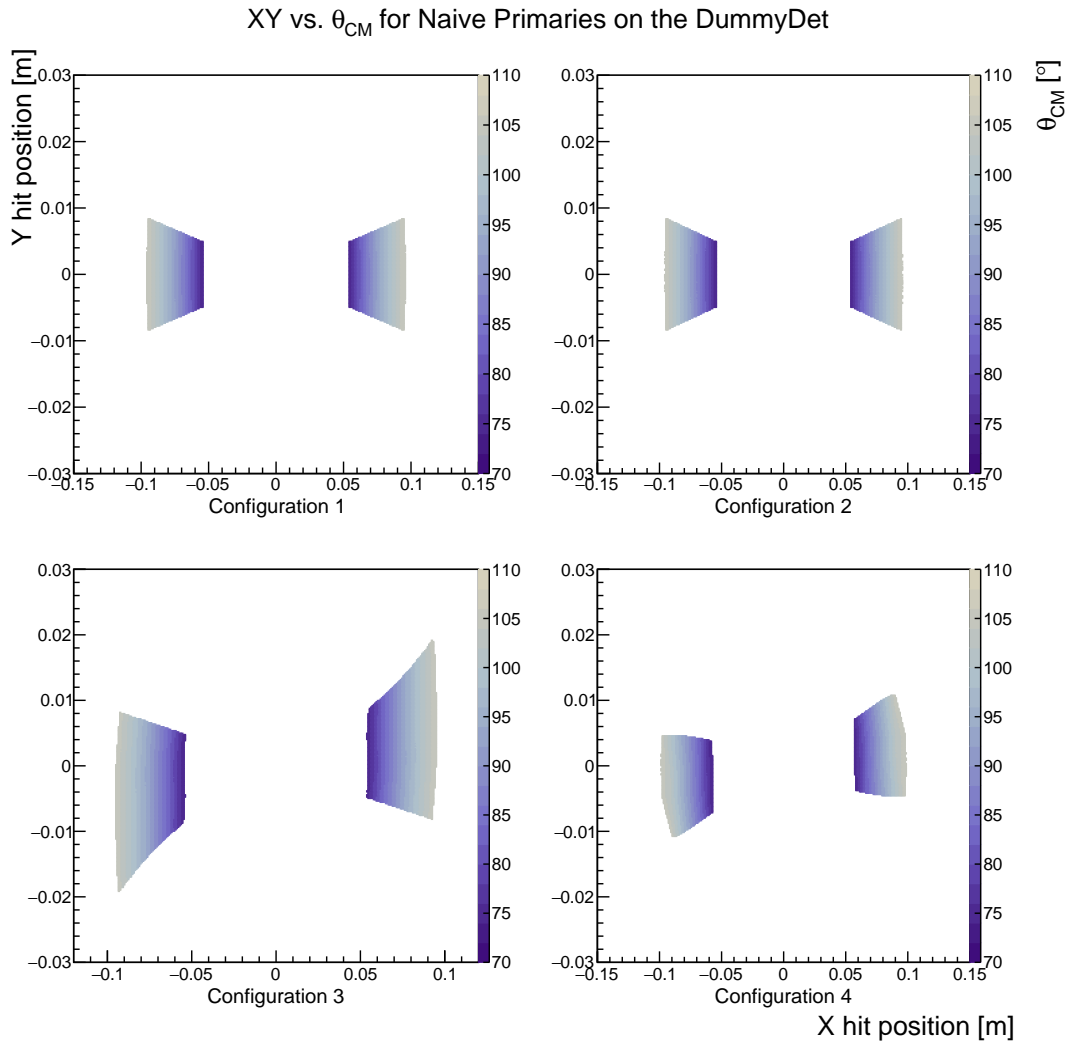


Figure 8.10: The θ_{CM} distribution on the face of the DummyDet naïve primaries coincidence hits, for Møller electrons generated over -5° to 5° for the 4 different magnetic configurations. Here the horizontal axis is the X hit position (-0.15 m to 0.15 m), vertical axis is the Y hit position (-0.03 m to 0.03 m), and color axis is the θ_{CM} angle (70° to 110°).

This is considered the baseline configuration, and should show two symmetric parts of the donut seen in Sec. 8.2.1.1. However, there is no expectation that the other configurations will lead to the same distribution. This distribution, is symmetric (see Fig. 8.10) given the symmetric range in θ_{CM} and ϕ_{CM} that events are generated over.

Configuration 2 only includes the set of four quadrupole magnets. Since quadrupoles focus along one axis while defocusing in the other, the quadrupoles are set up such that, for each pair, the scattered electrons are focused. Due to the focusing effects of the quadrupoles it is expected that there would be little difference between this and the first configuration. The results for configuration 2 can be seen in Fig. 8.10.

Configuration 3 only contains the target solenoid magnetic field. When a charged particle travels through the magnetic field, if it has a component that is perpendicular to the field lines, the particle will spiral around the field lines. The effect of the charged particles (in this case electrons) spiralling around the field lines will be expected to be some dispersion or “wings” in the detected distribution on the face of the DummyDet compared to configuration 1 (see Fig. 8.10). However this is not apparent in Figs. 8.5 and 8.7 because the range in ϕ_{CM} that is generated over is 0° to 360° , which covers up this effect. Since these are electrons and therefore are negatively charged, these “wings” will be on the top part of the $+\hat{x}$ distribution and on the bottom part of the $-\hat{x}$ half of the distribution².

Configuration 4 is the most realistic configuration because it has both the target solenoid field and the Hall A quadrupoles on. Compared to configuration 3 the effect of just the Hall A quadrupoles (*i.e.* Configuration 2) in the detected distribution on the face of the DummyDet, this change is most noticeable in the “wings” (see Fig. 8.10). Specifically, the “wings” are smaller here than in configuration 3, but in comparing this to configuration 1 or 2, it is seen that they are still present. The two parts of the distributions that didn’t have the “wings” in configuration 3, are different in the other configurations. In the $+\hat{x}$ distribution the “wing” on the top of the distribution is

²For a positively charged particle these “wings” be on the bottom part of the $+\hat{x}$ distribution and on the top part of the $-\hat{x}$ half of the distribution.

“squished” down towards the Y hit position, likewise on for “wing” on the bottom part of the $-\hat{x}$ distribution. Both of these effects cause the distribution to cover a smaller area on the DummyDet then in configuration 3.

Using these distributions some inferences about the design of possible detectors can be made. In the configurations 1 and 2, small symmetric detectors would be reasonable. However, for the other two configurations, especially configuration 3, small symmetric detectors may not be ideal. Larger detectors would be needed to account for the “wings” as they would change with E_B . The “wings” also may sway away from a simple detector geometry like a rectangle in favor of shape that is closer to a fraction of donut. Since the target solenoidal magnetic is a necessity, only configurations 3 and 4 are a realistic possibility. It is possible that one could farther improve the hit distribution for configuration 4 by optimizing the magnetic optics from the default Hall A design.

8.2.2.2 Radius vs. θ_{CM}

The radius of the hits for the various θ_{CM} angles gives another view on the θ_{CM} distribution on the DummyDet seen in Fig. 8.10. Here configurations 1, 2, and 3 have the same distribution as seen in Fig. 8.11. In these instances the minimum radius, $r_{min} \approx 0.054$ m and maximum radius, $r_{max} \approx 0.097$ m leads to a difference of $\Delta r \approx 0.043$ m. Also each for θ_{CM} there is a constant range of radii over which that θ_{CM} will be on the detector.

However, configuration 4 is different in a few ways from the other configurations. The minimum and maximum radii are larger then in the previous configurations. For this configuration $r_{min} \approx 0.057$ m and $r_{max} \approx 0.098$ m, which yields a decrease $\Delta r \approx 0.041$ m. Also seen in this configuration, especially at large θ_{CM} , there is a larger range of radii at each given θ_{CM} . This follows on what was seen in Fig. 8.10, the “squishing” of the “wings”.

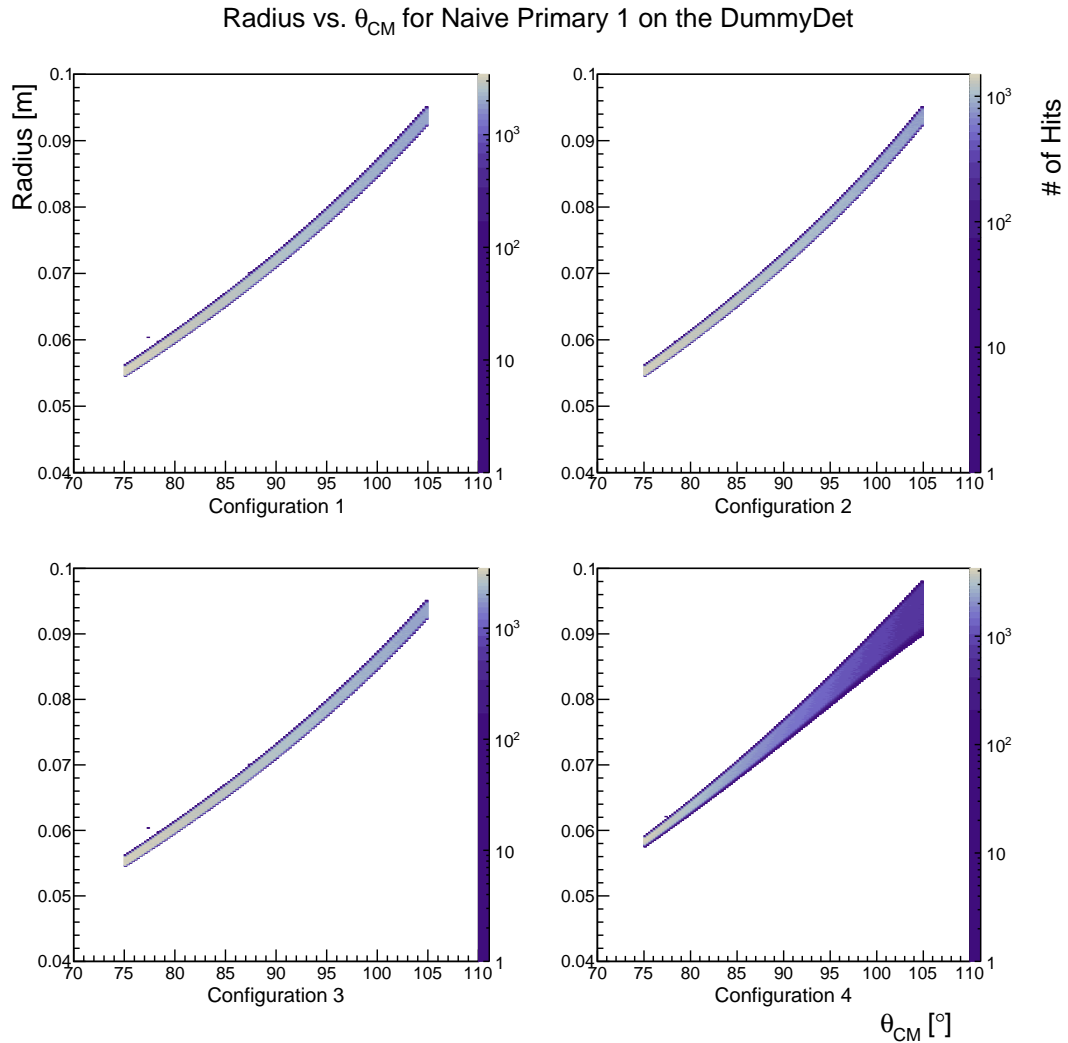


Figure 8.11: The radius vs. θ_{CM} distribution of naïve primaries coincidence hits, for Møller electrons generated over -5° to 5° for the 4 different magnetic configurations. Here the horizontal axis is θ_{CM} angle (70° to 110°), vertical axis is the radius (0.4 m to 1.0 m).

8.2.2.3 ϕ Angle Rotation

As explained in Secs. 8.1.1, the two primaries are 180° apart in ϕ_{CM} . When the interaction takes place within a magnetic field, specifically a solenoid, the primary electrons will rotate around the magnetic field lines. This causes them to reach the detector with a separation ϕ_{Lab} that is not always going to be 180° . However, if $\theta_{CM} = 90^\circ$ then regardless of where the interaction takes place in the target's solenoid the separation in ϕ_{Lab} for the two primary electrons will be 180° .

This separation between the two primary electrons on the face of the DummyDet $\zeta = \phi_{Lab_1} - \phi_{Lab_2}$, provides more information on the “wings” that are seen in Fig. 8.10. Figure 8.12 shows the relationship between ζ of the two primary electrons and θ_{CM} for each configuration. In configurations 1 and 2, where the target solenoid field is off, ζ is always 180° . Taking configuration 2 where the quadrupoles are on and comparing it to configuration 1 where there are no magnetic fields, shows again the cancellation effect each pair of quadrupoles has.

In configuration 3, the “wings” seen in Fig. 8.10 are more apparent. For $\theta_{CM} = 90^\circ$ case, $\zeta = 180^\circ$ is always expected, where for other values of θ_{CM} , however, ζ varies. When $\theta_{CM} < 90^\circ$, the minimum difference in the ϕ_{Lab} is $\zeta_{min} \approx 177.2^\circ$ and maximum is $\zeta_{max} = 180^\circ$ with an overall range of $\Delta\zeta = 2.8^\circ$. When $\theta_{CM} > 90^\circ$, the minimum is $\zeta_{min} \approx 180^\circ$ and maximum is $\zeta_{max} \approx 182.8^\circ$ with an overall range of $\Delta\zeta = 2.8^\circ$. Considering the entire θ_{CM} range, the separation between the two primary electrons varies over a range of $\Delta\zeta_{Tot} \approx 5.6^\circ$.

In configuration 4, like configuration 3 when $\theta_{CM} = 90^\circ$, $\zeta = 180^\circ$, always as expected, where for other values of θ_{CM} , however, ζ varies. However, unlike in configuration 3, this rotation is not just in one direction for either $\theta_{CM} < 90^\circ$ or $\theta_{CM} > 90^\circ$, but in both. Here when $\theta_{CM} < 90^\circ$, the minimum is $\zeta_{min} \approx 178.4^\circ$ and maximum is $\zeta_{max} \approx 181^\circ$ with an overall range of $\Delta\zeta = 2.6^\circ$. When $\theta_{CM} > 90^\circ$, the minimum is $\zeta_{min} \approx 179.2^\circ$ and maximum is $\zeta_{max} \approx 181.8^\circ$ with an overall range of $\Delta\zeta \approx 2.6^\circ$. Then the overall range over which the angle is rotated is therefore,

$\Delta\zeta_{Tot} \approx 3.4^\circ$. In this configuration, $\Delta\zeta_{Tot}$ has improved (*i.e.* reduced) 2.2° from configuration 3, therefore the quadrupoles serve to mitigate the effect of the solenoid on the angle range generated for these simulations.

8.3 Next Stages in HMolPol Development

Section 8.2.1.1 shows that for the energies used in these simulations, the scattered electrons have a maximum radius of less than 1 m at 7.47 m from the center of the target, which decreases as the E_B increases, as seen in Figs. 8.5 and 8.7. The hits are distributed evenly as seen in Figs. 8.6 and 8.8, leading to a detector design of a donut shape surrounding the beamline. In practice, however, this introduces other issues including: this can lead to problems with the experiment the Hydro-Møller is used for and other beamline components, an increase in backgrounds, and dimension issues with the needed detector inner radius being the size of the beamline.

How the target solenoid and the JLab Hall A quadrupoles influence the distribution of hits on the DummyDet is presented in Sec. 8.2.2. It is clear that the Hall A quads do help make the area of the distribution of the hits on the detector smaller, which is encouraging from a practical perspective. Using a coincidence detector system would help with reducing backgrounds, but with the H target there is a range in the difference in ϕ_{Lab} angles over which the hits can be apart. Unlike in the simulations, in reality there is no restriction in the angles which the Møller interactions take place, and since there is a range in the difference in ϕ_{Lab} angles over which the hits can be apart, a segmented coincidence detector may be the best choice to make sure the events detected are true coincidences. Simulation will be needed to look at various possible designs like this, and to help select the materials of any detector system.

Future JLab Hall A simulations need to be done to compare the Fe Møller polarimeter with the HMolPol geometry for the Hydro-Møller, which can be accomplished by switching the H target with the solenoid out for the Fe target. Comparing this with Configuration 2 will allow one to see if any differences arise due to the target material.

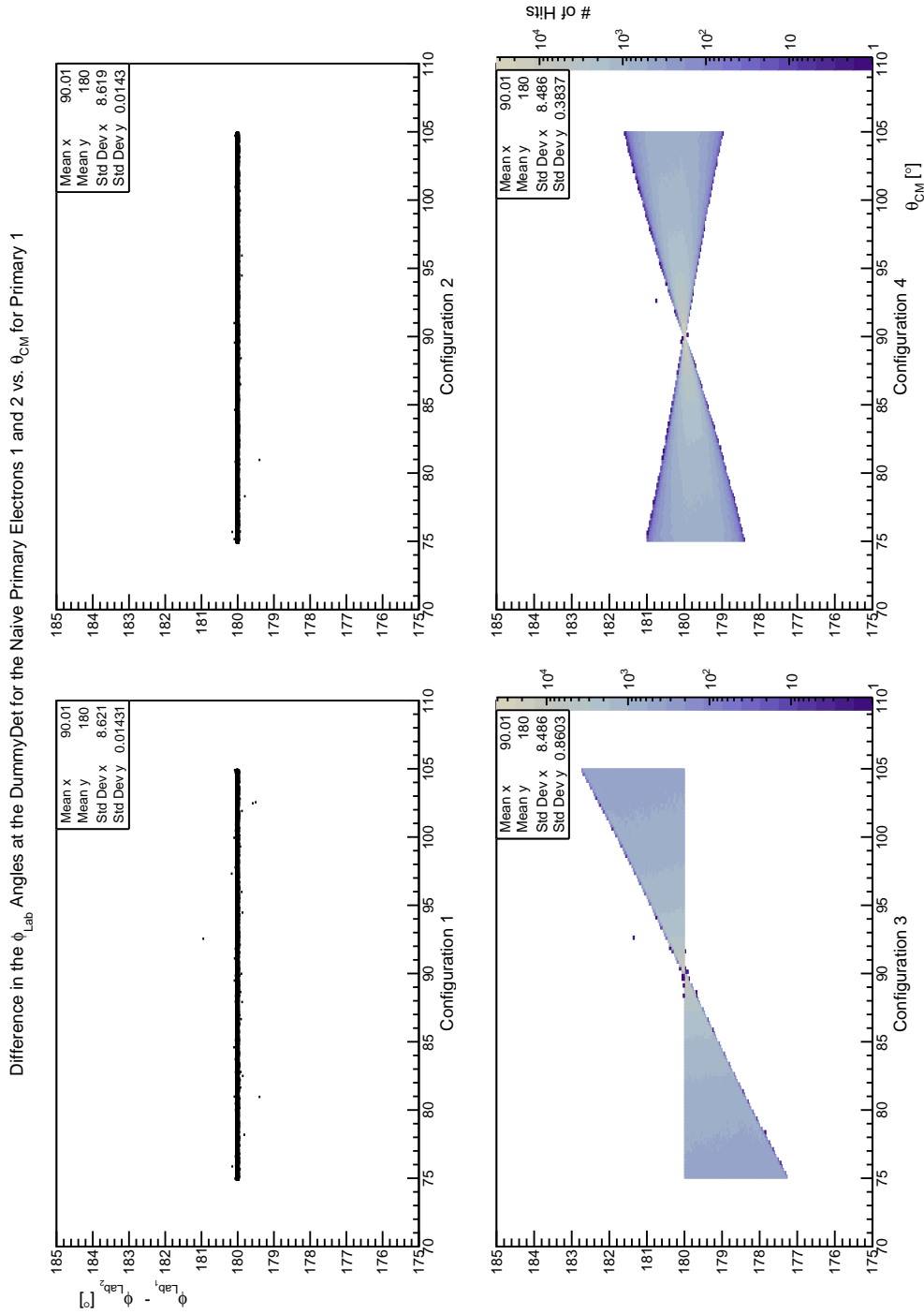


Figure 8.12: The ϕ_{Lab} hit difference in primary 1 and 2, ζ , vs. θ_{CM} distribution on the face of the DummyDet naive primaries from primary 1, for Møller electrons generated over -5° to 5° for the 4 different magnetic configurations. Here the x-axis is θ_{CM} angle (70° to 110°), y-axis is ζ (175° to 185°).

Changing the strengths of the quadrupoles to match any differences between what was used in these simulations and the actual values at 11 GeV, along with other beam energies, will require more simulations. Simulations should be done to investigate if these quadrupole's strengths are the ideal ones to use with the Hall A geometry or if the event distribution on the detectors improves with different values.

In Sec. 8.2.2 the only magnetic of the Hall A magnetic optics that was not included is the dipole; simulations will have to be done with this magnetic field on. The dipole will primarily bend the electrons down away from the beamline, but will also cause spreading based on the electron's energy. One other aspect of the all the magnetic fields (target and Hall A optics) that is not included is their fringe fields. The effect of these on the hit distribution on the detector will have to be investigated, as this can have impact on any detector design.

Future simulations will also have to be done looking to see if there is any change to the distribution with a target that has more accurate density and magnetic field strengths of the target as seen in Fig. 8.1.

The majority of simulations in this dissertation concentrate only on the present JLab Hall A Fe Møller polarimeter, however HMolPol was specifically designed such that it can easily be adapted to other places like MAMI though changing of the geometry, magnets, and detectors along with targets, both H or different material. MAMI and other labs will have to run simulations to investigate their Møller polarimeter system.

All of the simulations have been done with the DummyDet, and as stated in Sec. 8.1.3 and 8.1.4 the other type of detector geometry LeftRightDet is already in HMolPol which can be implemented. This detector geometry will need to be investigated, in a similar way to the initial studies in this dissertation, and in follow up studies that have been laid out in this section.

Other studies that are needed include: how the target solenoid impacts the electron beam transport and beam spot size, the effect of backgrounds such as Mott Scattering and scattering from the beam pipe and other materials, and what the critical apertures are in the magnetic optics.

Chapter 9

Conclusion

The Q_{weak} experiment made a measurement of Q_{W}^{P} at a $Q^2 = 24.8 \pm 0.1 \text{ m}(\text{GeV}^2)$. It measured Q_{W}^{P} to be 0.0719 ± 0.0045 which agrees with the prediction of the Standard Model of particle physics. This result sets a lower limit of 7.5 TeV for Λ_+/g , where g is coupling and Λ is the mass of a hypothetical particle exchanged in ep scattering not in the Standard Model.

An efficient modular Monte Carlo was developed for Møller polarimeters, HMolPol. Using HMolPol, initial feasibility studies for a novel Atomic Hydrogen Møller Polarimeter, Hydro-Møller, were done.

Appendix A

Q^2 Derivation

A.1 Q^2 Derivation

The four-momentum transfer¹, $Q^2 = -q^2$, for scattering of an electron off of a proton is shown in Fig. A.1.

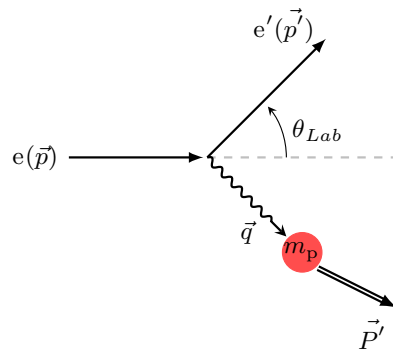


Figure A.1: An electron scattering off a proton. The electron comes in from the left with a momentum of \vec{p} , scattering off the stationary proton in red with a mass m_p , at an angle θ_{Lab} with a final momentum of \vec{p}' .

The relationship between the initial and final proton momentum, the electron's

¹In fixed-target scattering experiments, Q^2 is used rather than q^2 , because Q^2 is always a positive quantity.

initial and final momentum, and the momentum transfer are as follows:

$$P' = P + q = m_p + q \quad (\text{A.1a})$$

$$p = q + p' \quad (\text{A.1b})$$

$$q = p - p', \quad (\text{A.1c})$$

where p is the four-momentum of the incoming electron, p' is the four-momentum of the outgoing electron, P is the four-momentum of the proton initially or m_p as it is at rest, P' is the final four-momentum of the proton, and q is the four-momentum transferred from the electron to the proton.

Then using $p^2 = p'^2 = m_e^2$, q^2 can be determined as

$$\begin{aligned} q^2 &= (p - p')^2 \\ &= p^2 + p'^2 - 2p \cdot p' \\ &= m_e^2 + m_e^2 - 2\vec{p} \cdot \vec{p}' \\ &= 2m_e^2 - 2p \cdot p' \\ &= 2m_e^2 - 2 \left[(T + m_e)(T + m_e) - \vec{p} \cdot \vec{p}' \right] \\ &= 2m_e^2 - 2 \left[TT' + m_e^2 + m_e(T + T') - \vec{p} \cdot \vec{p}' \right] \\ &= 2 \left[\vec{p} \cdot \vec{p}' - TT' - m_e(T + T') \right], \end{aligned} \quad (\text{A.2})$$

where the kinetic energy, T and T' are defined by $p_0 = T + m_e$ and $p'_0 = T' + m_e$ respectively.

Since, $\vec{p} \cdot \vec{p}' = |\vec{p}| |\vec{p}'| \cos \theta_{Lab}$, Q^2 is

$$Q^2 = -2 \left[|\vec{p}| \cdot |\vec{p}'| \cos \theta_{Lab} - TT' - m_e(T + T') \right] \quad (\text{A.3})$$

Finally, T' can be found through using the recoil factor of the proton, η by through the following,

$$T' = \frac{T}{\eta} \quad (\text{A.4})$$

where,

$$\eta = 1 + 2 \frac{T}{m_p} \sin^2 \left(\frac{\theta_{Lab}}{2} \right). \quad (\text{A.5})$$

A.2 Q^2 Derivation: Relativistic Limit

Taking the relativistic limit, one can simplify Q^2 from Eq. A.2 into the more recognizable forms seen in Eq. A.23. For the Q_{weak} experiment $E = 1159.65 \text{ MeV} \gg m_e$, therefore the electron mass is negligible, this means that $p_0 = T + m_e \approx E$ and $p'_0 = T' + m_e \approx E'$ the incoming and outgoing electron energy respectively. This means the last term in Eq. A.2 can be neglected, therefore

$$Q^2 \approx 2 \left(EE' - \vec{p} \cdot \vec{p}' \right). \quad (\text{A.6})$$

Likewise, $\vec{p} \cdot \vec{p}'$ can be simplified,

$$\begin{aligned} p^2 &= m_e^2 \\ &= 0 \\ &= (E, \vec{p})^2 \\ &= E^2 - |\vec{p}|^2 \end{aligned} \quad (\text{A.7})$$

finally,

$$|\vec{p}|^2 = E^2 \quad (\text{A.8})$$

by the same reasoning,

$$|\vec{p}'|^2 = E'^2. \quad (\text{A.9})$$

Finally by combining Eqs. A.8 and A.9,

$$\begin{aligned} \vec{p} \cdot \vec{p}' &= |\vec{p}|^2 \cdot |\vec{p}'|^2 \cos \theta_{Lab} \\ &= EE' \cos \theta_{Lab}. \end{aligned} \quad (\text{A.10})$$

Finally, using Eqs. A.6 and A.10, Q^2 becomes:

$$Q^2 = 2EE'(1 - \cos \theta_{Lab}) \quad (\text{A.11a})$$

$$= 4EE' \sin^2 \left(\frac{\theta_{Lab}}{2} \right). \quad (\text{A.11b})$$

A.3 Q^2 Elastic Scattering in the Relativistic Limit

It can be useful to write Q^2 in terms of only one of the energy variables. By using Bjorken scaling variable, x and ν this can be achieved.

By using Eqs. A.1c, A.7 and A.9, the energy that is transferred to the proton, ν is

$$\nu = E - E'. \quad (\text{A.12})$$

Also the initial and final four-momentum, of the proton is as follows:

$$P = (m_p, \vec{0}) \quad (\text{A.13a})$$

$$P' = (m_p + \nu, \vec{P}') \quad (\text{A.13b})$$

Bjorken x is defined as

$$\begin{aligned} x &\equiv \frac{-q^2}{2P \cdot q} \\ &= \frac{Q^2}{2P \cdot q}. \end{aligned} \quad (\text{A.14})$$

Using Eqs. A.1c, A.7, A.9 and A.13a, $P \cdot q$ is

$$\begin{aligned} P \cdot q &= (m_p, \vec{0}) \cdot (p - p') \\ &= m_p (p_0 - p'_0) \\ &= m_p (E - E'). \end{aligned} \quad (\text{A.15})$$

It follows that Bjorken x becomes

$$\begin{aligned} x &= \frac{Q^2}{2P \cdot q} \\ &= \frac{Q^2}{2m_p (E - E')} \\ &= \frac{Q^2}{2m_p \nu}. \end{aligned} \tag{A.16}$$

For elastic scattering $x = 1$, or

$$1 = \frac{Q^2}{2m_p \nu}. \tag{A.17}$$

Then Q^2 can also be written as

$$\begin{aligned} Q^2 &= 2m_p \nu \\ &= 2m_p (E - E'). \end{aligned} \tag{A.18}$$

Therefore for elastic scattering Q^2 can be written independent of θ_{Lab} as

$$Q^2 = 2m_p (E - E'). \tag{A.19}$$

Using Eq. A.19, the electron's energy, E and E' can be determined:

$$E' = E - \frac{Q^2}{2m_p} \tag{A.20a}$$

$$E = E' + \frac{Q^2}{2m_p} \tag{A.20b}$$

Finally using Eqs. A.11a and A.20,

$$\begin{aligned} Q^2 &= 2EE'(1 - \cos \theta_{Lab}) \\ &= 2E \left(E - \frac{Q^2}{2m_p} \right) (1 - \cos \theta_{Lab}) \\ &= \left(2E^2 - \frac{EQ^2}{m_p} \right) (1 - \cos \theta_{Lab}). \end{aligned} \tag{A.21}$$

Then Q^2 for elastic scattering can found independently of E' ,

$$Q^2 = 2E^2 \frac{(1 - \cos \theta_{Lab})}{1 + \frac{E}{m_p} (1 - \cos \theta_{Lab})}.$$

Similarly, Q^2 for elastic scattering can found independently of E ,

$$Q^2 = 2E'^2 \frac{(1 - \cos \theta_{Lab})}{1 - \frac{E'}{m_p} (1 - \cos \theta_{Lab})}. \quad (\text{A.22})$$

Therefore, there are 4 equivalent expressions for Q^2 , one that is true all the time, Eq. A.11 and three that are valid only for elastic scattering, Eqs. 4.1, A.18 and A.22, which are summarized in Eq. A.23.

$$\begin{aligned} Q^2 &= 2EE'(1 - \cos \theta_{Lab}) \\ Q^2 &= 2m_p(E - E') \\ Q^2 &= 2E^2 \frac{(1 - \cos \theta_{Lab})}{1 + \frac{E}{m_p} (1 - \cos \theta_{Lab})} \\ Q^2 &= 2E'^2 \frac{(1 - \cos \theta_{Lab})}{1 - \frac{E'}{m_p} (1 - \cos \theta_{Lab})} \end{aligned} \quad (\text{A.23})$$

Appendix B

Eigenstates and Energies of Atomic Hydrogen

In Sec. 7.2, the Hamiltonian, \mathcal{H} , for a hydrogen atom in an external magnetic field, \vec{B} is given in Eq. 7.1,

$$\mathcal{H} = A\hat{i} \cdot \hat{s} + g_e\mu_B\vec{B} \cdot \hat{s} + g_p\mu_N\vec{B} \cdot \hat{i}.$$

Since the magnetic field and the electron (\hat{s}) and proton (\hat{i}) spins are both in the \hat{z} direction, this can be rewritten with raising and lowering operators for the spin operators as

$$\mathcal{H} = A\left(\frac{i_+s_- + i_-s_+}{2} + i_zs_z\right) + g_e\mu_B Bs_z + g_p\mu_N Bi_z. \quad (\text{B.1})$$

Using the good quantum numbers for this system, the total spin of the atom and Clebsch-Gordon coefficients, the eigenvectors of the system can be found; they are,

$$\begin{aligned}
 |0\ 0\rangle &= \frac{1}{\sqrt{2}} (|\uparrow\downarrow\rangle - |\downarrow\uparrow\rangle), \\
 |1\ -1\rangle &= |\downarrow\downarrow\rangle, \\
 |1\ 0\rangle &= \frac{1}{\sqrt{2}} (|\uparrow\downarrow\rangle + |\downarrow\uparrow\rangle), \\
 |1\ 1\rangle &= |\uparrow\uparrow\rangle.
 \end{aligned} \tag{B.2}$$

Here \uparrow and \downarrow are for the electron's spin, and \uparrow and \downarrow are the proton's spin. Solving this Hamiltonian is easiest through a matrix with a basis of $\{|\uparrow\uparrow\rangle, |\uparrow\downarrow\rangle, |\downarrow\uparrow\rangle, |\downarrow\downarrow\rangle\}$. By adopting this basis, the rewritten Hamiltonian can also be written as a matrix, with six nonzero elements. The zero elements are from the limits of the raising and lowering operators. This means all non-diagonal elements except for $\langle\downarrow\uparrow|\mathcal{H}|\uparrow\downarrow\rangle$ and $\langle\uparrow\downarrow|\mathcal{H}|\downarrow\uparrow\rangle$ are zero. The diagonal elements of the matrix will only have terms that contribute to it directly from terms that have the \hat{z} component of the spin. This gives a Hamiltonian matrix of,

$$\begin{pmatrix}
 \frac{A}{4} - \frac{B}{2}\mu_+ & 0 & 0 & 0 \\
 0 & -\frac{A}{4} - \frac{B}{2}\mu_- & \frac{A}{2} & 0 \\
 0 & \frac{A}{2} & -\frac{A}{4} + \frac{B}{2}\mu_- & 0 \\
 0 & 0 & 0 & \frac{A}{4} + \frac{B}{2}\mu_+
 \end{pmatrix}, \tag{B.3}$$

where μ_+ and μ_- are defined as $\mu_+ \equiv -g_e\mu_B + g_p\mu_N$ and $\mu_- \equiv -g_e\mu_B - g_p\mu_N$. This gives energies of

$$E(m_f) = -g_p\mu_N B m_f - \frac{A}{4} \pm \frac{A}{2} \sqrt{1 + 2m_f x + x^2}, \tag{B.4}$$

where m_f is the total spin of the system and $x \equiv \frac{-\mu_- B}{A}$. This means the energies for the eigenstate of the system are as follows:

Eigenstate	Energy	
$\frac{1}{\sqrt{2}}(\uparrow\downarrow\rangle - \downarrow\uparrow\rangle)$	$A \left(-1 - 2\sqrt{1 + \left(\frac{\mu_- B}{2A}\right)^2} \right)$. (B.5)
$ \downarrow\downarrow\rangle$	$A + \mu_+ B$	
$\frac{1}{\sqrt{2}}(\uparrow\downarrow\rangle + \downarrow\uparrow\rangle)$	$A \left(-1 + 2\sqrt{1 + \left(\frac{\mu_- B}{2A}\right)^2} \right)$	
$ \uparrow\uparrow\rangle$	$A - \mu_+ B$	

Appendix C

Analyzing Power for Møller Scattering

C.1 Lab Frame Analyzing Power Derivation

In the Center of Mass (CM) frame, the Møller reaction is shown in Fig. 6.2. The analyzing power (A_{zz}) of this reaction was shown in Eq. 6.4

$$A_{zz}(\theta_{CM}) = \frac{-\sin^2 \theta_{CM}(8 - \sin^2 \theta_{CM})}{(4 - \sin^2 \theta_{CM})^2}.$$

Figure 6.2 is a plot of how the A_{zz} changes with the center of mass scattering angle, θ_{CM} . The maximum analyzing power (A_{zz}^{max}) of $-7/9$ is at $\theta_{CM} = 90^\circ$. In the lab frame before the collision, the four momenta of the two particles are very well defined. The first electron comes in with the beam energy (E_B) and moves with momentum, p_L , and the second electron is at rest. In the initial state the four momentum for each electron then is:

$$\begin{aligned} 1 : (E_B, 0, 0, p_L) \\ 2 : (m_e, 0, 0, 0) \end{aligned} \tag{C.1}$$

with $p_L = \sqrt{E_B^2 - m_e^2}$. Then the Lorentz invariant is $E_{CM} = \sqrt{(E_1 + E_2)^2 - (\vec{p}_1 + \vec{p}_2)^2}$, where E_1 , E_2 , p_1 , and p_2 are the energies and momenta for the first and second electron respectively. For this situation the E_{CM} is

$$E_{CM} = \sqrt{2m_e^2 + 2E_B m_e}. \quad (\text{C.2})$$

The velocity of the CM in the lab frame is

$$\begin{aligned} \beta_{CM} &= \frac{p_L}{E_B + m_e} \\ &= \frac{\sqrt{E_B^2 - m_e^2}}{E_B + m_e}, \end{aligned} \quad (\text{C.3})$$

so it follows then that the γ_{CM} factor is

$$\gamma_{CM} = \frac{E_B + m_e}{\sqrt{2m_e^2 + 2E_B m_e}}. \quad (\text{C.4})$$

In the CM frame the four-momentum vectors are, where 1 and 2 denote the initial state and 3 and 4 are the final state,

$$\begin{aligned} 1: & \left(\frac{E_{CM}}{2}, 0, 0, \frac{p_{CM}}{2} \right) \\ 2: & \left(\frac{E_{CM}}{2}, 0, 0, -\frac{p_{CM}}{2} \right) \\ 3: & \left(\frac{E_{CM}}{2}, 0, \frac{p_{CM}}{2} \sin \theta_{CM} \cos \phi_3, \frac{p_{CM}}{2} \cos \theta_{CM} \right) \\ 4: & \left(\frac{E_{CM}}{2}, 0, \frac{p_{CM}}{2} \sin (\pi - \theta_{CM}) \cos \phi_4, \frac{p_{CM}}{2} \cos (\pi - \theta_{CM}) \right). \end{aligned} \quad (\text{C.5})$$

It follows then that the momentum in the CM frame is

$$p_{CM} = \sqrt{E_{CM}^2 - 4m_e^2}. \quad (\text{C.6})$$

The scattered electrons go off back to back to each other so $\phi_3 = 0$ and $\phi_4 = \pi$. The scattered particles' four momenta simplify to

$$\begin{aligned} 3: & \left(\frac{E_{CM}}{2}, 0, \frac{p_{CM}}{2} \sin \theta_{CM}, \frac{p_{CM}}{2} \cos \theta_{CM} \right) \\ 4: & \left(\frac{E_{CM}}{2}, 0, -\frac{p_{CM}}{2} \sin \theta_{CM}, -\frac{p_{CM}}{2} \cos \theta_{CM} \right). \end{aligned} \quad (C.7)$$

In the Lab frame the scattering is described in Fig. C.1. Boosting into the lab frame

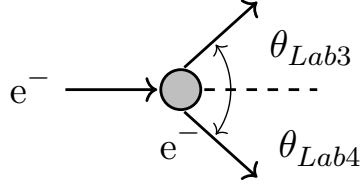


Figure C.1: Scattering electrons in the Lab frame.

gives:

$$\begin{aligned} 3: & \left(\gamma_{CM} \left[\frac{E_{CM}}{2} - \beta_{CM} \frac{p_{CM}}{2} \cos \theta_{CM} \right], 0, \right. \\ & \left. \frac{p_{CM}}{2} \sin \theta_{CM}, \gamma_{CM} \left[\frac{p_{CM}}{2} \cos \theta_{CM} - \beta_{CM} \frac{E_{CM}}{2} \right] \right) \\ 4: & \left(\gamma_{CM} \left[\frac{E_{CM}}{2} + \beta_{CM} \frac{p_{CM}}{2} \cos \theta_{CM} \right], 0, \right. \\ & \left. -\frac{p_{CM}}{2} \sin \theta_{CM}, \gamma_{CM} \left[-\frac{p_{CM}}{2} \cos \theta_{CM} - \beta_{CM} \frac{E_{CM}}{2} \right] \right) \end{aligned} \quad (C.8)$$

It follows then that the relationships between the θ_{Lab} and the θ_{CM} angles are:

$$\begin{aligned} \tan \theta_{Lab3} &= \frac{\frac{p_{CM}}{2} \sin \theta_{CM}}{\gamma_{CM} \left(\frac{p_{CM}}{2} \cos \theta_{CM} - \beta_{CM} \frac{E_{CM}}{2} \right)} \\ \tan \theta_{Lab4} &= \frac{-\frac{p_{CM}}{2} \sin \theta_{CM}}{\gamma_{CM} \left(-\frac{p_{CM}}{2} \cos \theta_{CM} - \beta_{CM} \frac{E_{CM}}{2} \right)} \end{aligned} \quad (C.9)$$

For A_{zz}^{max} , the angles become:

$$\begin{aligned}\tan \theta_{Lab3} &= -\frac{p_{CM}}{\gamma_{CM}\beta_{CM}E_{CM}} \\ \tan \theta_{Lab4} &= \frac{p_{CM}}{\gamma_{CM}\beta_{CM}E_{CM}}\end{aligned}\tag{C.10}$$

Figure C.2 is a graph of the A_{zz} as a function of θ_{Lab} for various beam energies. At the A_{zz}^{max} the electrons scatter at equal and opposite angles in the lab frame.

C.2 Energy Independence of the Analyzing Power

The relevant analyzing power, A_{zz} (beam and target both polarized in the $\hat{\mathbf{z}}$ direction) is energy independent, despite the fact that the cross-section for Møller scattering at tree level is energy dependent. This section will demonstrate this is true for the relativistic limit of the A_{zz} and provides the expression for the other analyzing powers where the beam and target are polarized in other combinations of directions. The total analyzing powers (A_{ij}) for a beam traveling in the $\hat{\mathbf{z}}$ direction, where $\hat{\mathbf{x}}$ is perpendicular to the plane of scatter, and $\hat{\mathbf{y}} = [\hat{\mathbf{x}} \times \hat{\mathbf{z}}]$ are:

$$A_{zz} = \tau(\xi, \theta_{CM}) [4\xi(2\xi - 1) - (\xi - 1)(\xi + 3) \sin^2 \theta_{CM}] \tag{C.11a}$$

$$A_{xx} = \tau(\xi, \theta_{CM}) [4\xi + (\xi - 1)(\xi + 3) \sin^2 \theta_{CM}] \tag{C.11b}$$

$$A_{yy} = \tau(\xi, \theta_{CM}) [4(2\xi - 1) - (\xi - 1)^2 \sin^2 \theta_{CM}] \tag{C.11c}$$

$$A_{zx} = A_{xz} = \tau(\xi, \theta_{CM})(\xi - 1)\sqrt{2(\xi + 1)} \sin 2\theta_{CM} \tag{C.11d}$$

$$A_{xy} = A_{yx} = A_{yz} = A_{zy} = 0 \tag{C.11e}$$

where

$$-\tau(\xi, \theta_{CM}) = \frac{\sin^2 \theta_{CM}}{4\xi^2(1 + 3 \cos^2 \theta_{CM}) + (\xi - 1)^2(4 + \sin^2 \theta_{CM}) \sin^2 \theta_{CM}} \tag{C.11f}$$

and where θ_{CM} is the center of mass scattering angle, and following the notation in the literature $\xi = E_B/m_e = \gamma$ is the energy of the incident electron normalized to the

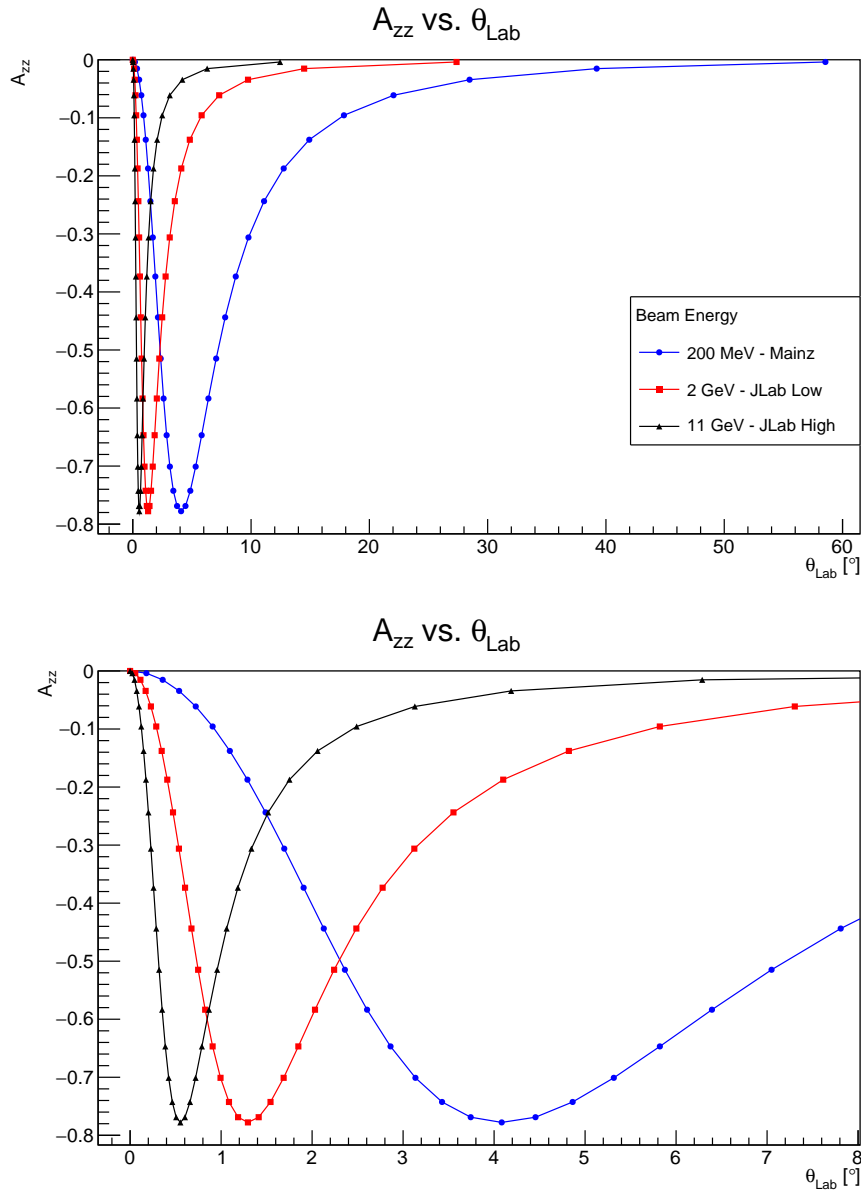


Figure C.2: Møller scattering analyzing power vs. θ_{Lab} . A_{zz} is shown for various beam energies appropriate for Jefferson Lab and for the MAMI accelerator at the Johannes Gutenberg University, Mainz. The beam energies shown are 200 MeV in blue circles, 2 GeV in red square, 11 GeV in black triangle.

mass of the electron [108]. For the relativistic limit $\xi \gg 1$ all factors to the order of ξ^2 or higher are negligible. Therefore Eqs. C.11 become:

$$A_{zz} = \tau(\xi, \theta_{CM}) \xi^2 (8 - \sin^2 \theta_{CM}) \quad (\text{C.12a})$$

$$A_{xx} = \tau(\xi, \theta_{CM}) \xi^2 \sin^2 \theta_{CM} \quad (\text{C.12b})$$

$$A_{yy} = \tau(\xi, \theta_{CM}) - \xi^2 \sin^2 \theta_{CM} \quad (\text{C.12c})$$

$$A_{zx} = A_{xz} = \tau(\xi, \theta_{CM}) 2\xi \sin \theta_{CM} \cos \theta_{CM} \quad (\text{C.12d})$$

$$A_{xy} = A_{yx} = A_{yz} = A_{zy} = 0 \quad (\text{C.12e})$$

where

$$-\tau(\xi, \theta_{CM}) = \frac{-\sin^2 \theta_{CM}}{\xi^2 (4 - \sin^2 \theta_{CM})^2} \quad (\text{C.12f})$$

Finally switching back to γ , these can be simplified to:

$$A_{zz} = \frac{-\sin^2 \theta_{CM} (8 - \sin^2 \theta_{CM})}{(4 - \sin^2 \theta_{CM})^2} \quad (\text{C.13a})$$

$$A_{xx} = \frac{-\sin^4 \theta_{CM}}{(4 - \sin^2 \theta_{CM})^2} \quad (\text{C.13b})$$

$$A_{yy} = \frac{\sin^4 \theta_{CM}}{(4 - \sin^2 \theta_{CM})^2} \quad (\text{C.13c})$$

$$A_{zx} = A_{xz} = \frac{2 \sin^3 \theta_{CM} \cos \theta_{CM}}{\gamma (4 - \sin^2 \theta_{CM})^2} \quad (\text{C.13d})$$

$$A_{xy} = A_{yx} = A_{yz} = A_{zy} = 0 \quad (\text{C.13e})$$

which are what are commonly seen in the literature [109, 110].

Appendix D

Hydro-Møller: Expected Event Rates

D.1 Expected Event Rates

Finding the rates for Møller scattering is important for the design of the detector system. For a typical Møller polarimeter the acceptance on the detectors is selected to be a small range of θ_{CM} angle around 90° , where A_{zz} is maximum, as shown in Fig. 6.2.

The scattering rate, R , is proportional to the luminosity, \mathcal{L} , and the cross section σ of an interaction,

$$R = \mathcal{L} \sigma, \quad (\text{D.1})$$

or using the differential cross section $\frac{d\sigma}{d\Omega}$ and integrating over the solid angle $d\Omega$,

$$R = \int \mathcal{L} \frac{d\sigma}{d\Omega} d\Omega. \quad (\text{D.2})$$

The luminosity is a product of the flux of the beam, N_b and the areal number of scattering centers in the given target, N_t ,

$$\mathcal{L} = N_b N_t. \quad (\text{D.3})$$

By using the definition of an Ampere, the flux of the beam over the beam current, \widetilde{N}_b can be found

$$\widetilde{N}_b = 6.2415 \times 10^{12} \frac{\text{Hz}}{\mu\text{A}} \quad (\text{D.4})$$

where $\widetilde{N}_b = N_b I_B$ where I_B is the beam current. The number of scattering centers in a target is given by

$$N_t = \frac{\rho_a N_A}{M_a}, \quad (\text{D.5})$$

where N_A is Avogadro's number, M_A is the average mass of the target nuclei in atomic mass units and ρ_A is the areal density of the target taking into account the number of scattering centers per atom. For a cryogenic target like the Hydro-Møller target, the areal density can be broken down into the length of the target, l and the volume density of the target, ρ_V by $\rho_A = l\rho_V$ ¹.

For the Hydro-Møller target with an effective length, l of 20.0 cm and ρ_V of $3 \times 10^{15} \text{ cm}^{-3}$ [1, 2], the luminosity divided by the beam current, $\widetilde{\mathcal{L}}$ where $\mathcal{L} = \widetilde{\mathcal{L}} I_B$, is

$$\widetilde{\mathcal{L}} = 0.374 \frac{\text{Hz}}{\mu\text{A } \mu\text{b}} \quad (\text{D.6})$$

Both the analyzing power and the unpolarized cross section can be considered constant over a suitably small range of θ_{CM} as shown in Fig. 8.4. However, for this a constant analyzing power will be considered, but the unpolarized cross section will be integrated over. For a range in ϕ inclusive from 0 to 2π and a range in θ_{CM} inclusive from 75° to 105° , the solid angle covered is

$$\int d\Omega = 31.140 \text{ sr}. \quad (\text{D.7})$$

Here we consider two different beam energies, 2 GeV to 11 GeV, corresponding to the low and high beam energies of the JLab accelerator, post upgrade. With an Hydro-Møller with target beam polarization, P_t^z of 100% [1, 2], and a beam polarization P_b^z

¹The target consist of H, therefore has one electron, otherwise ρ_V would need to take the number of electrons (Z) into account. Thus in general $\rho_A = Zl\rho_V$.

from experienced during the Q_{weak} experiment of 89% [22], then the polarized cross sections for the low beam energy, $\frac{d\sigma}{d\Omega_L}$ and high beam energy, $\frac{d\sigma}{d\Omega_H}$ become,

$$\sigma_L = 97.253 \mu\text{b} \quad (\text{D.8a})$$

$$\sigma_H = 17.680 \mu\text{b}. \quad (\text{D.8b})$$

For the beam current, I_B from Q_{weak} experiment of $180 \mu\text{A}$, combining the values for luminosity over the current in Eq. D.6, and the differential cross sections for both beam energies Eq. D.8, the rates for the low beam energy R_L and high beam energy, R_H become

$$R_L = 6.556 \text{ kHz} \quad (\text{D.9a})$$

$$R_H = 1.192 \text{ kHz}. \quad (\text{D.9b})$$

For the proposed MOLLER experiment the I_B is lower, $80 \mu\text{A}$.

These are rates that suggest that with high precision polarimetry can be done in a reasonable short time assuming a fairly efficient detector system.

D.2 Experimental Time Required per Measurement

From the rates found in Appendix D.1, how long it would take to reach a relative statistical precision on the beam polarization would be useful to estimate.

For Møller scattering, the relationship of the measured asymmetry (A_{msr}) to the polarization of the target (P_t^z), beam (P_b^z), and A_{zz} is given in Eq. 6.12,

$$A_{msr} = P_b^z P_t^z A_{zz}(\theta_{CM}).$$

Assuming an ideal world, there is no backgrounds, 100% detection the relative statistical

uncertainty on A_{msr} is the same as P_b^z ,

$$\frac{dA_{msr}}{A_{msr}} = \frac{dP_b^z}{P_b^z}. \quad (\text{D.10})$$

Therefore time it takes to make a statistical measurement on A_{msr} will be the same for P_b^z in this ideal case^{2,3}.

Using the integrated output signal from the main detectors, the measured asymmetry, A_{msr} was calculated from the helicity dependent sum of the cross section (σ).

Eq. 2.40, can be written in terms of the number of electrons counted in each helicity state (n_+ and n_-) rather than the cross section,

$$A_{msr} = \frac{n_+ - n_-}{n_+ + n_-}. \quad (\text{D.11})$$

Using this the statistical uncertainty on n_+ and n_- can be propagated through to A_{msr} .

$$(dA_{msr})^2 = dn_+^2 \left(\frac{\partial A_{msr}}{\partial n_+} \right)^2 + dn_-^2 \left(\frac{\partial A_{msr}}{\partial n_-} \right)^2 \quad (\text{D.12})$$

The two partial derivatives from Eq. D.12 are,

$$\frac{\partial A_{msr}}{\partial n_+} = \frac{2n_-}{(n_+ + n_-)^2} \quad (\text{D.13a})$$

$$\frac{\partial A_{msr}}{\partial n_-} = \frac{-2n_+}{(n_+ + n_-)^2}. \quad (\text{D.13b})$$

Then substituting Eq. D.13 into Eq. D.12,

$$(dA_{msr})^2 = dn_+^2 \left(\frac{2n_-}{(n_+ + n_-)^2} \right)^2 + dn_-^2 \left(\frac{-2n_+}{(n_+ + n_-)^2} \right)^2. \quad (\text{D.14})$$

Like in Appendix D.1 where A_{zz}^{max} in calculating σ_0 , here the relationship between

² A_{zz} has no uncertainty as it is the theoretical, and P_t^z has no statistical uncertainty.

³While the relative statistical uncertainty on A_{zz} and P_t^z would be same the absolute statistical uncertainty will different, $dA_{msr} = A_{zz}^{max} dP_t^z$.

n_+ , n_- and n_{tot} can be found

$$n_- = 8n_+ \quad (\text{D.15a})$$

$$n_{\text{tot}} = 9n_+. \quad (\text{D.15b})$$

Likewise,

$$dn_+ = \sqrt{n_+} \quad (\text{D.16a})$$

$$dn_- = \sqrt{8n_+} \quad (\text{D.16b})$$

$$dn_{\text{tot}} = 3\sqrt{n_+}. \quad (\text{D.16c})$$

Substituting Eqs. D.15 and D.16 into Eq. D.12,

$$(\text{d}A_{msr})^2 = \frac{32}{81n_{\text{tot}}}. \quad (\text{D.17})$$

Thus⁴,

$$\text{d}A_{msr} = \frac{4\sqrt{8}}{9\sqrt{n_{\text{tot}}}}. \quad (\text{D.18})$$

In order to get a calculate $\text{d}A_{msr}/A_{msr}$ from Eq. D.18, one must assume that a value of A_{msr} based on the average A_{zz} for the range in θ_{CM} in which the measurement is made, in this case A_{zz}^{max} . Therefore,

$$\frac{\text{d}A_{msr}}{A_{msr}} = \frac{4\sqrt{8}}{7\sqrt{n_{\text{tot}}}}. \quad (\text{D.19})$$

For a 0.5% statistical uncertainty on the A_{msr} , n_{tot} is,

$$n_{\text{tot}} = 26122.4. \quad (\text{D.20})$$

Finally, for the rates in Eq. D.9 the time (t) it would take to make a 0.5% statistical

⁴If one assumes that A_{msr} is small then $n_+ \approx n_-$ thus $n_{\text{tot}} \approx 2n_+$ one will get the usual $\text{d}A_{msr} = 1/\sqrt{n_-}$ as one would expect.

measurement on P_b^z is

$$t_L = 3.98 \text{ sec} \tag{D.21a}$$

$$t_H = 21.91 \text{ sec} . \tag{D.21b}$$

The time it will actually take to make a measurement of this statistical precision will increase due to any change in the angle coverage of the detectors⁵. As stated earlier this calculation also assumes that this is a detector with 100% efficiency, and there are no backgrounds.

⁵The angles range used in Appendix D.1 is $\phi \in [0, 2\pi]$ and $\theta_{CM} \in [75^\circ, 105^\circ]$.

References

- [1] E. Chudakov and V. Luppov, *IEEE Trans. Nucl. Sci.* **51**, 1533 (2004).
- [2] E. A. Chudakov and V. G. Luppov, *Møller Polarimetry with Atomic Hydrogen Target*, Unpublished: Project Description, 2005.
- [3] C. Burgard, *Standard model of physics*, T_EXample.net, (2016) <http://www.texample.net/tikz/examples/model-physics/>.
- [4] D. Galbraith, *Ux: standard model of the standard model*, CERN Webfest 2012, (2017) <http://davidgalbraith.org/portfolio/ux-standard-model-of-the-standard-model/>.
- [5] F. Halzen and A. D. Martin, *Quarks and Leptons: An Introductory Course in Modern Particle Physics* (Wiley, 1984).
- [6] P. Langacker, *The Standard Model and Beyond* (CRC Press, Boca Raton, FL, 2010).
- [7] R. Mann, *An Introduction to Particle Physics and the Standard Model* (CRC Press, Boca Raton, FL, 2010).
- [8] D. Perkins, *Introduction to High Energy Physics*, 4th ed. (Cambridge University Press, Cambridge New York, 2000).
- [9] M. E. Peskin and D. V. Schroeder, *An Introduction to Quantum Field Theory* (Addison-Wesley, Reading, Mass, 1995).
- [10] C. S. Wu *et al.*, *Phys. Rev.* **105**, 1413 (1957).
- [11] S. L. Glashow, *Nuclear Physics* **22**, 579 (1961).
- [12] A. Salam, “Weak and Electromagnetic Interactions”, in *Elementary Particle Theory*, edited by N. Svartholm (Almqvist & Wiksell, Stockholm, 1968), p. 367.
- [13] S. Weinberg, *Phys. Rev. Lett.* **19**, 1264 (1967).
- [14] C. Patrignani *et al.* (Particle Data Group), *Chin. Phys.* **C40**, 100001 (2016).
- [15] A. Kurylov, M. J. Ramsey-Musolf, and S. Su, *Phys. Rev. D* **68**, 035008 (2003).
- [16] J. Erler and M. J. Ramsey-Musolf, *Phys. Rev. D* **72**, 073003 (2005).
- [17] F. Zwicky, *Astrophys. J.* **86**, 217 (1937).
- [18] V. C. Rubin and W. K. Ford Jr., *Astrophys. J.* **159**, 379 (1970).
- [19] P. L. Anthony *et al.* (SLAC E158), *Phys. Rev. Lett.* **95**, 081601 (2005).
- [20] G. Aad *et al.* (ATLAS), *Phys. Lett. B* **716**, 1 (2012).

- [21] S. Chatrchyan *et al.* (CMS), Phys. Lett. B **716**, 30 (2012).
- [22] D. Androic *et al.* (Q_{weak}), Phys. Rev. Lett. **111**, 141803 (2013).
- [23] R. D. Young *et al.*, Phys. Rev. Lett. **99**, 122003 (2007).
- [24] C. Reece, in 9th Workshop on RF Superconductivity, Jefferson Lab (1999).
- [25] C. W. Leemann, D. R. Douglas, and G. A. Krafft, Annu. Rev. of Nucl. Part. Sci. **51**, 413 (2001).
- [26] Jefferson Lab’s Public Affairs Office, *How CEBAF Works*, (Aug. 2016)
- [27] D. S. Armstrong *et al.* (Q_{weak}), arXiv/1202.1255 (2007).
- [28] T. Allison *et al.* (Q_{weak}), Nucl. Instrum. Meth. **A781**, 105 (2015).
- [29] W. Deconinck, private communication, 2015.
- [30] P. Wang, “A Measurement Of The Proton’s Weak Charge Using An Integration Čerenkov Detector System”, PhD thesis (University of Manitoba, 2011).
- [31] J. M. Mammei, “Parity-Violating Elastic Electron Nucleon Scattering: Measurement of the Strange Quark Content of the Nucleon and Towards a Measurement of the Weak Charge of the Proton”, PhD thesis (Virginia Polytechnic Institute and State University, 2010).
- [32] J. P. Leckey IV, “The First Direct Measurement of the Weak Charge of the Proton”, PhD thesis (The College of William and Mary, 2011).
- [33] J. R. Hoskins, “Determination of the Proton’s Weak Charge via Parity Violating Electron Scattering”, PhD thesis (The College of William and Mary, 2015).
- [34] K. E. Myers, “The First Determination of the Proton’s Weak Charge Through Parity-Violating Asymmetry Measurements in Elastic e+p and e+Al Scattering”, PhD thesis (The George Washington University, 2012).
- [35] S. Yang, “A Precision Measurement Of The Weak Charge Of The Proton At Low Q^2 : Kinematics And Tracking”, PhD thesis (The College of William and Mary, 2016).
- [36] A. Lee, private communication, Virginia Tech, 2016.
- [37] S. Agostinelli *et al.* (GEANT4), Nucl. Instrum. Meth. **A506**, 250 (2003).
- [38] G. Smith, *LH2 Target (& Collimators) to QTOR Z Distance*, (Password required for access, please contact author for access.), (June 2015) <https://qweak.jlab.org/eelog/Target/27>.
- [39] J. Pan, *Update on hydrogen target Z-location sensitivity*, (Password required for access, please contact author for access.), (Apr. 2015) <https://qweak.jlab.org/eelog/Tracking/208>.
- [40] G. Smith and S. Covrig, *bulk boiling revisited*, (Password required for access, please contact author for access.), (June 2016) <https://qweak.jlab.org/eelog/Target/29>.
- [41] D. Armstrong, *Target Boiling and Q^2* , (Mar. 2017) <https://dilbert.physics.wm.edu/Physics/201>.

- [42] Jefferson Lab Alignment Group, *Data Transmittal*, #C1300, unpublished, July 8 2010.
- [43] Jefferson Lab Alignment Group, *Data Transmittal*, #C1346, unpublished, Nov. 11 2010.
- [44] Jefferson Lab Alignment Group, *Data Transmittal*, #C1472, unpublished, July 25 2012.
- [45] D. Armstrong, *Q² uncertainty due to QTor absolute calibration*, (Mar. 2015) <https://dilbert.physics.wm.edu/Physics/128>.
- [46] P. Wang, “Magnetic Field Simulation and Mapping for the Q_{Weak}^P Experiment”, Masters Thesis (University of Manitoba, 2007).
- [47] Jefferson Lab Alignment Group, *Data Transmittal*, #C1291, unpublished, June 14 2010.
- [48] Jefferson Lab Alignment Group, *Data Transmittal*, #C1295, unpublished, June 30 2010.
- [49] Jefferson Lab Alignment Group, *Data Transmittal*, #C1517, unpublished, July 29 2013.
- [50] M. Pitt, *Geometrical contribution to Q2 error*, (Password required for access, please contact author for access.), (Feb. 2017) <https://enterprise.phys.vt.edu/eelog/MISCELLANEOUS/513>.
- [51] G. Smith, “Analysis of collimator survey results”, (Password required for access, please contact author for access.), Apr. 2011.
- [52] A. Subedi, “Determination of the weak charge of the proton through parity violating asymmetry measurements in the elastic e+p scattering”, PhD thesis (Mississippi State Universtiy, 2014).
- [53] *Dispersion of main detector from tracking data*, <https://dilbert.physics.wm.edu/Physics/188>.
- [54] D. Armstrong, *R-Det (light-weighting correction) for Hydrogen*, (Password required for access, please contact author for access.), (June 2016) <https://qweak.jlab.org/eelog/Tracking/239>.
- [55] D. Armstrong, *Optical Properties of all MD bars from Tracking data*, (Password required for access, please contact author for access.), (June 2016) <https://qweak.jlab.org/eelog/Detector/110>.
- [56] M. Pitt, *R_acc Update - January 6, 2017*, (Password required for access, please contact author for access.), (Jan. 2017) <https://qweak.jlab.org/eelog/Analysis+%5C%26+Simulation/1656>.
- [57] E. Kargiantoulakis, “A Precision Test of the Standard Model via Parity-Violating Electron Scattering in the Q_{weak} Experiment”, PhD thesis (University of Virginia, 2015).
- [58] D. Jones, “Measuring the Weak Charge of the Proton via Elastic Electron-Proton Scattering”, PhD thesis (University of Virginia, 2015).

- [59] J. Magee, “A Measurement of the Parity-Violating Asymmetry in Aluminum and its Contribution to a Measurement of the Proton’s Weak Charge”, PhD thesis (The College of William and Mary, 2016).
- [60] A. Narayan, “Determination of electron beam polarization using electron detector in Compton polarimeter with less than 1% statistical and systematic uncertainty”, PhD thesis (Mississippi State University, 2015).
- [61] J. C. Cornejo, “Compton Scattering Polarimetry for the Determination of the Proton’s Weak Charge Through Measurements of the Parity-Violating Asymmetry of $^1\text{H}(e, e')p$ ”, PhD thesis (The College of William and Mary, 2016).
- [62] K. A. Aniol *et al.* (HAPPEX), Phys. Rev. Lett. **82**, 1096 (1999).
- [63] K. A. Aniol *et al.* (HAPPEX), Phys. Rev. Lett. **96**, 022003 (2006).
- [64] K. A. Aniol *et al.* (HAPPEX), Phys. Lett. B **635**, 275 (2006).
- [65] A. Acha *et al.* (HAPPEX), Phys. Rev. Lett. **98**, 032301 (2007).
- [66] Z. Ahmed *et al.* (HAPPEX), Phys. Rev. Lett. **108**, 102001 (2012).
- [67] D. T. Spayde *et al.* (SAMPLE), Phys. Lett. B **583**, 79 (2004).
- [68] T. M. Ito *et al.* (SAMPLE), Phys. Rev. Lett. **92**, 102003 (2004).
- [69] F. E. Maas *et al.* (PVA4), Phys. Rev. Lett. **93**, 022002 (2004).
- [70] F. E. Maas *et al.* (PVA4), Phys. Rev. Lett. **94**, 152001 (2005).
- [71] S. Baunack *et al.* (PVA4), Phys. Rev. Lett. **102**, 151803 (2009).
- [72] D. S. Armstrong *et al.* (G0), Phys. Rev. Lett. **95**, 092001 (2005).
- [73] D. Androic *et al.* (G0), Phys. Rev. Lett. **104**, 012001 (2010).
- [74] J. Erler *et al.*, Ann. Rev. Nucl. Part. Sci. **64**, 269 (2014).
- [75] J. Pan, “Towards a Precision Measurement of Parity-Violating e-p Elastic Scattering at Low Momentum Transfer”, PhD thesis (Universtiy of Manitoba, 2012).
- [76] C. Møller, “Zur Theorie des Durchgangs schneller Elektronen durch Materie”, Ann. Phys. (Leipzig) **406**, 531 (1932).
- [77] M. Hauger *et al.*, Nucl. Instrum. Meth. **A462**, 382 (2001).
- [78] C. Y. Prescott, *Spin Dependent Compton Scattering for use in Analyzing Electron Beam Polarizations*, unpublished, SLAC-TN-73-1.
- [79] J. D. Jackson, *Classical Electrodynamics*, 3rd ed. (Wiley, 1998).
- [80] J. Benesch *et al.* (MOLLER), arXiv/1411.4088 (2014).
- [81] L. G. Levchuk, Nucl. Instrum. Meth. **A345**, 496 (1994).
- [82] A. V. Glamazdin *et al.*, Fizika **B8**, 91 (1999).
- [83] A. Narayan *et al.*, Phys. Rev. **X6**, 011013 (2016).
- [84] N. Berger *et al.*, 10th International Workshop on e+e- collisions from Phi to Psi (PHIPSI15) Hefei, Anhui, China, September 23-26, 2015, arXiv:1511.03934 (2015).

- [85] R. W. Cline, T. J. Greytak, and D. Kleppner, *Phys. Rev. Lett.* **47**, 1195 (1981).
- [86] W. N. Hardy *et al.*, *Physica B+ C* **109**, 1964 (1982).
- [87] I. F. Silvera and J. T. M. Walraven, *Phys. Rev. Lett.* **44**, 164 (1980).
- [88] I. F. Silvera and J. Walraven, “Chapter 3: spin-polarized atomic hydrogen”, in *Progress in low temperature physics*, Vol. 10, edited by D. Brewer (Elsevier, 1986), p. 139.
- [89] S. B. Crampton *et al.*, *Phys. Rev. Lett.* **42**, 1039 (1979).
- [90] W. N. Hardy, A. J. Berlinsky, and L. A. Whitehead, *Phys. Rev. Lett.* **42**, 1042 (1979).
- [91] R. A. Guyer and M. D. Miller, *Phys. Rev. Lett.* **42**, 1754 (1979).
- [92] R. Cline *et al.*, *J. Phys. (Paris)* **41**, C7-151 (1980).
- [93] W. N. Hardy *et al.*, *Phys. Rev. Lett.* **45**, 453 (1980).
- [94] B. W. Statt and A. J. Berlinsky, *Phys. Rev. Lett.* **45**, 2105 (1980).
- [95] J. T. M. Walraven and I. F. Silvera, *Phys. Rev. Lett.* **44**, 168 (1980).
- [96] R. W. Cline *et al.*, *Phys. Rev. Lett.* **45**, 2117 (1980).
- [97] J. T. M. Walraven and I. F. Silvera, *Rev. Sci. Instrum.* **53**, 1167 (1982).
- [98] H. F. Hess *et al.*, *Phys. Rev. Lett.* **52**, 1520 (1984).
- [99] J. Walraven, *Physica B+C* **126**, 176 (1984).
- [100] H. F. Hess *et al.*, *Phys. Rev. Lett.* **59**, 672 (1987).
- [101] W. N. Hardy and L. A. Whitehead, *Rev. Sci. Instrum.* **52**, 213 (1981).
- [102] T. Roser *et al.*, *Nucl. Instrum. Meth.* **A301**, 42 (1991).
- [103] W. Kaufman, T. Roser, and B. Vuaridel, *Nucl. Instrum. Meth. A* **335**, 17 (1993).
- [104] R. Chytracek *et al.*, *IEEE Trans. Nucl. Sci.* **53**, 2892 (2006).
- [105] Jefferson Lab Alignment Group, *Data Transmittal, #A1496*, unpublished, Feb 20 2013.
- [106] Jefferson Lab Hall A Moller Group, *General Quadrupole Information*, unpublished, http://hallaweb.jlab.org/equipment/moller/magnets/Moller_quads2.pdf, 2012.
- [107] A. V. Glamazdin and E. Chudakov, *Hall A Møller Upgrade for 11 GeV*, private communication, 2000.
- [108] A. Kresnin and L. Rosentsveig, *J. Exp. Theor. Phys. (USSR)* **5**, 288 (1957).
- [109] J. Arrington *et al.*, *Nucl. Instrum. Meth.* **A311**, 39 (1992).
- [110] M. Swartz *et al.*, *Nucl. Instrum. Meth.* **A363**, 526 (1995).